Design, Fabrication, and Characterization of 3D Nanolattice Photonic Crystals for Bandgap and Refractive Index Engineering

Thesis by

Victoria F. Chernow

In Partial Fulfillment of the Requirements for

the degree of

Doctor of Philosophy

CALIFORNIA INSTITUTE OF TECHNOLOGY

Pasadena, California

2018

(Defended October 30, 2017)

Victoria F. Chernow
ORCID: 0000-0001-5405-1928

Acknowledgments

Caltech is an extraordinary institution, and I am grateful to have spent my graduate career here. It has been a privilege to be a part of such an inspiring community where curiosity and the pursuit of knowledge is foremost and constant. There are few places that can provide the kinds of opportunities and experiences I have been afforded here, and the people I've met throughout my time at Caltech have been truly amazing, indelibly helping to shape the person I've become.

I would like to thank my academic advisor, Professor Julia R. Greer, for her encouragement and constant support through the Ph.D. process. Julia has been singular in her enthusiasm and a primary reason for my choosing to come to Caltech. Upon joining her research group, I was given the structure and intellectual freedom needed to pursue my own research direction, and work in an area that was both unique to my previous experiences and academically stimulating. She has been incredibly supportive in allowing me to tailor my graduate school experience and explore opportunities outside of research. She has been instrumental in my coming to understand my strengths as a researcher, helped me work on my weaknesses, and aided in my discovery of what I love about the scientific process. I am thankful for the resources she has provided to allow me to develop technical and communication skills. Her encouragement to attend conferences has given me the opportunity to present my work, interface and learn from people in a variety of different fields, and create meaningful connections with individuals from all over the world. As I venture into the world outside of academia and graduate school, I know I will continue to use the presentation, communication, and critical thinking skills that Julia has been instrumental in helping me develop.

Thank you to the Dow Resnick grant for financially supporting my research, and the other funding sources which made this work possible.

I would also like to thank Professors Harry A. Atwater, Keith Schwab, William A. Goddard, George R. Rossman, and Oskar J. Painter for taking the time to serve on my candidacy and/or thesis committees and evaluate my work. I am grateful to Keith for his mentorship and advice regarding the scientific process and post-graduate plans, and for participating in my Feynman lectures book club when I was a third year

student. I am incredibly indebted to Professor Rossman for all his help with FTIR and Raman characterization, as well as his scientific expertise and fantastic stories.

The work described this thesis required the use of numerous labs and user facilities throughout Caltech. I am especially grateful for the resources available through the Kavli Nanoscience Institute (KNI). The KNI cleanroom facilities made so much of my work possible, and KNI staff was invaluable in helping me to use and master a number of fabrication and characterization tools. In particular, I would like to thank Matthew Sullivan Hunt and Melissa Melendes. Matt has been an incredible resource for all things SEM and FIB related, and I am grateful for his compassion in listening to the various tribulations and joys of my day. During her time with the KNI, Melissa was the gatekeeper and master user of a plethora of tools, and I am thankful for her excellent training and cheerful disposition in all situations. I am very grateful to the Atwater group for their willingness to share lab resources and to the numerous graduate students who work so hard maintaining equipment and training others. In particular, I would like to thank Dr. Siying Peng for her help and training in using the angle resolved spectroscopy setup she custom built—Siying was an amazing resource for discussing the physics of photonic crystals and methodologies for studying these structures.

Thank you to Professor Jennifer A. Dionne and Dr. Hadiseh Alaeian at Stanford University for being exceptional collaborators on my first graduate research project. Thank you to Dr. Katherine Fountaine, Dr. Philip Hon, and Georgia Papadakis for your insights and all the scientific discussions which made the work in Chapter 4 possible.

I am hugely grateful for all of the amazing people I have gotten to know in the Greer group. You were so much more than labmates and scientific colleagues—I am lucky to have worked with you, and in so doing, formed friendships that extended far beyond the lab. Thank you to Wendy, Rachel, and Lauren for being such incredible female exemplars. Chatting, laughing, and baking with you were highlights of time at Caltech. Thank you to Zach and David for being the greatest of officemates—not only were you saint-like in your patience with me, your advice and humor were invaluable. Thank you to Ryan, Lucas, Ottman, Eric, Carlos, and Arturo for all your help—scientific and otherwise—I have always viewed you as model researchers and am so grateful for the friendships we've forged. Thank you to Alessandro, Stephane, Daryl,

Mike, Dylan, Namita, Jan, Andrey, and all Greer group members past and present – time spent with you inside and outside the lab was central to what made my Caltech experience so memorable.

Thank you to Jane Herriman, Georgia Papadakis, and Heather Duckworth. You inspire me with your intellect, ambition, and ingenuity. In times of triumph, and inevitable graduate school melancholy, I am so grateful to have been able to turn to you for encouragement and counsel.

I'd like thank the whole of Ruddock for being a home away from home for two memorable years. Getting to know you all, and gaining an insight into undergraduate life at Caltech, has been an awesome experience. Thank you to the whole RA team for being so incredible. And thank you to everyone on the Caltech Ballroom Dance Club for being the best group on campus and providing me with a creative outlet, as well as a great group of friends.

Finally, thank you to my amazing, extraordinary, and unconditionally supportive family. My parents, Inna and Jeff, and my brother Lenny – thank you for encouraging me to pursue this Ph.D. and turn my scientific interest into a career, even though it meant moving across the country. Throughout this process you have been my staunchest advocates and I could not be more grateful for every sacrifice you've made to help me (like the number of times you've flown to California to help me move to a new apartment). You have and continue to encourage me to keep learning and always push the boundaries, and everything I've achieved, no matter how large or small, has been in large part because of your support. And to my late grandmother Paula—the strongest, fieriest woman I have ever known—this thesis is dedicated to you.

Abstract

Three-dimensional (3D) photonic crystals (PhCs) have been the focus of ever-increasing interest in the scientific community given their potential to impact areas spanning energy conversion to analyte sensing. These architected materials are defined by a refractive index that is spatially modulated with a period comparable to that of the electromagnetic wavelength. As a result, constructive and destructive interference due to multiple scattering gives rise to a band structure for photons which may contain gaps. Both bands and bandgaps can be engineered to specifically manipulate light propagation by 3D PhCs. In this work we explore the effect of lattice architecture, finite-size effects, and material constraints on stopband position and emergence of band dispersion phenomena like negative refraction. We show that uniaxial mechanical compression can be used to stably and reversibly tune stopband position in 3D polymer nanolattice PhCs with octahedron unit-cell geometry. We then explore how lattice architecture, namely the differences in 3D cubic space group and finite size effects impact experimentally observable stopbands, and assess the degree to which the stopband behavior of real PhCs can be adequately described by the photonic band structure for an infinite, ideal PhC. Finally, we discuss the design, fabrication, and characterization of a core-shell 3D nanolattice PhC which exhibits an effective negative refractive index in the mid-infrared range.

Published Content and Contributions

Chapter 2 is adapted from:

1) **V.F. Chernow**, H. Alaeian, J.A. Dionne, J.R. Greer. "Polymer lattices as mechanically tunable 3-dimensional photonic crystals operating in the infrared." *Appl. Phys. Lett.* **107,** 101905 (2015). DOI: 10.1063/1.4930819

   V.F.C. designed, fabricated, and characterized samples (TPL DLW, SEM, FTIR), performed compression experiments, analyzed data, performed cell pathlength calculations, and wrote the manuscript.

Chapter 4 is adapted from:

2) **V.F. Chernow,** R.C. Ng, J.R. Greer. "Designing core-shell 3D photonic crystal lattices for negative refraction." in *Proc. SPIE* (eds. Adibi, A., Lin, S.-Y. & Scherer, A.) 1, 101120G (2017). DOI: 10.1117/12.2251545

   V.F.C. designed and performed plane wave expansion method simulations, analyzed data, fabricated samples (TPL DLW and O_2 plasma etching), and wrote the manuscript.

3) **V.F. Chernow**, R.C. Ng, S. Peng, H.A. Atwater, J.R. Greer. "Dispersion mapping in 3D core-shell photonic crystal lattices" (in preparation).

   V.F.C. designed, fabricated, and characterized samples (TPL DLW, and O_2 plasma etching, SEM, FIB, FTIR, angle-resolved spectroscopy), plane wave expansion method simulations, analyzed data, and wrote the manuscript.

TABLE OF CONTENTS

Acknowledgments ii
Abstract v
Published Content and Contributions vi
List of Figures x
List of Tables xi
Chapter 1: Introduction to 3D Periodic Architectures as Photonic Crystals 1
1.1. Outline and Objectives 1
1.2. A Brief Introduction to Photonic Crystals 2
1.2.1. A Concise Overview of Photonic Crystal Theory 3
Chapter 2: Exploring the Photonic Band Gap Properties of 3D Periodic Architectures – Tuning Band Gap Position with Mechanical Strain 5
2.1. Introduction and Motivation 5
2.2. Fabrication of 3D lattices 6
2.2.1. Two Photon Lithography Direct Laser Writing (TPL DLW) 6
2.3. Mechanical Characterization of 3D Polymer Octahedron Nanolattices 8
2.3.1. Exploring Polymer Nanolattice Recoverability 8
2.3. Optical Characterization of Angle-Varied Nanolattices 9
2.3.1. Discussion of Stopband Position versus Effective Strain 10
2.4. Optical Characterization of in-situ Strained Nanolattices 12
2.4.1. Compression Cell Fabrication 13
2.5. Results and Discussion of Band Gap Tuning using Mechanical Strain 15
2.5.1. Calculating Compression Cell Pathlength Using the Interference Fringe Method 17
2.6. Comparison of Experimental Bandgap Position and Simulated Bandgap Results 19
2.7. Conclusions and Evolved Critiques 22
Chapter 3: Exploring the Photonic Band Gap Properties of 3D Periodic Architectures – Band Gap Properties as a Function of 3D Periodic Architecture 23
3.1. Outline and Motivation 23
3.2. Introduction to Periodic Lattice Architectures 23
3.2.1. Simple Cubic, Face Centered Cubic, and Base Centered Cubic 3D PhCs 23
3.3. Fabrication of 3D Nanolattices PhCs 27
3.4. Optical characterization of Octahedron, Octet, and Tetrakaidecahedron Nanolattices PhCs 29
3.4.1. Reflectivity Spectra with respect to Geometry and Periodicity 29
3.5. Comparing Experimental Reflectivity to Calculated Photonic Band Structure 31
3.5.1. Photonic Band Structure Calculations 31

3.5.2. Direct Comparison of Peak Reflectivity and Bandgap Position 35
3.5.3. Comparing the FWHM of Reflectivity Peaks to Calculated Bandgap Width 39
3.6. Future Directions for Exploring the Photonic Properties of Polymer 3D Architected PhCs 42
Chapter 4: Exploring the Band Structure and Band Dispersion Phenomena of 3D Periodic Architectures – Demonstrating Negative Refraction in 3D Photonic Crystal Lattices 44
4.1. Introduction and Motivation 44
4.1.1. Photonic Crystal Bands and Equi-frequency contours (EFCs) 44
4.2. Negative Refraction and its Implications 45
4.2.1. Negative Refraction in metamaterials 45
4.2.2. Negative Refraction in Photonic Crystals 46
4.3. Photonic Band Structure and Equi-frequency Contour Calculations 47
4.3.1. Exploring Varied Simulation Parameters: Fill Fraction 49
4.3.2. The Effect of Relative Index of Refraction 51
4.3.2.1. Polymer Core, Ge Shell PhCs 51
4.3.2.2. Carbon Core, Ge Shell PhCs 54
4.3.2.3. Polymer Core, Si Shell PhCs 55
4.3.3. The Effect of Beam Ellipticity 57
4.3.4. The Effect of Shell Offset Relative to Core Position 59
4.3.5. The AANR Region and Experimental Observation of Negative Refraction 61
4.4. Core-Shell Photonic Crystal Fabrication 62
4.4.1. TPL DLW process 62
4.4.2. Discussion of Surface Symmetry Effects and Lattice Orientation 63
4.4.3. O2 plasma Etching 65
4.4.4. Germanium Deposition via Sputtering 66
4.4.5. FIB cross-section characterization of Ge deposition on 3D structures 67
4.5. Optical Characterization of Core-Shell Photonic Crystal Lattices 68
4.5.1. Fourier Transform Infrared Spectroscopy 68
4.5.2. Angle resolved Infrared Spectroscopy for Band Mapping 69
4.5.3. Experimental Observation of a Photonic Band Relevant for Negative Refraction 71
4.5.4. Comparison of Experimental Band Structure and PWE Simulation Results 72
4.6. Conclusions and Outlook on Negative Refraction with 3D PhCs 74
4.6.1. Creation of a 3D Core-Shell PhC Superlens 74
Chapter 5. Perspectives on Future Research Directions for 3D Photonics 77
5.1. Opportunities in PhC Architecture and Topology 77
5.1.1. Topological Photonics 78
5.1.2. Photonic Quasicrystals 79

5.2. Future Directions for Index of Refraction Engineering and 3D Photonic Crystal Fabrication..... 80
Appendicies..... 84
Appendix A..... 84
Appendix B..... 86
Appendix C..... 88
References..... 90

LIST OF FIGURES

Figure 1. Process flow for the fabrication of 3D polymer nano and micro-architected structures 6
Figure 2. Scanning electron microscopy (SEM) images of a representative as-fabricated octahedron nanolattice. 8
Figure 3.Representative stress-strain data for a uniaxial compression of an octahedron nanolattice.. 9
Figure 4. Schematic showing the configuration of the Cassegrain lens used in the Nicolet Continuum Infrared Microscope in reflection mode. 10
Figure 5. The relationship between effective strain and stopband position in as-fabricated angle varied nanolattices 11
Figure 6. Schematic of the nanolattice compression cell setup. 13
Figure 7. Scanning electron microscopy (SEM) images of representative compression cell samples.. 14
Figure 8. Normalized reflectance spectra for an as-fabricated nanolattice outside of the compression cell (red), and under compression (blue) using the custom FTIR compression cell setup. 15
Figure 9. Strain-stopband plots comparing data from the as-fabricated angle-varied lattices under corresponding effective strain, and experimentally strained nanolattices using a compression cell over multiple cycles. 16
Figure 10. FTIR spectra of a background collected against a regular polished silicon surface, and a background collected against the bottom of an empty etched silicon well through a KBr window. .. 18
Figure 11. Results of simulated reflectance for effectively strained nanolattices compared to experimental data.. 20
Figure 12. A color map depicting the variation in reflection as a function of incident angle and wavelength for a simulated 45° nanolattice. 22
Figure 13. Schematic of an octahedron simple cubic PhC lattice. 25
Figure 14. Schematic of an octet face centered cubic PhC lattice 26
Figure 15. Schematic of a tetrakaidecahedron base centered cubic PhC lattice. 26
Figure 16. Representative images of as-fabricated octahedron, octet, and tetrakaidecahedron PhC lattices 28
Figure 17. FTIR reflectance spectra for octahedron, octet, and tetrakaidecahedron nanolattice PhCs..... 30
Figure 18. Brillouin zone and band structure calculated for the octahedron simple cubic lattice 32
Figure 19. Brillouin zone and band structure calculated for the octet face centered cubic lattice. 33
Figure 20. Brillouin zone and band structure calculated for the tetrakaidecahedron base centered cubic lattice. 34
Figure 21. Calculated bands and experimental reflectivity peaks for simple cubic octahedron nanolattice PhCs. 36
Figure 22. Calculated bands and experimental reflectivity peaks for face centered cubic octet nanolattice PhCs. 37
Figure 23. Calculated bands and experimental reflectivity peaks for base centered cubic tetrakaidecahedron nanolattice PhCs.. 38
Figure 24. Outline for comparing the FWHM of experimental reflectivity peaks to the calculated bandgap width $\Delta\omega$ 40
Figure 25. FWHM of experimental reflectivity peaks versus calculated bandgap width $\Delta\omega$ for octahedron, octet, and tetrkaidecahedron PhCs of varying periodicity. 41
Figure 26. CAD schematic of the 3D bcc PhC lattice 48
Figure 27. Representative band structure and equifrequency contours. 49
Figure 28. Average AANR Frequency and AANR Frequency range versus volume fraction.. 50

Figure 29. Average AANR Frequency, AANR Frequency range, and equi-frequency contours for polymer-germanium core-shell PhCs. 53
Figure 30. Average AANR Frequency and AANR Frequency range for amorphous carbon-germanium core-shell PhCs. 55
Figure 31. Average AANR Frequency, AANR Frequency range, and equi-frequency contours for polymer-silicon core-shell PhCs.. 56
Figure 32. Average AANR Frequency, AANR Frequency range, and evolution of band structure for polymer-germanium core-shell PhCs with beams of varying ellipticity. 59
Figure 33. Examples of Ge-shell offset from the polymer-core center position in the X, XZ, and XYZ dimensions, and the effects of shell offset on average AANR Frequency and AANR Frequency range. 61
Figure 34. Surface symmetry and orientation of the bcc PhC lattice. 63
Figure 35. Representative scanning electron microscopy (SEM) image of the (101) lattice face of a bcc PhC lattice after 45 min of oxygen-plasma etching. 66
Figure 36. Scanning electron microscope images of a polymer-germanium core-shell PhC. 67
Figure 37. Normalized FTIR reflectance spectra for the polymer-Ge core-shell bcc PhC lattice compared to reflectance from an IP-Dip polymer thin film. 69
Figure 38. Schematic of the orientation of incident QCL laser light relative to the PhC sample orientation 70
Figure 39. Experimentally measured and calculated band structure for the core-shell PhC lattice. 72
Figure 40. EFC plot and beam propagation construction inside the core-shell bcc PhC and resulting plots of negative refraction and negative effective index. 73
Figure 41. FTIR spectra of an unstrained 45° octahedron nanolattice, and a 1.9μm cured thin film of IP-Dip photoresist 85
Figure 42. FTIR reflectance spectra for a 7.4μm TPL cured IP-Dip thin film, and a fitting curve for the reflectance data extending from 2.5-5.5μm 86
Figure 43. FDTD simulations of octahedron nanolattices.. 88

LIST OF TABLES

Table 1. Figures of merit derived from band structure and EFC calculations on PhC lattices of varied beam diameters with $n_{beam} = 4.0047$ 51
Table 2. Figures of merit derived from band structure and EFC calculations on core-shell PhC lattices of varied polymer core diameter and Ge shell thickness. 53
Table 3. Figures of merit derived from band structure and EFC calculations on core-shell PhC lattices of varied amorphous carbon core diameter and Ge shell thickness. 55
Table 4. Figures of merit derived from band structure and EFC calculations on core-shell PhC lattices of varied polymer core diameter and Si shell thickness. 57
Table 5. Figures of merit derived from band structure and EFC calculations on core-shell PhC lattices with beams of varying ellipticity and constant cross-sectional area. 58
Table 6. Figures of merit derived from band structure and EFC calculations on polymer-Ge core-shell PhC lattices with Ge shell offset from the center core position in the X-direction, XZ-directions, and XYZ-directions. 60

Chapter 1: Introduction to 3D Periodic Architectures as Photonic Crystals

1.1. Outline and Objectives

The scientific community has long been captivated by the search for novel designs to manipulate the propagation of light according to specific demands. To this end, the usage of artificially designed photonic architectures—architectures which are composed of at least two kinds of materials that differ in their respective refractive indices and which are periodically structured on an optical length scale—holds a great deal of promise. The relationship between the specific design of these photonic architectures and their impact on light propagation is a fundamental issue underpinning current research, as this knowledge forms the basis for engineering and tailoring photonic systems for specific optical applications.

Systematic research in the field of three-dimensional (3D) photonic architectures or photonic crystals (PhCs) was initiated in 1987, having been independently introduced in the pioneering work of E. Yablonovitch[1] and S. John[2]. Both proposed that periodically architected dielectric materials will result in the photonic dispersion relation organizing into bands, analogous to the electronic band structure in solid crystalline materials. Photonic stopbands or band gaps can evolve between bands, and are related to Bragg diffraction at the interfaces of the periodically varying dielectric materials. By carefully designing photonic crystals, the band structure can be tailored according to specific requirements and can exhibit unique dispersion phenomena. In particular, 3D PhCs can possess a complete photonic band gap: photons with frequencies within this gap cannot propagate through the structure, but are completely reflected. The existence of photonic bands and band gaps has led to the emergence of the field of photonic band gap engineering, which explores various methods for turning optical materials like photonic crystals into components analogous to those in electronic circuits.

In this thesis, we explore the effect of lattice architecture, finite-size effects, and material constraints on stopband position and emergence of band dispersion phenomena like negative refraction. We design and fabricate 3D PhCs with underlying simple cubic, face centered cubic, and body centered cubic architecture by employing the technique of two photon lithography direct laser writing, which provides the opportunity for arbitrarily structuring photosensitive materials in all three dimensions with sub-diffraction

limited feature sizes. In Chapter 1 we discuss general concepts of photonic crystals with an emphasis on 3D PhCs. In Chapter 2, we explore how uniaxial mechanical compression can be used to stably and reversibly tune stopband position in 3D polymer nanolattice PhCs with octahedron unit-cell geometry. In Chapter 3 we look at how lattice architecture, namely the differences in 3D cubic space group and finite size effects impact experimentally observable stopbands, and assess the degree to which the stopband behavior of real PhCs can be adequately described by the photonic band structure for an infinite, ideal PhC. In Chapter 4 we discuss the design, fabrication, and characterization of a core-shell 3D nanolattice PhC which exhibits an effective negative refractive index in the mid-infrared range. Finally, in Chapter 5 we provide some perspectives on emerging and future directions for 3D PhC research.

1.2. A Brief Introduction to Photonic Crystals

Photonic crystals (PhC) are composites of materials with different refractive indices, where the materials are arranged in a spatially alternating manner such that the resulting modulation period of the refractive index is in the order of the wavelength. Depending on the number of spatial directions a photonic system is structured along, it can be termed a one-dimensional (1D), two-dimensional (2D), or three-dimensional (3D) PhC. With such structure or architecture, the propagation of light in PhCs is strongly modified, which can be qualitatively understood in the context of a 1D PhC, which act as multi-layer mirrors resulting in Bragg-reflection. Propagating light is repeatedly redirected by Fresnel-reflection at the material interfaces in the 1D structure, and depending on the optical path length difference, given by the period a, and the refractive index of the layers, the reflections can interfere constructively and destructively. With such constructive and destructive interference, the propagation of light of certain frequencies is forbidden, as in a highly reflective multi-layer mirror. For 2D and 3D PhCs the situation is considerably more complicated. as the redirection of propagating light occurs via diffraction in two and three dimensions, respectively, and is dependent on such factors as the polarization of incident light, and material boundaries, or PhC architecture. This level of complexity means that, generally, the theoretical modeling of light propagation in PhCs must be done numerically.

1.2.1. A Concise Overview of Photonic Crystal Theory

As mentioned previously, photonic crystals were first discussed by Yablonovitch[1] and John[2] using the analogy of a lattice of electromagnetic (EM) scatterers which manipulate light in a manner similar to how crystalline solids influence electrons. Specifically, when PhC lattice constant is on the order of the wavelength of light, and scattering strength, or dielectric contrast, is substantial, the propagation of light waves inside such a lattice will be modified by the photonic lattice structure.

To determine the new photonic modes inside such a lattice, regularly defined by a position-dependent, periodic dielectric permittivity $\varepsilon(\vec{r})$, Maxwell's equations can be reduced to:

$$\boldsymbol{\nabla} \times \frac{\mathbf{1}}{\boldsymbol{\varepsilon}(\vec{\boldsymbol{r}})} \boldsymbol{\nabla} \times \overrightarrow{\boldsymbol{H}} = \frac{\boldsymbol{\omega}^{\mathbf{2}}}{\boldsymbol{c}^{\mathbf{2}}} \overrightarrow{\boldsymbol{H}} \tag{1}$$

where $\nabla \times \frac{1}{\varepsilon(\vec{r})} \nabla \times$ is a position dependent Hermitian operator, $\overrightarrow{\boldsymbol{H}}$ is the stand-in for the electromagnetic field (in this case it *is* the magnetic field), and ω is the angular frequency of the stationary state. Equation (1) can be seen as an analog to Schrödinger's equation from quantum mechanics, with the Hermitian (self-adjoint) "Hamiltonian" operator on the left corresponding to periodic atomic potentials, and ω^2/c^2 corresponding to the energy eigenvalue. In solving this eigenvalue problem, we note that Eq. (1) is a Hermitian eigenproblem over an infinite domain, and generally produces a continuous spectrum of eigenfrequencies, ω. However, in the case of photonic crystals which possess a periodic dielectric permittivity $\varepsilon(\vec{r})$, we can borrow concepts from electronic band theory and apply Bloch's theorem in deriving solutions to Eq. (1). Here, Bloch's theorem says that the solution for Eq. (1) with a periodic ε can be chosen from:

$$\overrightarrow{\boldsymbol{H}} = \boldsymbol{e}^{\boldsymbol{i}(\vec{\boldsymbol{k}} \cdot \vec{\boldsymbol{x}} - \boldsymbol{\omega t})} \overrightarrow{\boldsymbol{H}}_{\vec{\boldsymbol{k}}} \tag{2}$$

where $\vec{H}_{\vec{k}}$ is a periodic function of position. If we substitute Eq. (2) into Eq. (1), we find that the function $\vec{H}_{\vec{k}}$ satisfies the Hermitian eigenproblem:

$$(\boldsymbol{\nabla} + i\vec{\boldsymbol{k}}) \times \frac{\mathbf{1}}{\boldsymbol{\varepsilon}} (\boldsymbol{\nabla} + i\vec{\boldsymbol{k}}) \times \overrightarrow{\overrightarrow{\boldsymbol{H}}_{\vec{\boldsymbol{k}}}} = \frac{\boldsymbol{\omega}^{\mathbf{2}}}{\boldsymbol{c}^{\mathbf{2}}} \overrightarrow{\boldsymbol{H}}_{\vec{\boldsymbol{k}}} \tag{3}$$

Because $\vec{H}_{\vec{k}}$ is periodic, we need only consider this eigenproblem over a finite domain, the period of the photonic crystal, otherwise known as the unit cell. A general theorem from linear algebra tells us that

eigenvalue problems with a finite domain have a discrete set of eigenvalues. As such, the eigenfrequencies ω emerge as a countable sequence of continuous functions of the wavevector $\vec{\boldsymbol{k}}$ and band index n: $\omega = \omega_n(\vec{\boldsymbol{k}})$. When ω is plotted as a function of $\vec{\boldsymbol{k}}$, these frequency "bands," or modes, form the band structure of the photonic crystal. In frequency regions where no propagating states $\omega_n(\vec{\boldsymbol{k}})$ are allowed, we see the emergence of photonic band gaps. In practice, the complexity of most photonic crystal structures necessitates that photonic band structures are determined numerically rather than analytically, employing computational methods like plane-wave expansion (PWE) and finite difference time domain (FDTD). It is worth stating however, that the numerical results of photonic band structure calculations are essentially exact within the linear response approximation. This is in contrast to the numerical results of electronic band structures which are almost always complicated by the effects of electron-electron interaction and Fermi statistics.

In discussing the nature of photonic modes in a photonic crystal lattice, one should note that an important property of Maxwell's equations in general, and of Eq. (1) in particular, is that they are scale independent. If the unit cell size of your PhC was somehow scaled up by a factor of 2, the solutions would be exactly the same except that the frequencies would be divided by the same factor, 2. An implication is that we can solve for a band structure once, and then apply the same results to problems at all length scales and frequencies. For example, one can design a system in the infrared or microwave regime, and scale the design to other wavelengths, like the optical regime, merely using parameters that are fractions of the original wavelength. Given this scale invariance, it is also convenient to use dimensionless units to designate length or periodicity, a, and time or frequency, ω. As such, all distances will be expressed as a multiple of a and all angular frequencies ω as a multiple of $2\pi c/a$, which is equivalent to writing frequency as a/λ, where λ is the vacuum wavelength.

For a more thorough and rigorous examination of photonic crystal theory, we recommend perusing reference 3.

Chapter 2: Exploring the Photonic Band Gap Properties of 3D Periodic Architectures – Tuning Band Gap Position with Mechanical Strain

2.1. Introduction and Motivation

Three-dimensional (3D) photonic crystals (PhCs) have been the focus of ever-increasing interest in the scientific community given their potential to impact areas spanning energy conversion to analyte sensing. These architected materials have a periodic variation in their refractive index and selectively reflect light of wavelengths on the order of their periodicity[4]. Though only a few 3D PhCs possess a complete photonic bandgap[5,6], defined as a range of frequencies for which incident light cannot propagate in any direction, all 3D PhCs have stopbands that forbid light propagation in some crystallographic directions[7]. Within the spectral range of a photonic bandgap or stopband, light is selectively reflected, rendering 3D PhCs applicable in numerous optical devices such as low-loss mirrors[8,9], lasers[10], chemical[11] and mechanical[12,13] sensors, and displays[14–16]. Several of these applications, including variable filters, laser sources, and strain sensors[7], require that the PhC be reconfigurable or reversibly tunable while maintaining structural integrity, which would enable them to be optically active over a wide range of frequencies. Most existing fabrication methodologies produce PhCs that operate over a fixed and limited bandwidth[17]. The response of these otherwise passive PhCs can be rendered active by fabricating structures using dynamic materials which can respond to external stimuli including, for example, electric fields, solvent swelling, and mechanical deformation.

Stopband position can be tuned by changing either the refractive index and/or the periodicity of the PhC structure, with the latter being generally more straightforward[18]. The number of experimentally available methods for modulating the lattice periodicity exceeds the number of index-tunable materials, and, more importantly, altering the lattice constant often leads to a more substantial stopband shift[19,20]. Several approaches that can reversibly tune the stopband position of PhCs post-fabrication—for example methods based on temperature gradients[21,22], electric fields[23,24], and solvent swelling[25]—often suffer from limited tuning ranges, typically restricted to between 100-200nm shifts. Compositional or structural changes that arise within 3D PhCs in response to mechanical deformation allow for wider tuning ranges,

but are sometimes irreversible[26,27]. In addition, most of the existing mechanically tunable 3D PhCs have been limited to opal and inverse opal type structures[7,19,26,27].

Herein we discuss the fabrication of 3-dimensional polymer nanolattices with ~4μm wide octahedron unit cells that act as PhCs and can be stably and reversibly tuned by mechanical compression over multiple cycles. The mechanical properties of similarly-architected hollow metallic and ceramic octahedron nanolattices have been reported[28–30]. In this work, the polymeric composition facilitates maximum optical tunability and reversibility. We find that a reversible ~2.2μm stopband blueshift can be achieved with a uniaxial compression of ~40%, and that the blueshift is linear for applied strains from 0-40%.

2.2. Fabrication of 3D lattices

2.2.1. Two Photon Lithography Direct Laser Writing (TPL DLW)

Nanolattices are fabricated using a technique called two photon lithography (TPL) direct laser writing (DLW), a process that can be seen as the high-resolution analogue to conventional macroscale 3D printing. TPL DLW allows for the fabrication of almost arbitrary 3D structures with sub-micron feature sizes. Very generally, the high resolution is achieved by tightly focusing a near-IR laser into liquid, negative photoresist, resulting in a change in photoresist solubility. This change in solubility is achieved by local polymerization of the monomer contained in the photoresist. By then moving the relative position of the focused laser volume, called a voxel, with regard to the substrate, 3D structures can be created. In a final step, remaining, unexposed photoresist is washed away with a solvent, leaving only the insoluble 3D polymer structure.

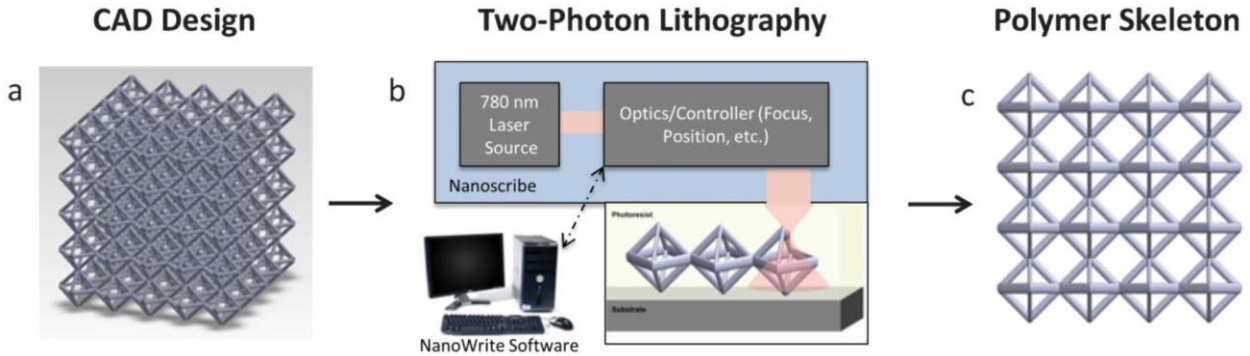

Figure 1. Process flow for the fabrication of 3D polymer nano and micro-architected structures. (a) 3D structures are first designed using CAD software, (b) then written into photosensitive polymer via two-photon lithography direct

laser writing. (c) After washing away undeveloped photoresist, a 3D polymer structure remains. Reproduced with permission from Reference 28 © 2014 Wiley-Blackwell.

We utilize the commercially available TPL DLW system produced by Nanoscribe GmbH in our fabrication process. The TPL DLW workflow first involves designing the desired 3D architecture using a computer aided design (CAD) program like SolidWorks (Figure 1(a)), after which the design is imported to NanoWrite, a proprietary software program that interfaces with the Nanoscribe TPL instrument (Figure 1(b)). Once the structure is defined, a 780nm femtosecond pulsed laser is focused down to a voxel within a droplet of liquid photo-sensitive monomer. Throughout this thesis, the photoresist used is commercially known as IP-Dip (Nanocribe GmbH), and is composed of the monomer pentaerythritol triacrylate (PETA) and the photoinitiator 7-diethylamino-3-thenoylcoumarin (DETC). Within the voxel volume, simultaneous two-photon absorption is possible, leading to the excitation of DETC radicals which initialize polymerization of the PETA monomer. As PETA is a multi-functional monomer, i.e., a monomer with more than one acrylate groups, a cross-linked polymer network is created that is insoluble. The voxel is elliptically shaped and is traced in 3-dimensions within the photoresist droplet, creating a polymer structure of any arbitrary geometry (Figure 1(c)). Laser power and speed can also be modulated, which will impact voxel size, resulting in the creation of features with transverse dimensions as small as 150 nm.[31]

2.2.2. TPL DLW fabricated Octahedron Nanolattices

As described, nanolattices were fabricated using the direct laser writing (DLW) two-photon lithography (TPL) system, Photonic Professional (Nanoscribe GmbH, Germany). Specifically, samples were prepared by drop-casting the negative-tone photoresist "IP-Dip" (Nanoscribe GmbH) on a 500μm thick polished silicon substrate. An infrared laser was then used to crosslink and write a preprogrammed pattern into the acrylic-based photopolymer via two-photon absorption. The exposed sample was then developed for 30 minutes in propylene glycol monomethyl ether acetate and isopropanol. This process allows for maximum control over the final architecture and enables the fabrication of arbitrarily complex nano- and micro-structures. Figure 2 shows that the nanolattices have individual octahedron unit cells on the order of ~4μm, and are 6.5 unit cells tall. Individual beams have elliptical cross-sections, with short axes of ~500nm and long axes of ~1.75μm.

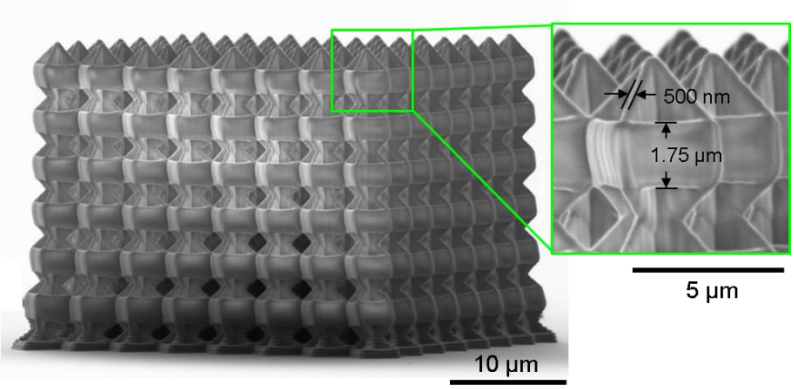

Figure 2. Scanning electron microscopy (SEM) images of a representative as-fabricated octahedron nanolattice. Inset shows relevant dimensions of the unit cell.

2.3.Mechanical Characterization of 3D Polymer Octahedron Nanolattices

Mechanical characterization of the nanolattices was performed using an *in-situ* nanoindenation system, InSEM (Nanomechanics Inc.), inside an SEM chamber (see ref. 32 for specifications). This instrument enables precise measurement of applied load vs. displacement data with simultaneous real-time visualization of nanolattice deformation[32]. *In-situ* uniaxial compression experiments were conducted at a constant prescribed displacement rate of 50nm/sec. Nanolattices were aligned orthogonal to the electron-beam, and in line with the nanoindenter arm, such that the periodicity of the lattice was gradually reduced along this compression axis.

2.3.1. Exploring Polymer Nanolattice Recoverability

Samples were strained by >60% before reaching the instrument load limit of 35mN. Figure 3 shows representative stress-strain data and SEM micrographs captured at various points during a typical experiment. It appears that the polymer nanolattices underwent a global compression, where each layer of unit cells was compressed in a homogenous fashion, gradually decreasing the pitch of the structure. This is in contrast to a layer-by-layer collapse mechanism typical of hollow ceramic and metallic octahedron nanolattices[28–30]. It also appears that the Poisson's ratio of the nanolattices is close to zero because no transverse deformation was observed—the structure neither expanded nor contracted laterally—in response to axial strain. This behavior is likely due to the fact that compressive straining will cause beams to buckle into the pores of the lattice structure, instead of contributing to lateral expansion or contraction. Analysis of SEM images and a hysteresis in the stress-strain data revealed that the structure recovered by ~82%

nearly immediately following load removal after compression in excess of 60%. The acrylic-based polymer that comprises the nanolattice is viscoelastic and continues to recover with time through a time-dependent strain response. We observed a recovery to ~90% of the original height within hours of the primary compression. Subsequent to the initial cycle of compression and recovery, samples were compressed again to ε~60% and appeared to recover to ~100% of their initially-recovered height after this second cycle. Lattices were compressed to ε~60% a 3rd and 4th time and showed similar recovery. This result suggests that a few permanent structural defects were formed during the initial compression, and for all subsequent deformations the structure acts elastically and recovers completely and instantaneously.

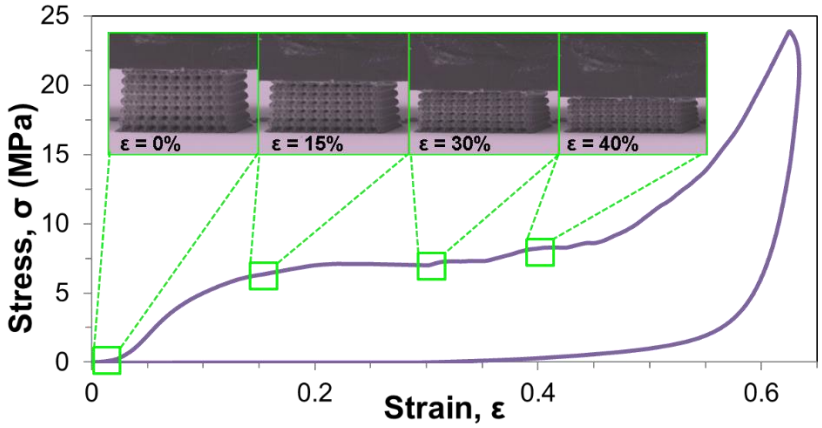

Figure 3.Representative stress-strain data for a uniaxial compression of an octahedron nanolattice. Inset images are scanning electron micrographs of the nanolattice, captured simultaneously at various points during the compression experiment.

2.3. Optical Characterization of Angle-Varied Nanolattices

The micron-scale unit cell size of the nanolattices suggests that the PhC will exhibit a bandgap in the infrared range. We used Fourier Transform Infrared (FTIR) microspectroscopy to evaluate the optical properties of the nanolattices, including their reflectance and stopband position. Spectra were acquired using a Nicolet iS50 FT-IR spectrometer equipped with a Nicolet Continuum Infrared Microscope. This instrument uses a 15x objective with a numerical aperture (N.A.) of 0.58, and has a working distance of 11mm. Because the Nicolet Continuum Infrared Microscope FTIR spectrometer employs Cassegrain type lenses for light focusing, sample illumination at normal incidence was restricted. Instead, light is incident

on the sample as an annulus with an angular range, the upper limit of this range determined by the numerical aperture of the condenser, and the lower limit due to blockage by a secondary mirror residing inside the Cassegrain lens. As shown schematically in Figure 4, light incident on the sample has an angular range between 16°-35.5° relative to the normal.

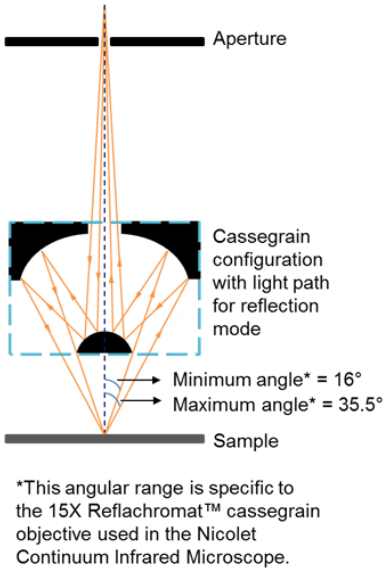

Figure 4. Schematic showing the configuration of the Cassegrain lens used in the Nicolet Continuum Infrared Microscope in reflection mode. Note how the upper limit of the objective's range is determined by the primary mirrors of the Cassegrain, which affect the numerical aperture of the lens, and how the lower limit is due to blockage by a secondary mirror, which also prevents light from hitting the sample at normal incidence.

2.3.1. Discussion of Stopband Position versus Effective Strain

To establish a baseline understanding of the relationship between strain and the position of the stop band, we fabricated several nanolattices which mimicked compressed morphologies for 4 strains—0%, 14.8%, 27.1%, and 38.6%—corresponding to unit cell angles of approximately 45°, 40°, 35°, and 30°, as shown in Figure 5(a-b). These 'effectively strained' angle-varied nanolattices were fabricated with slightly altered geometries such that the unit cells evolved from fully isotropic in the unstrained state, to progressively more anisotropic at higher effective strains (Figure 5(b)). Increasing the degree of anisotropy in the unit cells also serves to uniformly decrease the height and periodicity of the overall lattice, with the effective strains calculated based on the relative change in the unit cell angle experienced by octahedron nanolattices during *in-situ* compression experiments. Compacting lattice periodicity along the z-direction

by altering the unit cell angle allowed us to create a set of effectively strained lattices which represent idealized versions of the compressed octahedron PhC at 0%, 14.8%, 27.1%, and 38.6% strain.

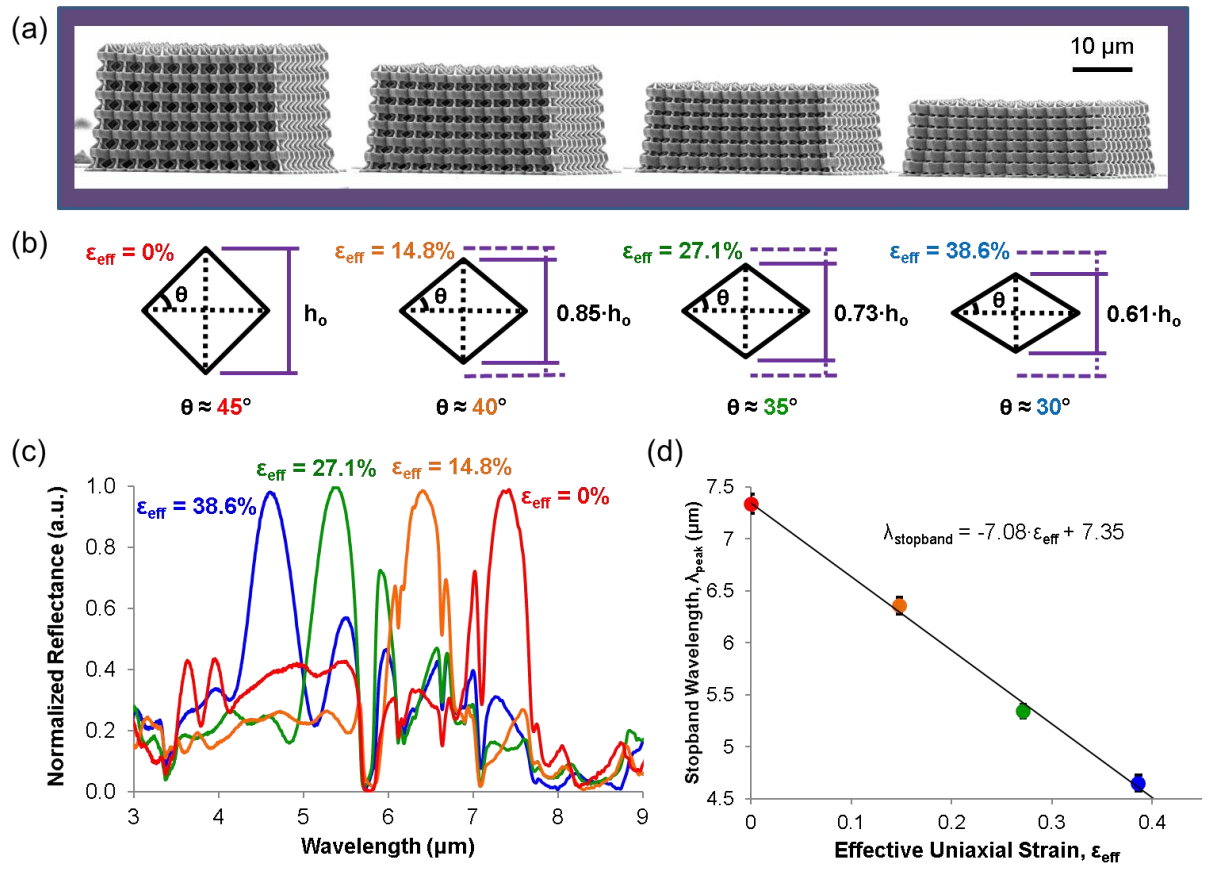

Figure 5. The relationship between effective strain and stopband position in as-fabricated angle varied nanolattices. (a) SEM images of octahedron nanolattices fabricated with varying angles, corresponding to different degrees of effective strain. (b) Schematic of the relationship between unit cell angle and effective strain in the fabricated nanolattice. (c) Normalized reflection spectra of a 45° unstrained octahedron nanolattice, and three angle-varied nanolattices, corresponding to increasing degrees of effective strain, ε_{eff}. (d) Effective strain-stopband plot for the angle-varied lattices. Note that ε_{eff} and λ_{peak} are directly proportional.

Figure 5(c) shows the FTIR reflectance spectra for the four nanolattices. For the as-fabricated nanolattices, a significant peak in normalized reflectance emerges, and is centered at 7.42μm, which corresponds to the first order stop band. The center of this peak shifts to progressively shorter wavelengths for nanolattices with decreasing pitch: from 7.42μm for the unstrained nanolattice to 6.40μm for the 14.8% effectively strained nanolattice, to 5.38μm for 27.1% effective strain, and to 4.61μm for the 38.6% effectively strained sample. The plot in Figure 3(d) reveals the relationship between the central position of each stop band peak, denoted λ_{peak}, and effective strain, ε_{eff}, based on the normalized reflectance

measurements of 24 separate unstrained and effectively strained samples (6 samples for each strain). In addition to the blueshifting of the photonic bandgap with increasing effective strain, the stopband data appears to vary linearly with strain. This is not unexpected because the opto-mechanical response of these 3D PhCs under uniaxial compression is associated with a change in spacing of closest-packed planes, and a consequent change in the Bragg resonance condition and peak wavelength. This trend is similar to the stopband-strain relationships reported for 1D and 2D mechanically tunable photonic crystals[4,33]. The largest stopband shift of 2.8μm was exhibited by samples that were effectively strained by ~40%. This stopband shift is more substantial than the 1.25μm shift achieved by solvent swelling of lamellar photonic crystal gels outlined in Kang et al.[18], and outperforms other elastomeric 3D photonic crystals like the one reported in Fudouzi et al. where a 20% strain leads to a 30nm stopband shift[34].

2.4. Optical Characterization of *in-situ* Strained Nanolattices

The nearly-full recoverability of the compressed polymeric nanolattices studied in this work required the design of a special experimental setup which could measure the optical response of compressed nanolattices in their strained state. Figure 6 provides a schematic of the custom compression cell setup, which was constructed by first etching wells of varying depths into a silicon substrate using deep-reactive ion etching (DRIE), followed by the fabrication of pristine unstrained nanolattices into individual wells. An IR-transparent KBr slide was then placed on top of the nanolattices and wells, and then, to ensure uniaxial straining of the lattices, a washer-shaped lead weight was placed on to the slide.

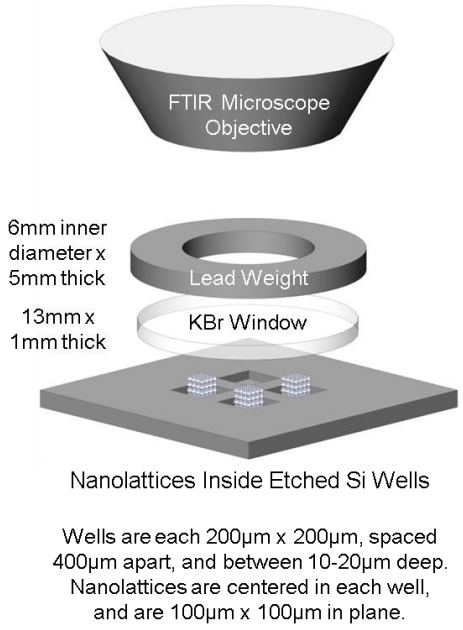

Figure 6. Schematic of the nanolattice compression cell setup.

2.4.1. Compression Cell Fabrication

Polished silicon substrates were initially washed with acetone and isopropanol before additional oxygen plasma cleaning. The 1cm x 1cm silicon chips were then spin coated using Shipley 1813 positive photoresist at 3000 rpm for 30 seconds. Samples were soft baked at 115°C for 1 minute. Samples were then exposed to UV light for 15 seconds through a transparency mask containing a 2 x 4 grid of square boxes, each 200µm x 200µm, and spaced 400µm apart. Following UV exposure, samples were developed for 1 min, rinsed with water, and dried under nitrogen. An Oxford Plasmalab System 100 ICP-RIE was used to dry etch wells into the silicon substrate. The dry reactive ion etch (DRIE) process used was a standard Bosch procedure, where the number of cycles was varied between silicon chips to achieve wells with depths ranging from 10-20µm.

Silicon chips with etched wells were then used as substrates for subsequent nanolattice fabrication. As described in the manuscript, the direct laser writing (DLW) two-photon lithography (TPL) system, Photonic Professional (Nanoscribe GmbH, Germany) was used to do an alignment, and then to write a 100µm x 100µm octahedron nanolattice into the center of the well (nanolattices were to be taller than the edge of the well). Nanolattices were first designed using CAD software, after which structural data was converted to a

file format specific to the Photonic Professional system. On each silicon chip, at least two wells were always left empty so they could be used for taking FTIR background spectra. Following the fabrication and development of the nanolattices, samples were SEM imaged to ascertain the starting height of unstrained structures, and several representative micrographs of the lattices and wells are shown in Figure 7(a-c).

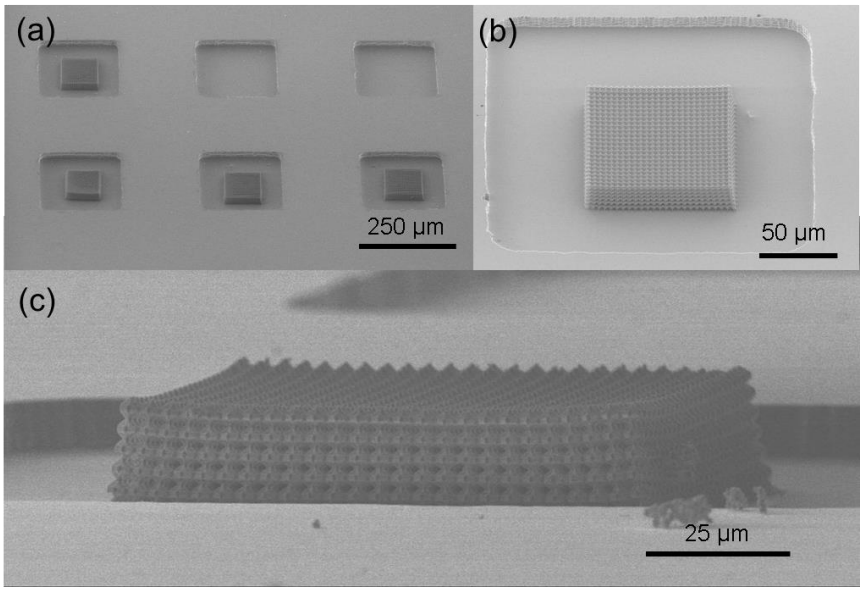

Figure 7. Scanning electron microscopy (SEM) images of representative compression cell samples. (a) A grid of etched wells with nanolattices fabricated into select wells. Two wells are left empty so they can be used for collecting background FTIR spectra. Image was taken at a 45° tilt. (b) A close-up of a single lattice fabricated within an etched silicon well. Image was taken at a 45° tilt. (c) A close-up of a nanolattice inside a well. Image was taken at a 92° tilt, so that it is possible to see that the nanolattice extends beyond the edge of the well (which is important for subsequent compression).

Polished potassium bromide (KBr) slides were then carefully placed on top of the grid of etched silicon wells and nanolattices, in the next step of creating the compression cell. These circular slides were purchased from International Crystal Labs, and had the following dimensions: 13mm diameter, and 1mm thickness.

To complete the compression cell, a lead washer was used as a weight to aid in the compression of the nanolattices built into the etched silicon wells. The weight was placed centrally on top of the KBr slide. These washers were machined to have the following dimensions: 40mm outer diameter, 6mm inner diameter, and 5mm thickness.

2.5. Results and Discussion of Band Gap Tuning using Mechanical Strain

Using the compression cell described above, it was possible to strain an as-fabricated sample to a preordained position, and fix it in the strained state by bounding from above by the IR-transparent KBr slide, while it sits affixed to the polished Si substrate. We then collected reflectance with the same FT-IR spectrometer as used on the effectively strained samples. Four experiments on cyclically strained nanolattices were carried out, with each one corroborating the finding that compressing an octahedron nanolattice leads to a blueshifting in the PhC stopband, and releasing the load shifts the stopband back to within 89.8 ± 2.8% of the original stopband position of the pristine nanolattice—a value commensurate with the ~90% recovery observed in nanolattice height following primary compression. Figure 8 shows the reflection spectrum of a representative sample. For this particular sample, the stopband of the initial nanolattice was centered at 7.32μm and that of the 15.2% strained nanolattice blueshifted to 6.34μm.

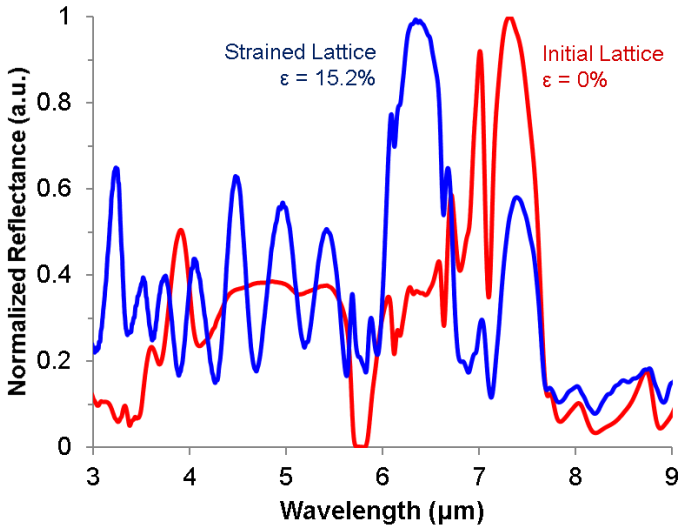

Figure 8. Normalized reflectance spectra for an as-fabricated nanolattice outside of the compression cell (red), and under compression (blue) using the custom FTIR compression cell setup.

For this series of strained nanolattice experiments, the applied strain was monitored by calculating the pathlength of the FTIR compression cell using interference fringes which appear in the background reflection spectra[35]. The KBr surface of the cell is positioned nearly parallel to the Si substrate—between which the nanolattices are sandwiched—which results in the appearance of sinusoidal fringes in the spectra. These fringes are created by interference between light that has been transmitted through the sample, and

light that has been reflected internally between the parallel surfaces[35]. The number and the position of interference fringes allow us to estimate the pathlength through the compression cell[35], which is equivalent to the thickness of the sample and the height of the compressed nanolattices:

$$\boldsymbol{d = \frac{N\lambda_1\lambda_2}{2n_{eff}\cos\theta(\lambda_2-\lambda_1)}} \quad (4)$$

Here, d is the sample thickness or compression cell pathlength, N is the number of interference fringes between the wavelength range λ_1 and λ_2, n_{eff} is the effective refractive index of the material within a well of the compression cell, and θ is the average angle of incident light on the sample. Having measured the height of pristine, unstrained nanolattices using SEM imaging, and calculated the cell pathlength for a compressed sample, we obtained a value for applied compressive strain. Full details on this analysis are provided in the subsequent section.

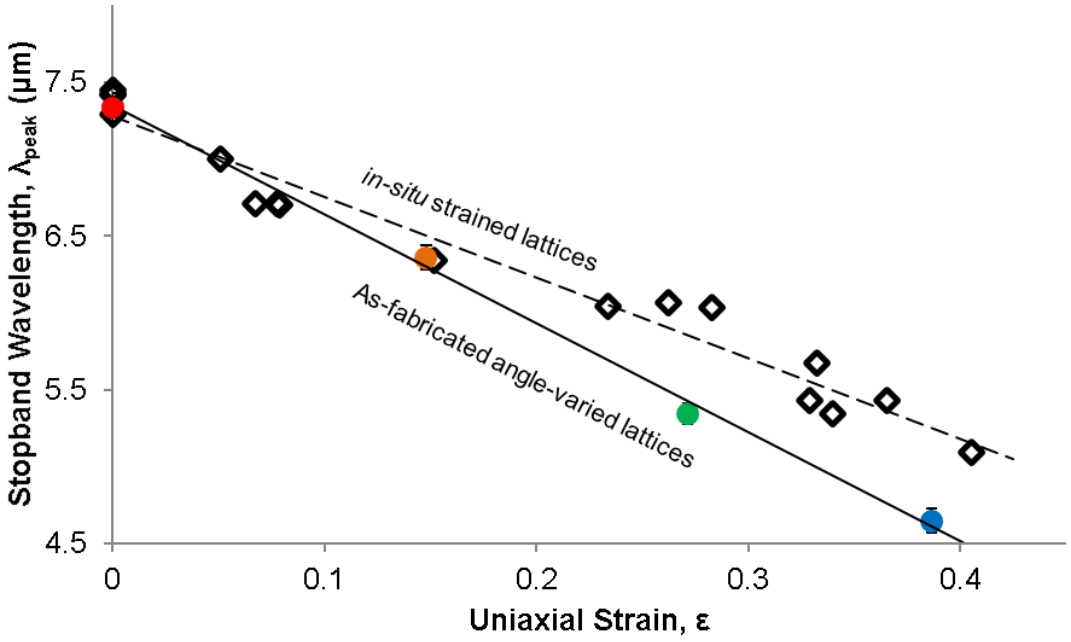

Figure 9. Strain-stopband plots comparing data from the as-fabricated angle-varied lattices under corresponding effective strain, and experimentally strained nanolattices using a compression cell over multiple cycles.

Figure 9 shows that *in-situ* straining of the nanolattices results in a blueshifting of the stopband, and that a linear relationship holds between applied strain and stopband position. The slope of this linear dependency is a factor of 1.42 lower than the slope predicted by the idealized, effectively strained

nanolattices, also plotted in Figure 8 for comparison. This plot reveals that nanolattices strained by 40.5% exhibited a stopband shift of 2.19μm, compared to a 2.87μm shift for the effectively strained angle-varied nanolattices compressed by the same amount. This plot also shows that at high strains of ε ~ 40%, the percent error between the measured λ_{peak} for *in-situ* strained and angle-varied lattices is 14.1%, while at low strains, on the order of ε ~ 10%, the percent error is significantly smaller, at 1.7%. These deviations likely arise from minor shearing in the *in-situ* setup that accompanies the nominal uniaxial compressive straining of the lattice. Shear strain in this system may take the form of a torqueing at the nodes of the unit cells comprising the lattice, which leads to a shape change rather than a volume change, and does not affect the periodicity of the lattice in the vertical direction to the same degree predicted by the angle-varied lattices modelling effective strain. It has been previously shown that the stopband position increases nonlinearly with shear strain[4], which may also contribute to our observation of larger deviations from the λ_{peak} position of the angle-varied lattices modelling effective strain, where only uniaxial strain was taken into account.

2.5.1. Calculating Compression Cell Pathlength Using the Interference Fringe Method

Interference fringes in an FTIR spectrum can be a convenient method for determining the lattice thickness or cell pathlength. Per reference 35, pathlength of the cell may be calculated as

$$\boldsymbol{d} = \frac{\boldsymbol{N}}{\boldsymbol{2n_{eff}(\overline{\nu_1}-\overline{\nu_2})}} \tag{5}$$

where d is pathlength, N is the number of interference fringes between wavenumbers $\overline{\nu_1}$ and $\overline{\nu_2}$, and n_{eff} is the effective refractive index of the material between the two surfaces generating the interference fringes.

As described previously, the Nicolet Continuum Infrared Microscope FTIR spectrometer used in our experiments illuminates the sample in an annulus with an angular range between 16°-35.5° relative to the normal. This non-normal incidence necessitates the addition of a cosine term to equation (5) for more accurate calculations of cell pathlength:

$$\boldsymbol{d} = \frac{\boldsymbol{N}}{\boldsymbol{2n_{eff}\cos\theta(\overline{\nu_1}-\overline{\nu_2})}} \tag{6}$$

where θ is the average angle of incident light on the sample. For all our calculations of the cell pathlength d, we used an average angle of 25.75° to the normal.

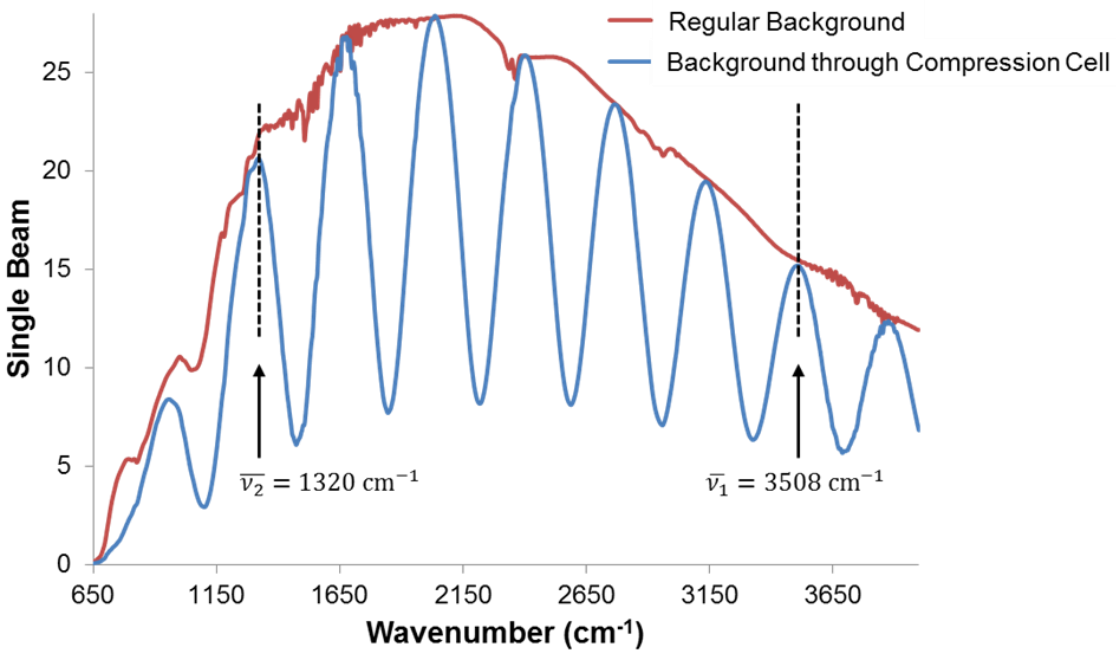

Figure 10. FTIR spectra of a background collected against a regular polished silicon surface, and a background collected against the bottom of an empty etched silicon well through a KBr window, as part of the compression cell. Interference fringes appear in the compression cell spectrum due to reflection between the internal faces of the polished KBr window and Si surface at the bottom of the well.

Before every sample measurement, a background spectrum was collected against a polished silicon surface. In the case of compression cell measurements, background spectra were collected through the KBr window, against the bottom surface of an empty well etched into each silicon chip compression cell. Figure 10 shows an example of a 'regular' background spectrum taken against the reflective surface of a piece of polished silicon, and an example of a background spectrum collected against the reflective surface at the bottom of an empty etched silicon well through the KBr window, as part of the compression cell. While the 'envelope' shape of the background spectrum collected through the KBr window remains consistent with the shape of the 'regular' background spectrum, prominent and relatively regular interference fringes appear in this spectrum due to reflection between the two internal faces of the compression cell (the bottom of the polished KBr slide on one side, and the polished Si surface of the well on the other). We can now utilize equation (6) to determine the cell pathlength in this particular compression cell by counting the number of

fringes between wavenumbers $\overline{\boldsymbol{\nu_1}}$ and $\overline{\boldsymbol{\nu_2}}$. Per Figure 10, $\overline{\boldsymbol{\nu_1}}$= 3508 cm^{-1}, $\overline{\boldsymbol{\nu_2}}$= 1320 cm^{-1}, $N = 6$, $\theta = 25.75°$, and $n_{eff} = 1$ (we take this measurement against the silicon surface of an empty well, so the effective medium is just air). For the specific compression cell background spectrum in Figure 10, cell pathlength/sample thickness (a measure of the distance between the bottom of the polished KBr slide and the silicon surface of the etched well) is $d = 15.2\mu m$. It is by this process that we calculated heights for compressed nanolattices residing in neighboring wells on the same silicon chip. The fringes found in background spectra were often clearer than the fringes which manifested in the reflection spectra of actual compressed nanolattices (see Figure 8)—fringes in compressed nanolattice spectra may become convolved with other features of the reflection spectra—and as such background spectra were used preferentially for cell pathlength calculations.

2.6. Comparison of Experimental Bandgap Position and Simulated Bandgap Results

To numerically investigate the electromagnetic properties of the octahedron nanolattices and see how they compare to experimental results, we employed the Finite Difference Time Domain (FDTD) solver Lumerical. The simulated geometries were determined by using SEM images of the fabricated experimental samples; the polymer refractive index of n~1.49 was determined by fitting FTIR reflectance data for TPL polymerized IP-Dip thin films using a scattering matrix approach combined with a minimization technique (described in Appendix C). We accounted for the almost infinite transverse extent of the lattices by designating Bloch boundary conditions in the x-y plane. In the z-direction normal to the plane, 6.5 unit cells were stacked on top of one another to complete the 3D model of the lattice—similar to our fabricated samples—and the whole stack was assumed to reside on an infinite slab of Si with a fixed refractive index of 3.4 over all frequencies. The entire model was then surrounded by perfect matched layers (PML) along the z-direction.

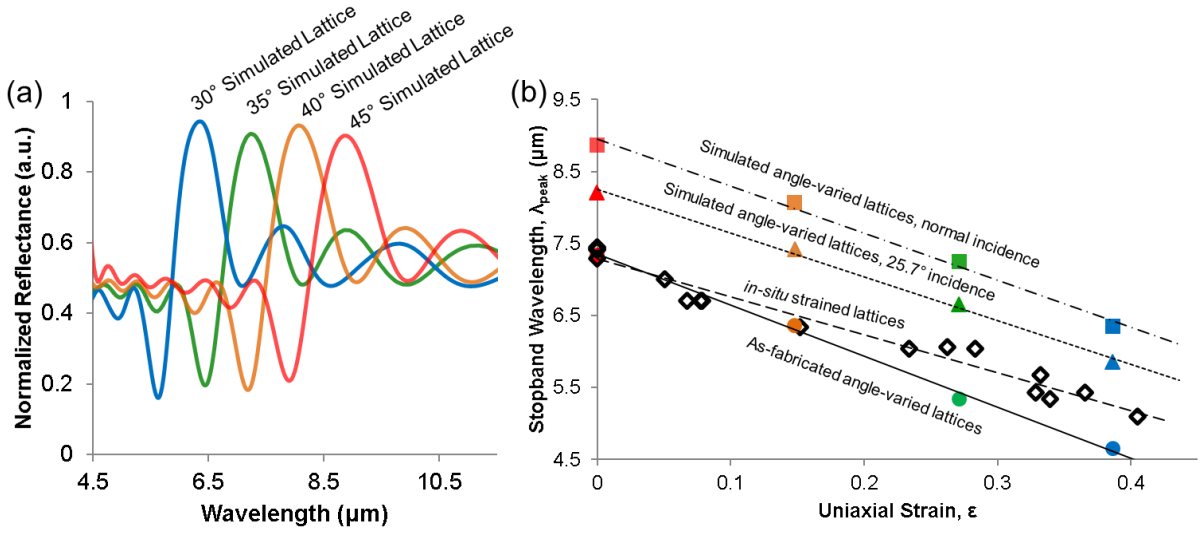

Figure 11. Results of simulated reflectance for effectively strained nanolattices compared to experimental data. (a) Normalized reflection spectra under normal illumination for a simulated 45° unstrained octahedron nanolattice, and three simulated angle-varied nanolattices, each with corresponding degrees of increasing effective strain. The main peak for each simulated nanolattice corresponds to a 1st order Bragg reflection; secondary peaks that appear at longer wavelengths are caused by the higher order Bragg reflections. (b) Strain-stopband plots comparing data from the as-fabricated angle-varied lattices under corresponding effective strain, experimentally strained nanolattices using a compression cell over multiple cycles, and the simulated angle-varied lattices at normal incidence, and 25.7° incidence.

Figure 11(a) shows the reflectance spectra for four different simulated angle-varied octahedron unit cells, 45°, 40°, 35°, and 30°, illuminated with a normal-incidence plane wave. The simulations show a clear blueshift of the reflection peak with decreasing apex angle of the octahedron unit cell, in agreement with experimental results.

These numerical results also display a linear trend between reflection peak position and effective strain, as do the experiments on the as-fabricated and *in-situ* strained nanolattices (see Figure 11(a)). Despite the difference in the actual position of λ_{peak} for the fabricated and simulated angle-varied lattices, the slopes of these lines are very similar. While the simulations appear to over-predict the stopband wavelength, this discrepancy in λ_{peak} position is in large part due to the angle of incident light used for illuminating simulated and fabricated samples; simulated samples are illuminated using plane waves incident at a single angle, and fabricated samples are under illumination from a Gaussian beam with an angular range between 16-35.5°. Simulating nanolattices at an average illumination angle of 25.7° does shift the calculated stopband peak closer to the experimentally-measured peaks. Further discrepancies can be attributed to some non-idealities

in the fabricated samples, like the imperfect uniformity of beams and unit cells and buckling at the joints between unit cells.

The reflection peak observed in our experiments and simulations can be attributed to the 1st order Bragg reflection in the lattice. Bragg's law is formulated as $2d \times cos\theta = n\lambda$, where d is the vertical separation between two layers in the lattice, θ is the angle of the incident beam with the normal line, and n is the order of the Bragg reflection. A monotonic decrease in d from uniaxial strain will result in a monotonic decrease in the resonance wavelength λ_{peak}. This result is in agreement with the general blueshift trend observed both in the numerical and experimental data. Additional reflection peaks observed at longer wavelengths can be attributed to higher orders of the Bragg grating, and are substantially weaker than the main peak of the lattice.

As previously mentioned, the primary peak of the reflection can be attributed to the 1st order Bragg reflection in the lattice. One consequence of this fact is that, increasing the angle of incidence light, relative to the normal, will shift the resonant reflection peak to shorter wavelengths. The color map shown in Figure 12 shows the variation in reflection as a function of incident angle and wavelength for the case of a simulated, unstrained, 45° lattice. It can be clearly seen that as the angle of incidence with respect to the normal increases and the peak resonance wavelength shifts to the shorter values. For further clarification, we superimposed a dashed black line which shows the relation between the incident angle and the resonant wavelength as predicted by the Bragg condition equation. Notice that the line closely follows the resonant wavelengths obtained by numerical simulations. The discrepancies between the peak values of the colormap and the black line are due to the presence of the silicon substrate in the numerically modeled lattice. This substrate redshift the resonance following the Bragg condition, and is more substantial at larger angles of incidence. It should also be noted that the angle of incidence affects the stopband position in a nearly identical manner for the 40°, 35°, and 30° lattices.

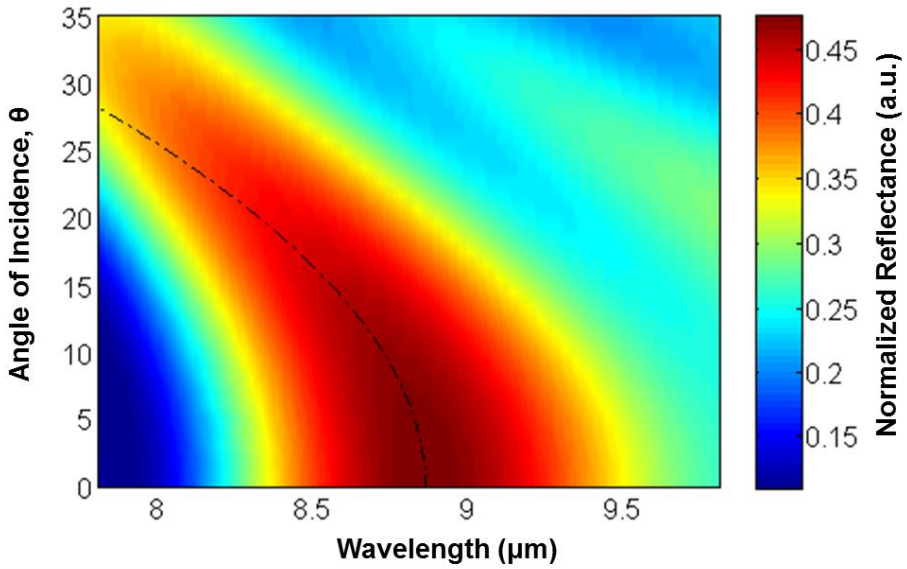

Figure 12. A color map depicting the variation in reflection as a function of incident angle and wavelength for a simulated 45° nanolattice. Note that the angle of incidence here is measured with respect to the line normal to the surface. At larger angles of incidence, the peak in reflection shifts to shorter wavelengths, and the black dashed line overlaying the data shows the relation between the incident angle and the resonant wavelength given by the Bragg condition equation.

2.7. Conclusions and Evolved Critiques

This work demonstrates fabrication and characterization methodologies for 3-dimensional polymer nanolattices, active in the mid-IR range, whose photonic bandgap can be reversibly modulated as a function of uniaxial compressive strain. Opto-mechanical experiments and theory reveal that applied uniaxial compressive strain and the photonic stopband are linearly related, with a maximum attained bandgap shift of ~2.2μm at ~40% compressive strain. These findings imply that architected nanolattices may be utilized for emerging applications including but not limited to optical strain gauges, accelerometer and other mechanical sensors, as well as tunable laser sources and variable filters. And while 3D lattice fabrication using TPL DLW is currently constrained by the minimum axial resolution attainable, restricting the dimensions of the octahedron geometry studied here to unit cell sizes of no less than 2.5μm, advances like stimulated-emission-depletion (STED) DLW are pushing the resolution limits of this technology, and may soon enable the patterning of any arbitrary 3D lattice with photonic properties extended into the visible range.

Chapter 3: Exploring the Photonic Band Gap Properties of 3D Periodic Architectures – Band Gap Properties as a Function of 3D Periodic Architecture

3.1. Outline and Motivation

One of the primary methods for assessing the performance of a PhC is by measuring the quality of its photonic band gap. In general, 3D periodic structures display more complicated bandgap properties than their 2D counterparts and possess more flexibility in applications where the existence of partial stop gaps and a strong suppression rate of some wavelengths are important. Therefore, 3D photonic structures made of low refractive index materials such as polymers can be quite useful in photonic applications. In general, the existence and characteristics of photonic bandgaps depend on such factors as the dielectric contrast and volume fractions, as well as the symmetry, connectivity, and geometrical shape of the periodic dielectric structure.

In this chapter, we report on the optical properties 3D polymeric photonic crystals whose photonic response is dictated by periodic architecture, or more specifically, lattice symmetry. It is noted that local, directional, or "pseudo" band gaps can be easily tuned and even created by changing the size of unit cells comprising the structure. Also discussed is the degree to which finite lattices capture and display the properties predicted by infinite structures and their calculated band structure diagrams.

We study the photonic properties, namely the emergence of pseudo-bandgaps in three different 3D lattice architectures that have been traditionally explored in the context of their mechanical properties. These architectures include octahedron, octet, and tetrakaidecahedron 3D periodic structures, where the octahedron lattice has an underlying simple cubic (SC) structure, the octet lattice has an underlying face centered cubic (FCC) structure, and the tetrakaidecahedron lattice has an underlying base centered cubic (BCC) structure.

3.2. Introduction to Periodic Lattice Architectures

3.2.1. Simple Cubic, Face Centered Cubic, and Base Centered Cubic 3D PhCs

The exploration of 3D PhC structures with an underlying simple cubic lattice symmetry was first undertaken by Sozuer and Haus.[36] The authors explored PhCs formed by dielectric spheres arranged in a

simple cubic lattice and found that, despite the appearance of directional stopbands, no complete bandgaps will occur for this architecture, regardless of the volume fraction of spheres. By inverting the dielectric structure however, and placing air spheres in a dielectric background, they obtained the first full photonic bandgap structure with simple cubic symmetry.

Compared to simple cubic PhCs, face centered cubic structures have been very extensively studied, thanks in part to the ease of fabricating opal and inverse opal structures using self-assembly methods. Opals are formed through the close packing of dielectric spheres which results in a natural fcc lattice, and in-filling the air voids in an opal structure with a dielectric and removing the original sphere material, converting it to air, forms the fcc inverse opal structure. The majority of research on FCC 3D PhCs has focused on opal, inverse opal, and woodpile architectures as the former are amenable to fabrication through self-assembly methods, and the latter can be fabricated using conventional lithographic methods.

The study of photonic band gap properties in base centered cubic PhC structures has been somewhat less extensive compared to its sc and fcc counterparts. However, the band gap properties of void-based bcc PhCs in a solidified transparent polymer have been studied,[37] as have BCC-based gyroid structures, which have been demonstrated to have a complete gap almost as wide as that of diamond.[38]

3.2.2. Octahedron, Octet, and Tetrakaidecahedron Lattice Architectures

In general, most of the research performed on the various 3D cubic symmetry PhCs has been computational, assessing which combination of architecture and high index material will yield the largest complete bandgap. Of the experimental studies done on SC, FCC, and BCC PhCs, the actual architectures have been largely limited to structures with unit cells of limited complexity, like spheres or stacked beams. With the advent of two photon lithography direct laser writing however, the opportunity exists to create 3D PhCs with arbitrarily shaped unit cells and underlying lattice symmetry. As such, we fabricate and characterize 3D PhCs composed of polymer octahedron, octet, and tetrakaidecahedron unit cells—architectures whose photonic properties have not yet been studied (with exception of the work presented in Chapter 2).

Schematics of the octahedron unit cell, lattice, and underlying simple cubic symmetry are shown in Figure13(a-c). It should be noted that lattices are constructed along Cartesian coordinates with the PhC surface pointing along the (001) direction.

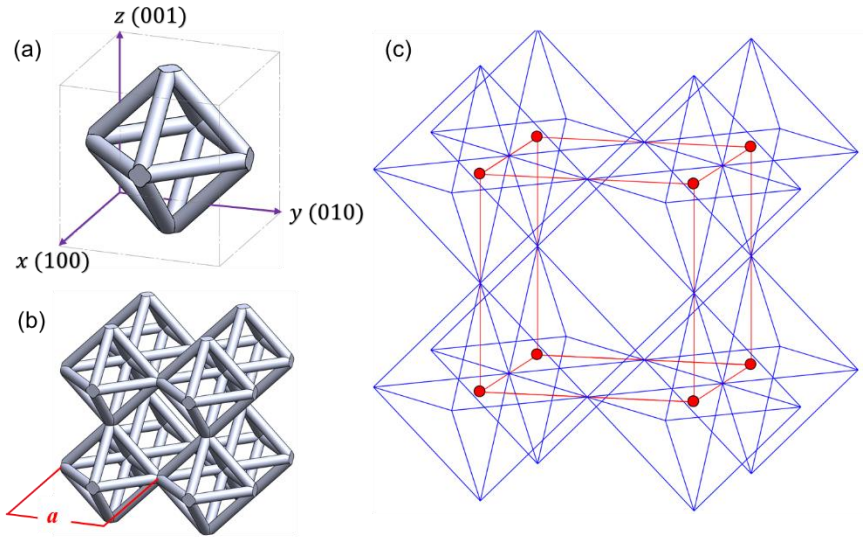

Figure 13. Schematic of an octahedron simple cubic PhC lattice. (a) A view the octahedron unit cell with cylindrical beams. (b) A representation of a 2x2x2 octahedron unit cell lattice. The lattice period is given by the parameter *a*. (c) Representation of the underlying simple cubic lattice symmetry in the octahedron-based PhC architecture.

Schematics of the more complex octet unit cell, lattice, and underlying face centered cubic symmetry are shown in Figure14(a-c). It should again be noted that lattices are constructed along Cartesian coordinates with the PhC surface pointing in the (001) direction.

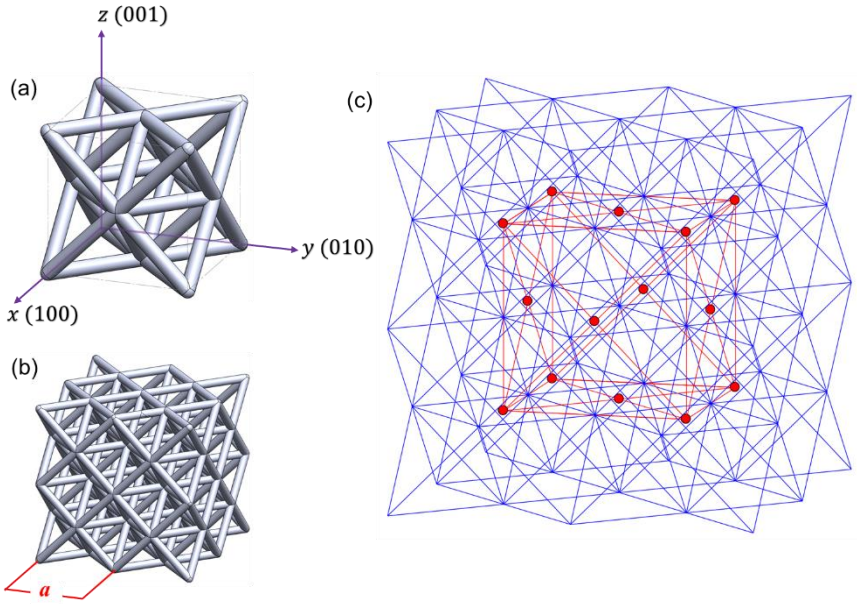

Figure 14. Schematic of an octet face centered cubic PhC lattice. (a) A view the octet unit cell with cylindrical beams. (b) A representation of a 2x2x2 octet lattice. The lattice period is given by the parameter *a*. (c) Representation of the underlying FCC symmetry in the octet-based PhC architecture.

Finally, schematics of the tetrakaidecahedron unit cell, lattice, and underlying base centered cubic symmetry are shown in Figure15(a-c). It should again be noted that lattices are constructed along Cartesian coordinates with the PhC surface pointing in the (001) direction.

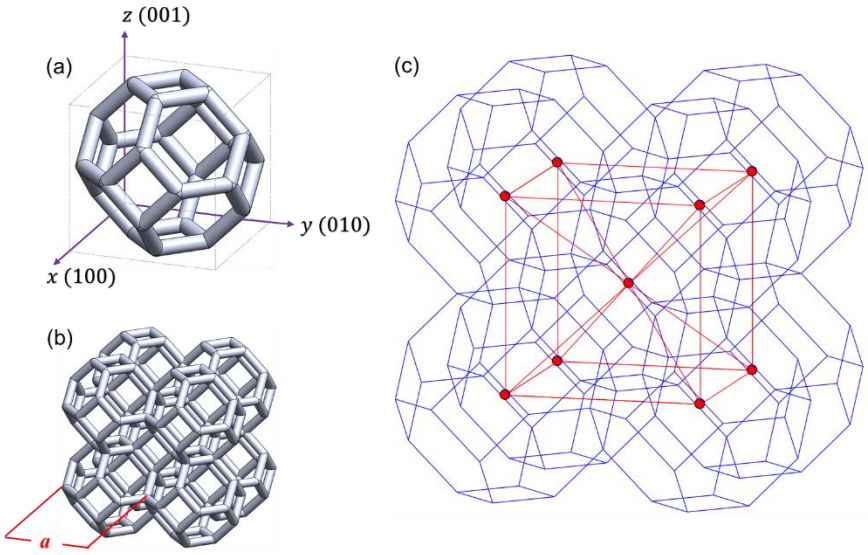

Figure 15. Schematic of a tetrakaidecahedron base centered cubic PhC lattice. (a) A view the tetrakaidecahedron unit cell with cylindrical beams. (b) A representation of a 2x2x2 tetrakaidecahedron lattice. The lattice period is given by the parameter *a*. (c) Representation of the underlying BCC symmetry in the tetrakaidecahedron-based PhC architecture.

3.3. Fabrication of 3D Nanolattices PhCs

As described in detail previously, nanolattice PhCs were fabricated out of the acrylate-based "IP-Dip" photosensitive monomer, using the direct laser writing two-photon lithography (DLW TPL) system developed by Nanoscribe GmbH. For this DLW TPL process, the 3D periodic octahedron, octet, and tetrakaidecahedron architectures were created using MATLAB and the computer aided design (CAD) program SolidWorks, with lattice beams defined in slices, so that writing could be performed in a layer-by-layer fashion.[39] The layer-by-layer writing scheme allows for the generation of beams possessing nearly circular cross-sections (see ref. [39] for additional detail) , as compared to the octahedron lattices described in Chapter 2 which had elliptical beams. PhC samples were written on a 500μm thick silicon chip, and following the photoresist exposure step, 3D polymer structures were developed for 30 minutes in propylene glycol mono-methyl ether acetate (PGMEA) followed by a 5-minute rinse in isopropyl alcohol. To prevent lattice collapse or excessive shrinkage due to capillary forces during the drying step, lattices were critical point dried using a TousimisAutosamdri-815B, Series B critical point dryer.

Lattices were designed to be approximately 130μm x 130μm in x-y extent, and fabricated with varying heights, ranging from 10 unit cell layers in z-extent to 20 unit cell layers. Each of the three lattice architectures under study were fabricated with two different unit cell sizes, so that the stopband position could be assessed on the basis of periodicity as well as lattice architecture. Octahedron lattices were fabricated with unit cells sizes of approximately 3.3 μm and 4.75 μm. Octet lattices were made with unit cells sizes of approximately 3.5 μm and 4.75 μm, and tetrakaidecahedrons were fabricated with unit cells sizes of approximately 4.3 μm and 6.75 μm. Though unit cell size, or lattice periodicity, was varied for all 3D periodic architectures in this study, the cylindrical beam dimensions remained constant between all structures, with an approximate diameter of 850 nm. Representative images of as-fabricated octahedron, octet, and tetrakaidecahedron structures are presented in Figure 16(a-c).

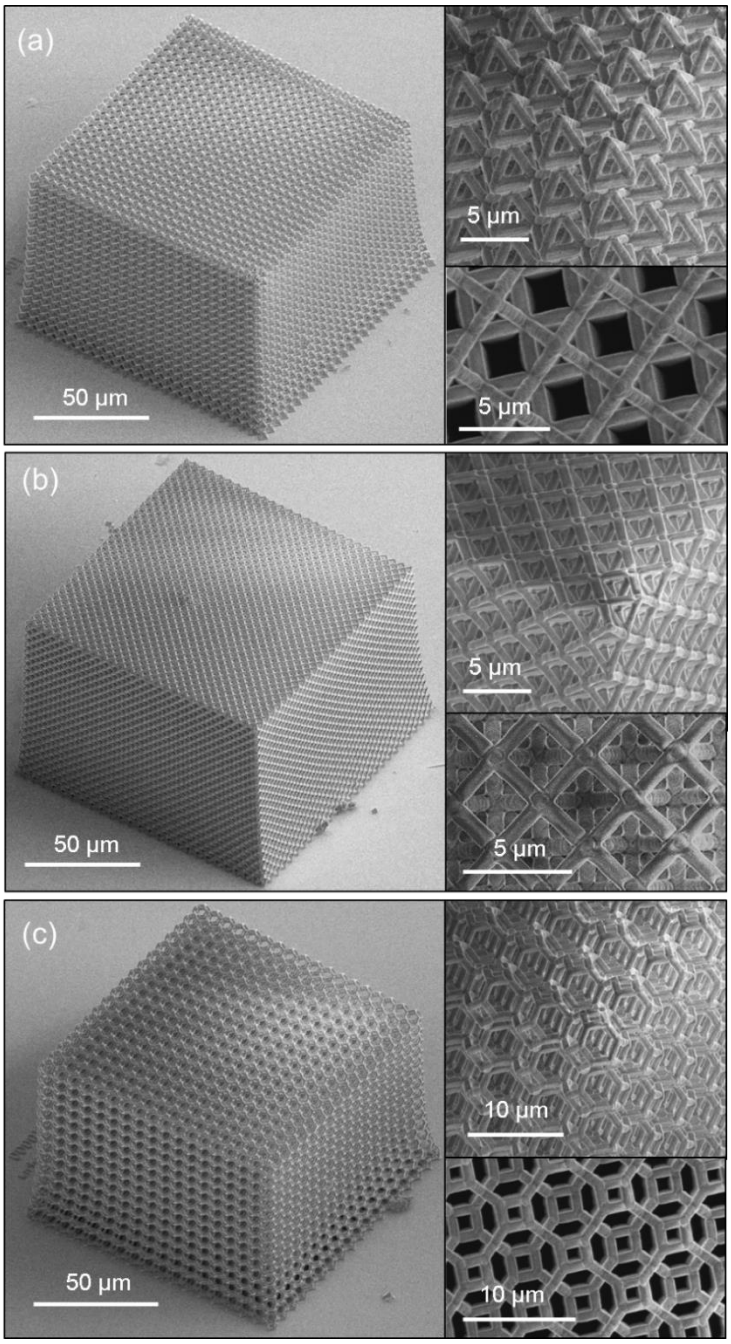

Figure 16. Representative images of as-fabricated octahedron, octet, and tetrakaidecahedron PhC lattices. (a) Full scale octahedron nanolattice with periodicity a = 4.75µm. Insets show an enlarged lattice corner and round, cylindrical beams, and a top down view of the simple cubic octahedron arrangement. (b) Full scale octet nanolattice with periodicity a = 4.75µm. Insets show an enlarged lattice corner and round, cylindrical beams, and a top down view of the face centered cubic octet arrangement. (c) Full scale tetrakaidecahedron nanolattice with periodicity a = 6.75µm. Insets show an enlarged lattice corner and round, cylindrical beams, and a top down view of the base centered cubic tetrakaidecahedron arrangement.

It should be noted that one particular benefit of 3D PhC fabrication using TPL DLW is that any lattice orientation is possible, so long as it can be designed. This is in contrast to methods like self-assembly where

periodic arrangements will typically be close packed, resulting in FCC PhCs with a (111) crystal surface arrangement, as is the case with opal structures.

3.4. Optical characterization of Octahedron, Octet, and Tetrakaidecahedron Nanolattices PhCs

Reflection spectroscopy is a customary optical characterization technique which reveals stop bands as peaks of increased reflection, indicating the nonzero imaginary component of the wavevector for those frequencies contained in the stop band. While all lattices under study are purely polymeric, possessing a relatively low dielectric contrast with air compared to a high-index material like silicon (the refractive index of IP-Dip is n = 1.49 in the mid-IR), we nonetheless expect at least a directional stopband to be present in these PhC structures.

The micron-scale unit cell sizes of our lattices suggest that the PhCs will exhibit a bandgap in the infrared range. As such, we used Fourier Transform Infrared (FTIR) microspectroscopy in reflectance mode to measure stopband position. Spectra were acquired on a Nicolet iS50 FT-IR spectrometer equipped with a Nicolet Continuum Infrared Microscope. The microspectrometer Cassegrain lenses limited incident light to an off-normal annulus with an angular range between 16°-35.5°. All spectra were collected against a smooth, fully reflective gold mirror background.

3.4.1. Reflectivity Spectra with respect to Geometry and Periodicity

In Figure17(a) we have two representative reflectivity spectra plotted for simple cubic PhC lattices of octahedron unit cells with periodicities equal to 3.3μm and 4.75μm. For the lattice with average periodicity of 3.3μm, a significant peak in normalized reflectance emerges, and is centered at 6.41μm, which corresponds to the first order stopband. For the lattice with an average period of 4.75μm, the first order stopband appears at 9.69μm.

Consistent with our findings from Chapter 2, stop band position is highly dependent on lattice periodicity, and shifts to shorter wavelengths for nanolattices with decreasing unit cell size. In Figure 17(a) we also observe peaks in reflectance to the right of our first order stopband which are smaller in amplitude than the primary reflectance peak. For the a = 4.75μm octahedron lattice we observe secondary reflectance

peaks at 4.89µm 3.20µm, and these positions are consistent with 2nd and 3rd order Bragg reflections respectively.

It should also be noted that most of the sharp, intense dips we observe in our nanolattice PhC spectra are not optical features belonging to the nanolattice architecture, but are instead absorptions from the polymer material. Some of these material absorptions pass through the relevant stopband features of the lattice, like the dips at 9.39µm and 10.13µm in the 4.75µm octahedron lattice, but these are actually caused by excited vibrational modes of the IP-Dip polymer (see Appendix A for more detail).[40]

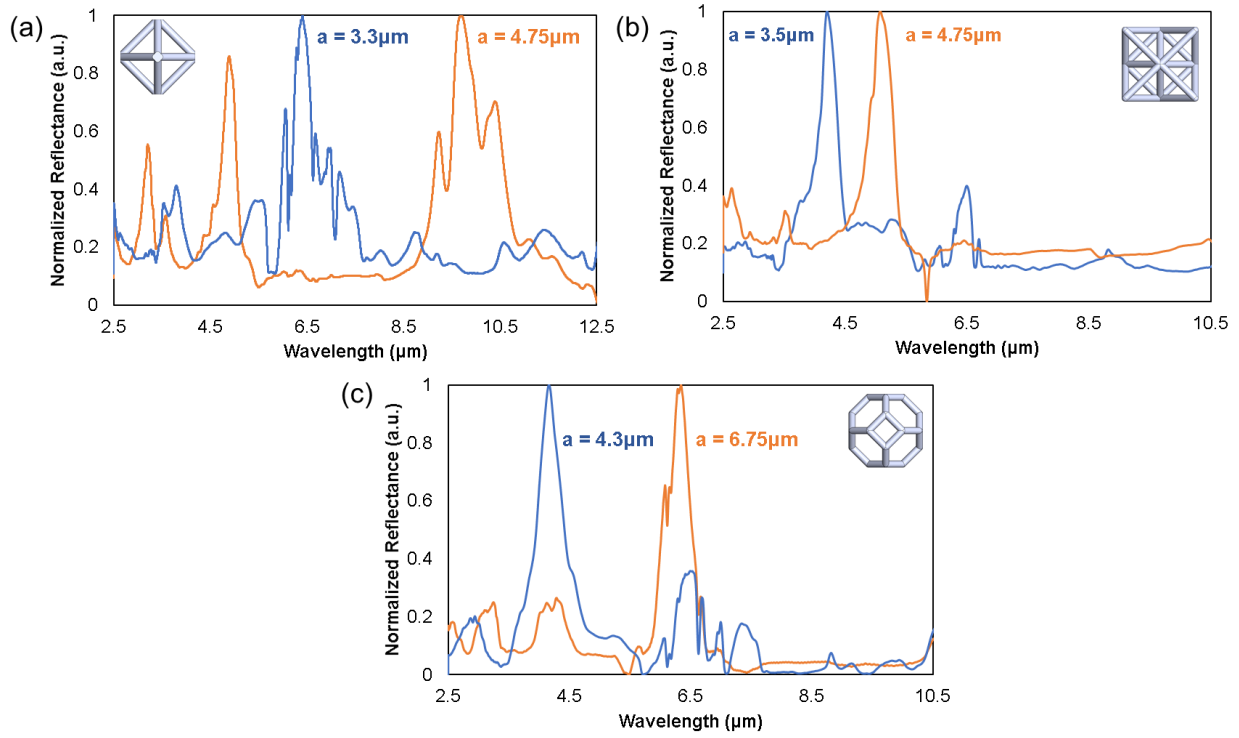

Figure 17. FTIR reflectance spectra for octahedron, octet, and tetrakaidecahedron nanolattice PhCs. (a) Normalized reflectance spectra for octahedron nanolattice PhCs with 3.3µm and 4.75µm periodicities. (b) Normalized reflectance spectra for octet nanolattice PhCs with 3.5µm and 4.75µm periodicities. (c) Normalized reflectance spectra for tetrakaidecahedron nanolattice PhCs with 4.3µm and 6.75µm periodicities.

In Figure17(b) we have two representative reflectivity spectra plotted for face centered cubic PhC lattices of octet unit cells with average periodicities equal to 3.5µm and 4.75µm. For the lattice with a = 3.5µm, a significant peak in normalized reflectance emerges at 4.20µm, which corresponds to a first order stopband. For the lattice with a = 4.75µm, the first order stopband appears at 5.07µm. We can again note

that stopband position is dependent on lattice period, with a decreasing unit cell size leading to blueshifting of the stopband peak.

Finally, in Figure17(c) we have two representative reflectivity spectra plotted for base centered cubic PhC lattices of tetrakaidecahedron unit cells with average periodicities equal to 4.3μm and 6.75μm. For the lattice with a = 4.3μm, a significant peak in normalized reflectance emerges at 4.16μm, which corresponds to a stopband. For the lattice with a = 6.75μm, a stopband appears at 6.34μm. These results again corroborate that, regardless of lattice architecture, stopband position is highly influenced by lattice period, and by decreasing the unit cell size of any architecture with any underlying lattice symmetry, the center position of the stopband will blueshift.

3.5. Comparing Experimental Reflectivity to Calculated Photonic Band Structure

3.5.1. Photonic Band Structure Calculations

In order to carry out a comparison of our experimental results with theory, we have calculated the photonic band structures associated with our three unique cubic PhC systems using the plane wave expansion (PWE) method.[41] In PWE, Maxwell's equations are combined to obtain the differential wave equation that governs the propagation of the electromagnetic waves within a PhC structure, and assumes an infinite, ideal photonic crystal. Photonic band structures for octahedron, octet, and tetrakaidecahedron architectures were simulated and analyzed using the commercially available BandSOLVE simulation engine, which utilizes an optimized implementation of the PWE technique for periodic structures.

To construct the photonic bands, we take wave vectors from the edges of the underlying lattice symmetry irreducible Brillouin zones (as commonly done in the photonic literature[42]), where particular points along the Brillouin zone path correspond to different magnitudes and directions of the wave-vector $\vec{k}$. For each chosen $\vec{k}$ path, the corresponding eigenvalues are calculated, forming an ascending set of n eigenvalues. In grouping the eigenvalues and plotting them as a function of $\vec{k}$, band diagrams are generated. In general, we note that position of the midgap, or center of a bandgap, is determined by the edge of the Brillouin zone, and therefore it is highly dependent on direction.[43] Furthermore, gap width (the frequency range of the bandgap) is directly proportional to the index of materials forming the PhC.

Consequently, we expect that with a small polymer index of n = 1.49, the widths of our bandgaps for all lattice symmetries will be rather small.

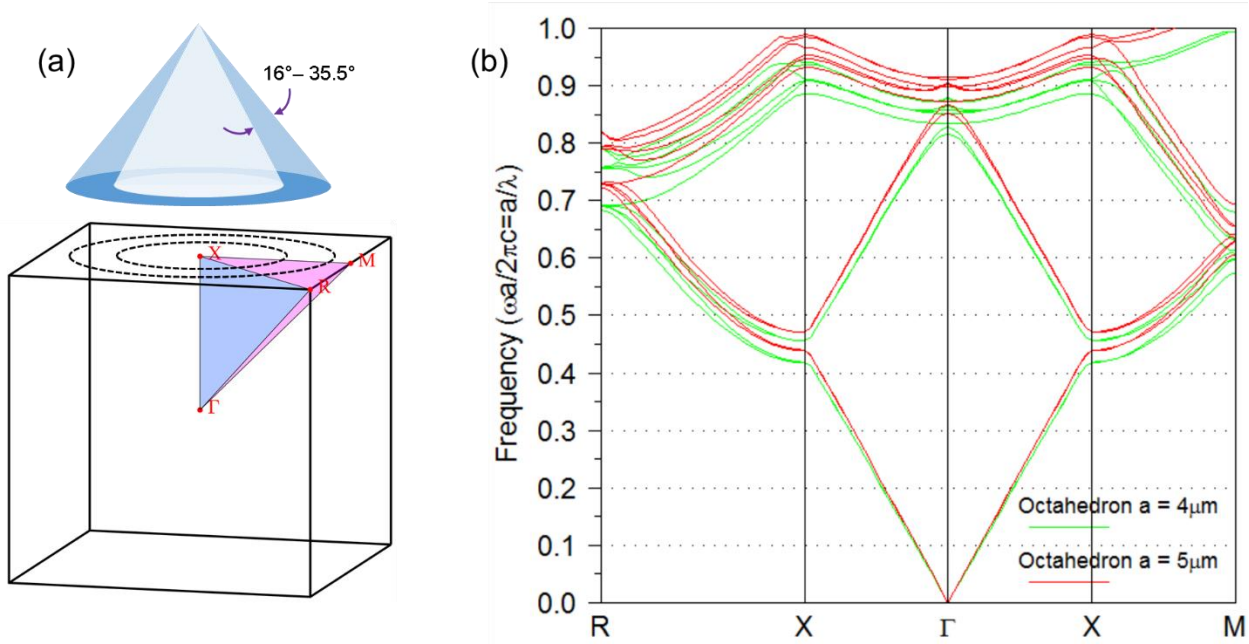

Figure 18. Brillouin zone and band structure calculated for the octahedron simple cubic lattice. (a) The Brillouin zone for a simple cubic PhC set relative to the wave vectors incident on the simple cubic octahedron lattice during FTIR reflectance measurements. The angular range of the incident light annulus means wave vectors will interface with the Γ-X-R and Γ-X-M planes (denoted in blue and pink). (b) Band structure calculated for the octahedron simple cubic lattice probing the Γ-X-R and Γ-X-M directions. Bands are compared for lattices with a periodicity of 4μm and 5μm.

In Figure 18(a) we present the Brillouin zone for a simple cubic (SC) with distinct k-paths and end points labelled Γ, X, R, and M. While Γ, X, R, and M are the general high symmetry points for simple cubic crystals, we chose the particular band structure k-paths shown in Figure 18(b) deliberately for our calculations. In our fabricated octahedron simple cubic PhCs, the top surface is oriented in the (001) direction, which corresponds to the ΓX path, or probing the PhC at normal incidence. Since the Cassegrain lens arrangement in the FTIR microscope prevents sampling the PhC at normal incidence, the angular span of incident annular light means that we actually probe the PhCs in the Γ-X-R and Γ-X-M planes simultaneously (the blue and pink triangles in Figure 18(a)). We calculated the band structure for octahedron simple cubic PhCs along the Γ-X-R and Γ-X-M paths, and observe that the first four bands in X-R and X-M appear rather symmetric. More significantly, a substantial bandgap opens between bands 2 and 3 at the Γ-X edge, and this bandgap continues to propagate along X-R and X-M, though the bandgap

width diminishes and moves to higher frequencies the further we move in X-R and X-M. It is likely that the peaks we observe in our FTIR reflectance spectra are due to this propagating bandgap in the X-R and X-M directions. We also note that, while the overall band structure shape is identical for octahedron lattices with 4μm and 5μm periodicities, band and bandgap positions are all shifted to higher frequencies (longer wavelengths) as periodicity increases. This is likely because the beam diameter used in both simulations is set to 850nm, meaning that the 5μm lattice possesses a slightly lower fill fraction compared to the 4μm lattice.

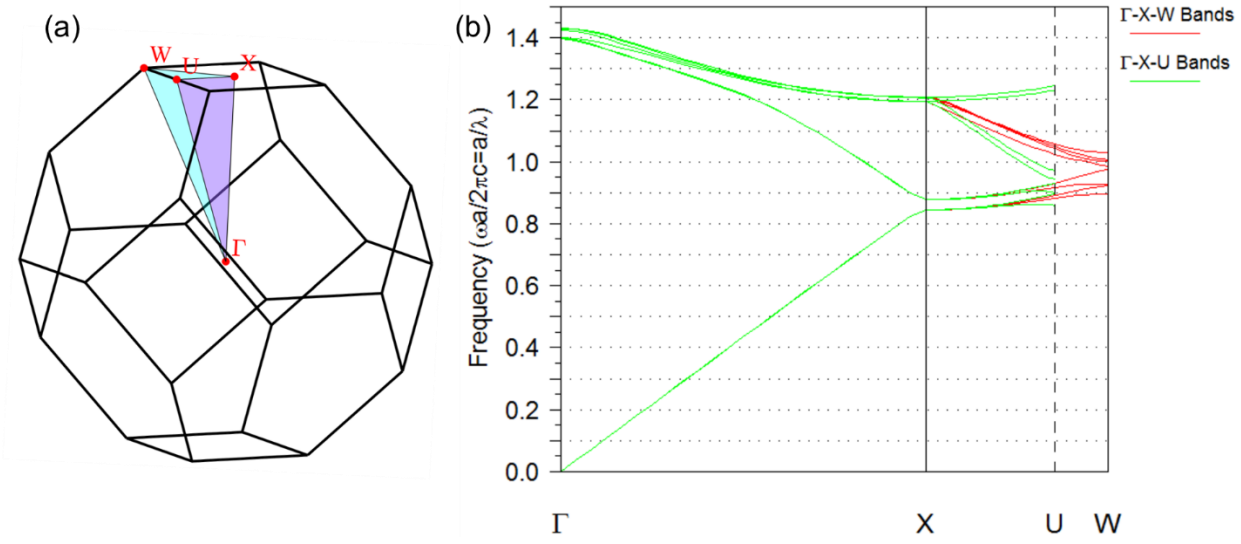

Figure 19. Brillouin zone and band structure calculated for the octet face centered cubic lattice. (a) The Brillouin zone for a face centered cubic PhC. The Γ-X-U and Γ-X-W planes (denoted in purple and light blue) are singled out as the planes which coincide with wave vectors of light incident on the octet PhC from FTIR reflectance measurements. (b) Band structure calculated for the octet FCC lattice along the Γ-X-U and Γ-X-W directions. Bands along the X-U and X-W directions are overlaid to show their similarities.

In Figure 19(a) we present the Brillouin zone for a FCC lattice with Γ, X, U, and W high symmetry points. In our fabricated octet FCC PhCs, the top surface is oriented in the (001) direction, which again corresponds to the ΓX path. In FTIR measurements, the annular cone of infrared light is incident on the PhC surface such that the incident and diffracted wave vectors coincide with planes passing through both the Γ-X-U and Γ-X-W points (purple and light blue triangles in Figure 19(a)). We calculate the band structure for octet face centered cubic PhCs along the Γ-X-U and Γ-X-W paths, and observe that, along the X-U and X-W segments, the first four bands display significant overlap. Furthermore, a substantial bandgap

opens between bands 2 and 3 at the Γ-X edge, and this bandgap continues to propagate in both the X-U and X-W directions, though the bandgap width diminishes and moves to higher frequencies the further we move along these k-paths. The peaks we observed in our FTIR reflectance spectra for octet PhC samples are likely due to the bandgap which appears in both the X-U and X-W directions.

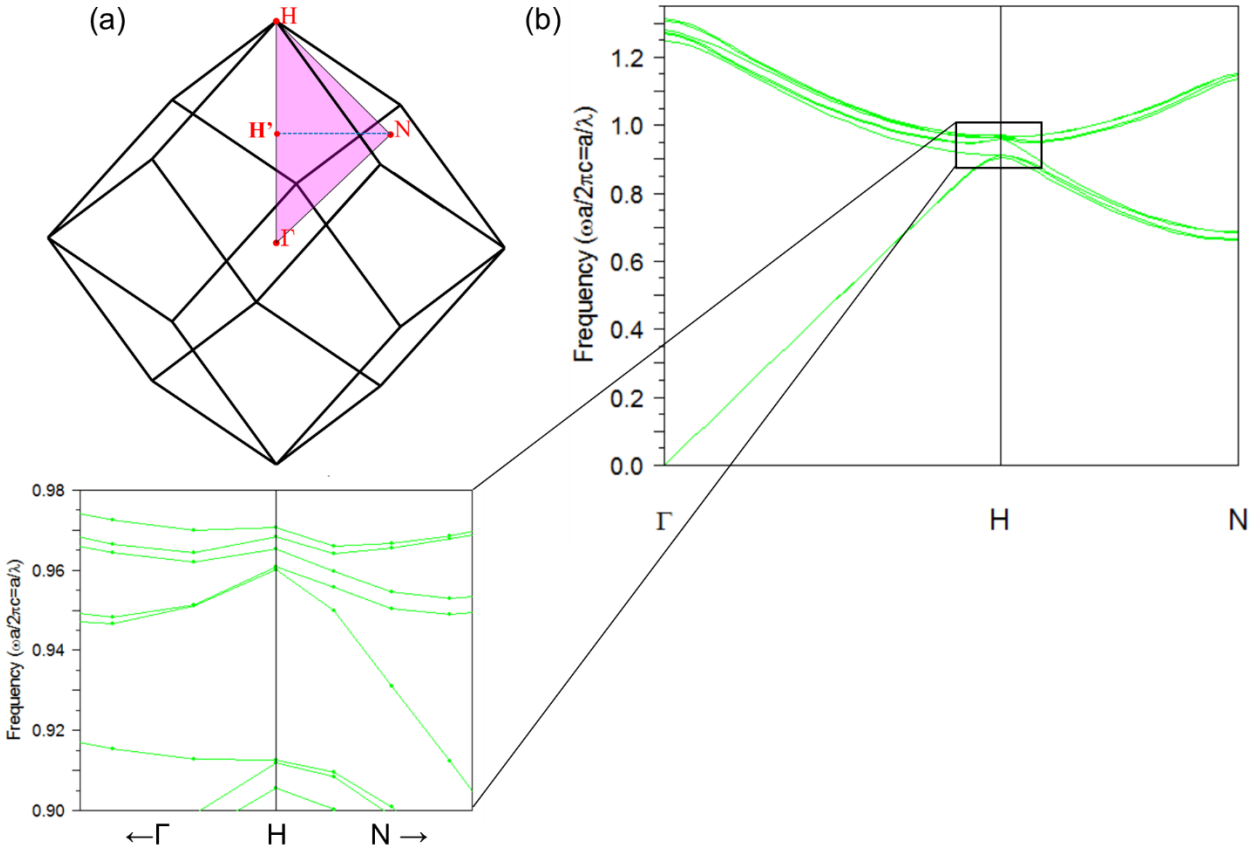

Figure 20.Brillouin zone and band structure calculated for the tetrakaidecahedron base centered cubic lattice. (a) The Brillouin zone for a base centered cubic PhC. The Γ-H-N plane (denoted in pink) is singled out as the plane which coincides with wave vectors of light incident on the tetrakaidecahedron PhC from FTIR reflectance measurements. (b) Band structure calculated for the tetrakaidecahedron BCC lattice along the Γ-H-N direction. Inset shows an expanded view of bands and band gaps around the H point.

In Figure 20(a) we present the Brillouin zone for a BCC lattice with Γ, H, and N high symmetry points. In our fabricated tetrakaidecahedron BCC PhCs, the top surface is oriented in the (001) direction, which corresponds to the ΓH' path (the H point actually denotes the (002) direction so, H', which sits along the same k-path, will refer to (001) for our purposes). In FTIR measurements, the annular cone of infrared light is incident on the PhC surface such that the incident and diffracted wave vectors coincide with the plane passing through the points Γ-H-N (the pink triangle in Figure 20(a)). We calculate the band structure for

tetrakaidecahedron base centered cubic PhCs along the Γ-H-N path, and observe a small bandgap opening between bands 6 and 7 at the Γ-H edge (see the expanded band plot in Figure 20(b)). This bandgap continues to propagate along the H-N direction, shifting to higher frequencies while the bandgap width increases, and then contracts the further we move along this k-path. The peaks we observed in our FTIR reflectance spectra for tetrakaidecahedron PhC samples are likely due to the appearance of this bandgap in the H-N direction.

3.5.2. Direct Comparison of Peak Reflectivity and Bandgap Position

Now that we have band structure calculations for all lattice architectures, we can directly compare the position of experimentally measured stopbands relative to the expected stopband position for an ideal PhC. While FTIR reflectance measurements provide precise and resolved frequency information, these spectra give convoluted momentum space information, since measurements are taken over range of angles. As such, we can plot the center frequency position of experimentally measured stopbands over a band structure diagram, but as we cannot discern wave vector position precisely, each stopband data point will be plotted over the angular range of the FTIR, 16° – 35.5°, for multiple directions (and will appear as a line instead of a point on the plot).

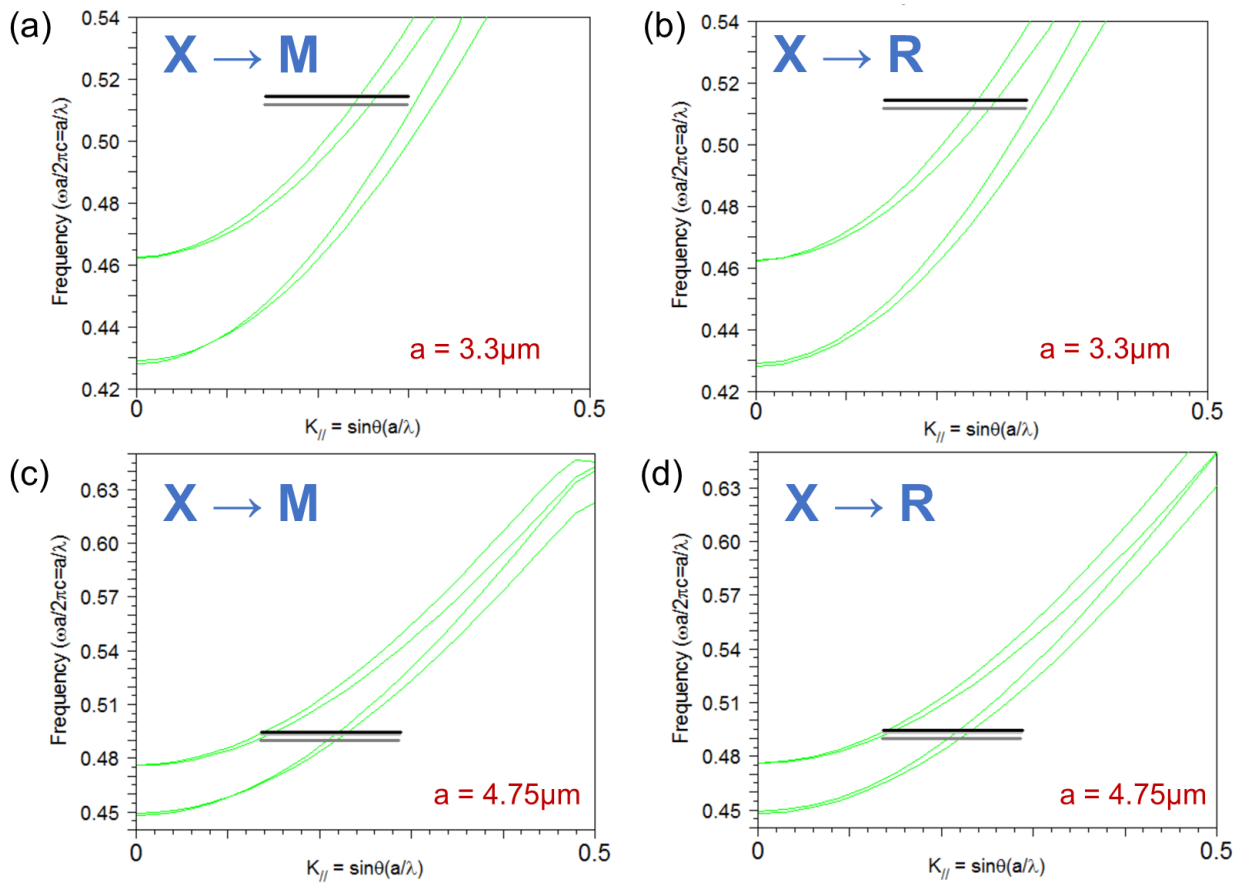

Figure 21. Calculated bands and experimental reflectivity peaks for simple cubic octahedron nanolattice PhCs. (a) Calculated bands (green lines) along the X-M direction and experimental reflectivity peaks (grey and black lines) for octahedron lattices with 3.3μm periodicity. (b) Calculated bands (green lines) along the X-R direction and experimental reflectivity peaks (grey and black lines) for octahedron lattices with 3.3μm periodicity. (c) Calculated bands (green lines) along the X-M direction and experimental reflectivity peaks (light grey, dark grey, and black lines) for octahedron lattices with 4.75μm periodicity. (d) Calculated bands (green lines) along the X-R direction and experimental reflectivity peaks (light grey, dark grey, and black lines) for octahedron lattices with 4.75μm periodicity.

In Figure 21(a-b) we have plotted the center peak position of experimentally measured stopbands for two octahedron lattice samples (grey and black lines) with an approximate unit cell size of 3.3μm, relative to the bands for an ideal 3.3μm octahedron PhC. The width of the lines represents the angular range of the incident wave vector, and because incident light impinges on the PhC in an annulus, we cannot separate whether the observed peak in reflectivity is due to the bandgap present in the X-M or X-R directions, or properly weight the contribution of direction on the evolution of the bandgap. However, we observe that in both directions, the experimental reflectivity peaks substantially overlap the bandgap region. While an ideal experimental sample reflectivity would be centered in the bandgap at a particular frequency, we can

attribute deviations in reflectivity peak position to inhomogeneities in unit cell size throughout the PhC height. During lattice fabrication, some measure of lattice shrinkage is inevitable, resulting in the unit cells affixed to the substrate being larger than unit cells near the lattice top, meaning peak reflectivity is actually a convolution of the stopband positions of PhCs with multiple periodicities.

In Figure 21(c-d) we plot the center peak position of experimentally measured stopbands for three octahedron lattice samples (light grey, dark grey, and black lines) with an approximate unit cell size of 4.75µm, relative to the bands for an ideal 4.75µm octahedron PhC. We observe that in both the X-M and X-R directions, experimental reflectivity peaks noticeably overlap the bandgap region, and that is overlap is more substantial relative to the plots in Figure 21(a-b) for the 3.3µm octahedron PhCs. One reason for this is that the 4.75µm samples are more homogeneous throughout their height, and as such, better approximate an ideal simple cubic octahedron lattice with constant periodicity.

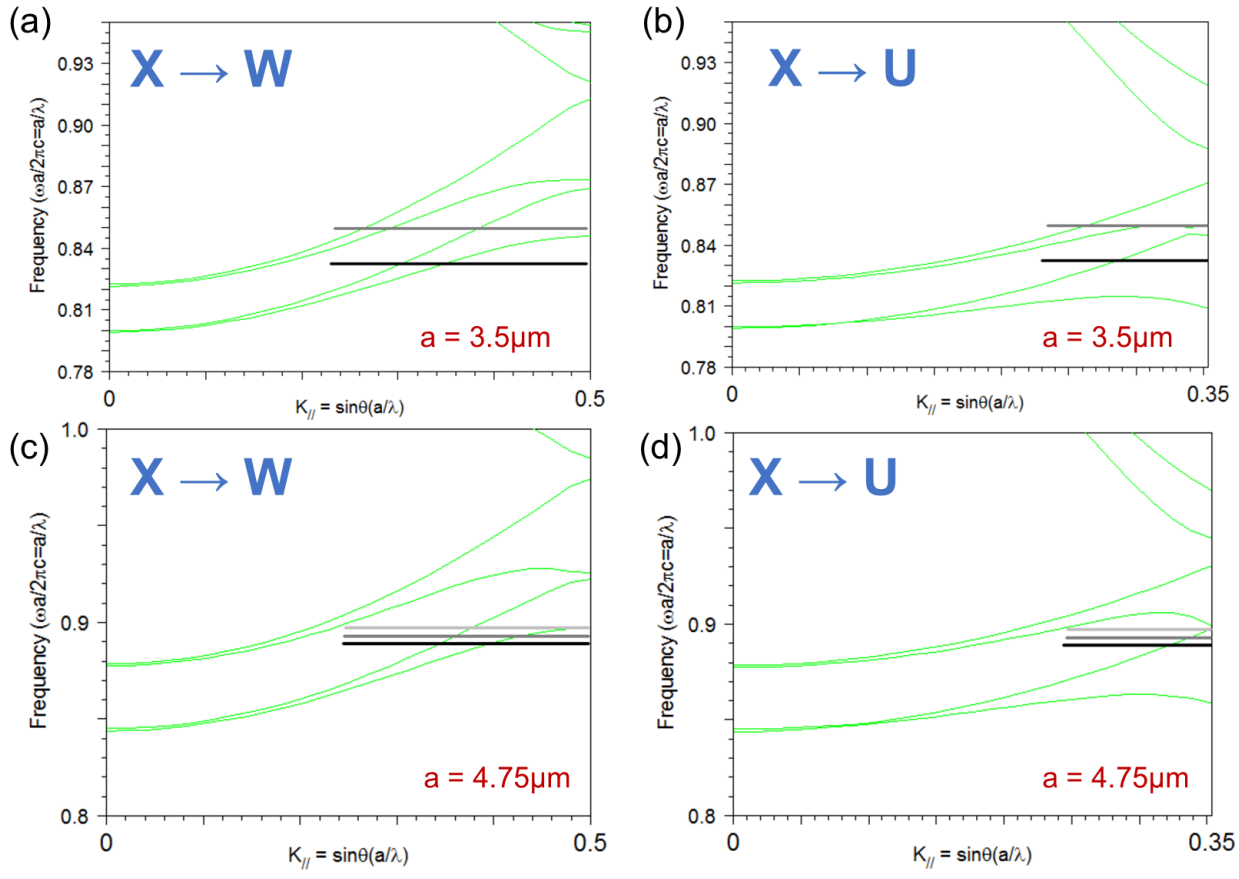

Figure 22. Calculated bands and experimental reflectivity peaks for face centered cubic octet nanolattice PhCs. (a) Calculated bands (green lines) along the X-W direction and experimental reflectivity peaks (grey and black lines)

for octet lattices with 3.5µm periodicity. (b) Calculated bands (green lines) along the X-U direction and experimental reflectivity peaks (grey and black lines) for octet lattices with 3.5µm periodicity. (c) Calculated bands (green lines) along the X-W direction and experimental reflectivity peaks (light grey, dark grey, and black lines) for octet lattices with 4.75µm periodicity. (d) Calculated bands (green lines) along the X-U direction and experimental reflectivity peaks (light grey, dark grey, and black lines) for octet lattices with 4.75µm periodicity.

In Figure 22(a-b) we plot the center peak position of experimentally measured stopbands for two octet lattice samples (grey and black lines) with an approximate unit cell size of 3.5µm, relative to the bands for an ideal 3.5µm octet PhC. we observe that in both the X-W and X-U directions, experimental reflectivity peaks overlap the bandgap region, but are far from centered over the gap at their respective frequencies. This is likely caused by significant inhomogeneities in periodicity throughout the PhC volume. It should be noted that the X-U k-path is shorter than the X-W k-path, and consequently FTIR reflectance measurements actually sample regions of the 2nd FCC Brillouin zone (not shown here) as well as the 1st Brillouin zone.

Figure 22(c-d) presents the experimental reflectivity peaks for three octet PhC lattices (light grey, dark grey, and black lines) with a periodicity of 4.75µm plotted with the band structure of an ideal 4.75µm octet PhC. Similar to what we observe in Figure 22(a-b), experimental measurements overlap with the bandgap at the respective center frequencies for the reflectivity peaks. However, all of our experimentally measured octet samples present larger deviations in k-path position compared to our experimentally measured octahedron samples, and the reasons for this observation must be explored in a subsequent study.

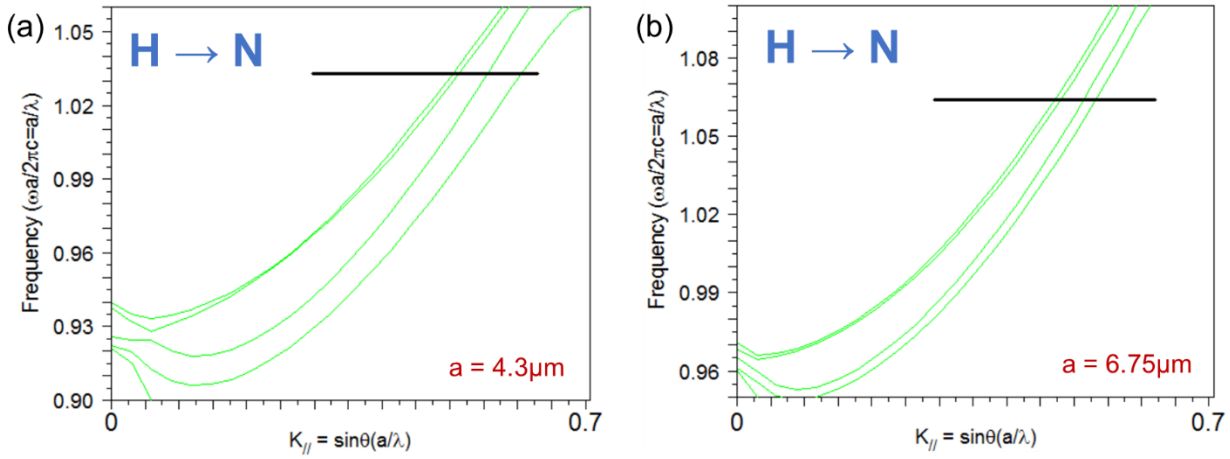

Figure 23. Calculated bands and experimental reflectivity peaks for base centered cubic tetrakaidecahedron nanolattice PhCs. (a) Calculated bands (green lines) along the H-N direction and experimental reflectivity peaks (black lines) for tetrakaidecahedron lattices with 4.3µm periodicity. (b) Calculated bands (green lines) along the H-N direction and experimental reflectivity peaks (black lines) for tetrakaidecahedron lattices with 6.75µm periodicity.

In Figure 23(a) we plot the center peak position of an experimentally measured stopbands for a tetrakaidecahedron lattice sample (black line) with an approximate unit cell size of 4.3μm, relative to the bands for an ideal 4.3μm tetrakaidecahedron PhC. We observe that the experimental reflectivity peak overlaps the bandgap region in its entirety, unlike the behavior observed in octahedron and octet lattices. In Figure 23(b) we plot the center peak position of an experimentally measured stopbands for a tetrakaidecahedron lattice sample (black line) with an approximate unit cell size of 6.75μm, relative to the bands for an ideal 6.75μm tetrakaidecahedron PhC. We again observe that the experimental reflectivity peak overlaps the bandgap region in its entirety. However, for both periodicities, the experimental reflectivity is not centered over the band gap region for each individual center frequency. An implication of this is that non-idealities likely exist in the tetrakaidecahedron nanolattices, but the angular window for FTIR measurements is wide enough that the likelihood of hitting the correct k-vectors which coincide with the band gap region is substantially large.

3.5.3. Comparing the FWHM of Reflectivity Peaks to Calculated Bandgap Width

If it were possible to fabricate a perfect PhC, free of defects and irregularities in unit cell size, and containing enough layers to be considered infinite in every direction, then we would expect experimental peaks in reflectivity to look like a rectangular pulse function, with a width corresponding to the calculated bandgap width, and a flat top, representative of the fact that within the bandgap, reflectivity should be equal over the whole frequency range of the gap.[43,44] Realistically though, the experimentally measured reflectivity peaks of a 3D PhC will not present a flat top, even in the absence of disorder, precisely because real PhCs are finite.[44] The extinction length for frequencies close to the stopband edge is larger than for the stopband center, and consequently, finite PhCs will possess reflectivity peaks (and transmission dips) that have a rounded shape.[44,45] Also affecting the final shape and width of the reflectivity peak is the presence of defects or disorder in a PhC lattice. Differences in unit cell size through the height of the PhC lattice, as well as fabrication imperfections, will affect experimentally obtained reflection spectra. Reflection peaks

will become less intense and asymmetric, and may become spectrally wider due to lattice defects and disorder.[44]

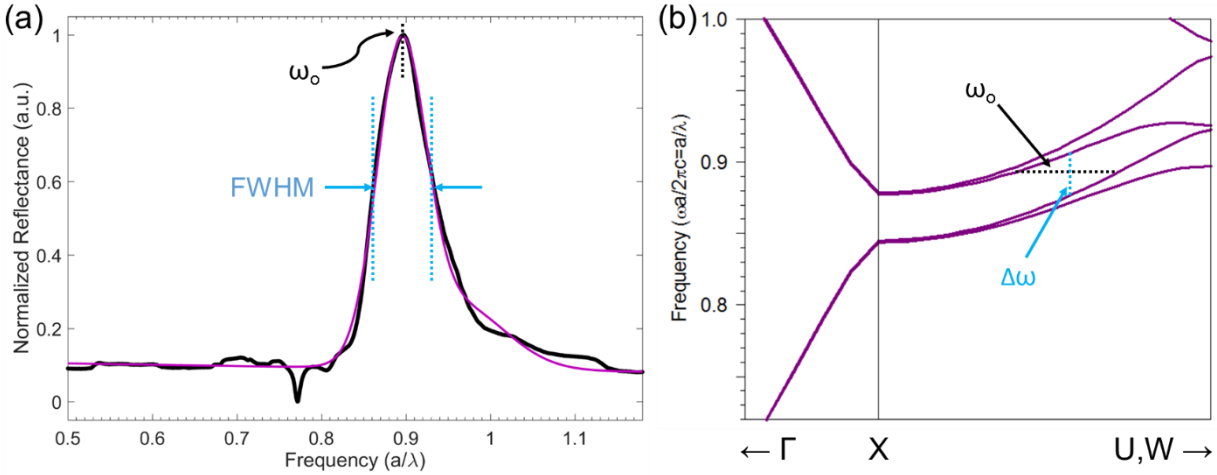

Figure 24. Outline for comparing the FWHM of experimental reflectivity peaks to the calculated bandgap width Δω. (a) Experimental reflectivity peaks are fit to a Gaussian curve and the full width at half maximum is measured around the center peak frequency ω_o. (b) At the same center frequency we measure the bandgap width, Δω, from the PhC band structure diagrams.

Another manner by which we can assess the quality of reflection peaks, namely how well they correspond to the expected bandgap properties, is by comparing the full width at half maximum (FWHM) of the experimental peaks, to the corresponding calculated bandgap width Δω, at the relevant center gap frequency. This process is outlined in Figure 24(a-b). We take the experimentally obtained stopband peaks for PhC lattices of all three underlying symmetries, and fit the data to a Gaussian model, from which we can extract the FWHM of the peak (Figure 24(a)). At the corresponding center frequency, ω_o, we measure the bandgap width (Figure 24(b)), and compare the FWHM values to the Δω values for octahedron, octet, and tetrakaidecahedron PhCs. The closer the two values are, the more ideal the PhC sample, as defects and disorder lead to the widening of bandgap reflectivity peaks.

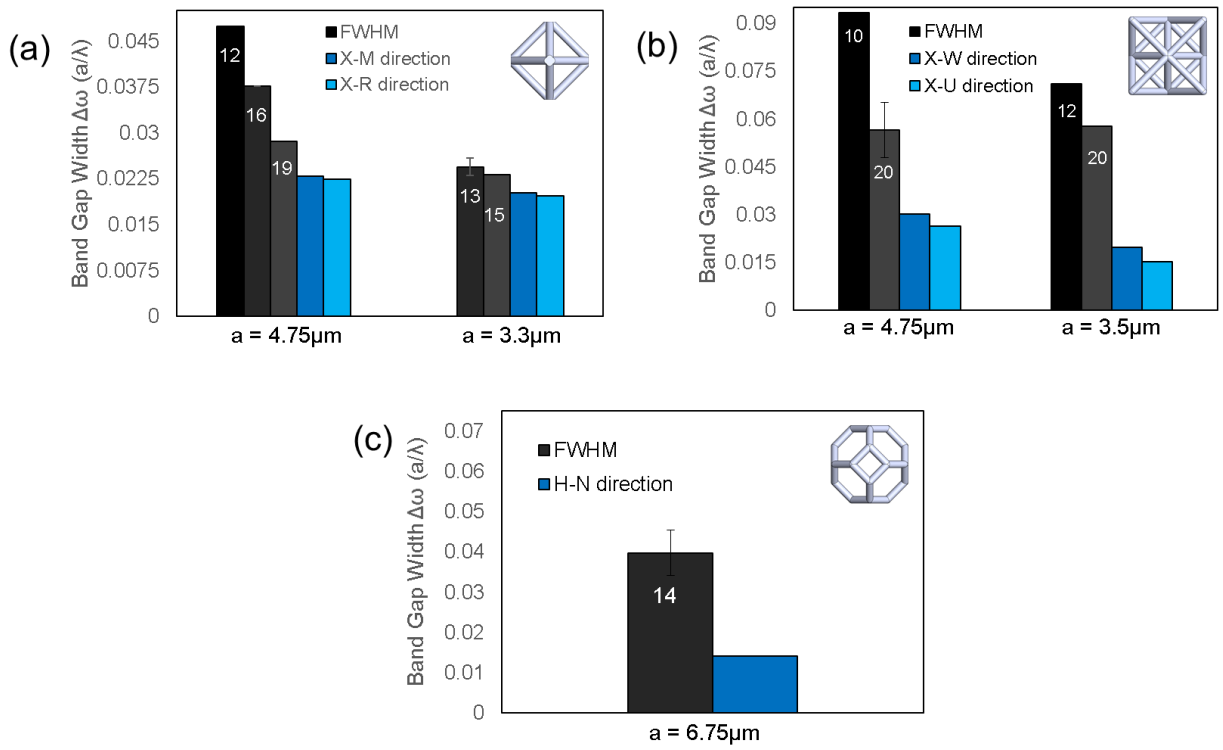

Figure 25. FWHM of experimental reflectivity peaks versus calculated bandgap width Δω for octahedron, octet, and tetrkaidecahedron PhCs of varying periodicity. (a) The FWHM of experimentally measured octahedron peaks is plotted (black and grey bars) versus the calculated bandgap width in both the X-M and X-R directions (blue bars). The number of z-layers for each measured octahedron PhC is presented on the corresponding data bar. (b) The FWHM of experimentally measured octet peaks is plotted (black and grey bars) versus the calculated bandgap width in both the X-W and X-U directions (blue bars). The number of z-layers for each measured octet PhC is presented on the corresponding data bar. (c) The FWHM of experimentally measured tetrakaidecahedron peaks is plotted (black bar) versus the calculated bandgap width in the H-N direction (blue bar). The number of z-layers is presented on the data bar.

In Figure 25 we compare the compare the FWHM values of our various architected PhCs and their varied periodicities to the bandgap width, Δω, calculated along each relevant Brillouin zone direction. It should be noted that data is excluded from lattices with substantial deformation, and FWHM values are distinguished on the basis of the number of z-layers each lattice possesses (the thickness in terms of number of unit cells). In Figure 25(a) we look at the FWHM versus bandwidth for octahedron lattices with a = 3.3μm and a = 4.75μm. We observe that, though minor, there is a difference in bandgap width between bandgaps in the X-M and X-R directions, and that, as expected, as we increase the number of layers in our lattice, we begin to approach the theoretical bandgap width. For octahedron samples of sufficient

conformity, we observe that the FWHM value begins to approach Δω when the number of layers divided by lattice period is approximately greater than or equal to 4.

In Figure 25(b) we look at the FWHM versus bandwidth for octet lattices with a = 3.5μm and a = 4.75μm. We again observe that, though minor, there is a difference in bandgap width between bandgaps in the X-W and X-U directions, and that, as expected, as we increase the number of layers in our lattice, we steadily get closer to the theoretical bandgap width. Nonetheless, we find that, even in the "extreme" case of lattices with 20 unit cells in the vertical dimension, we still do not reach the theoretical bandgap width. This is an interesting finding and one which cautions the use of TPL DLW in the fabrication of "infinite" PhCs – while we can, in theory, write taller PhCs (up to a limit of 300μm depending on the particular objective used), the time necessary for writing such a structure would be untenable. As it currently stands, layer-by-layer writing of a single 130μm x 130μm x 95μm lattice takes on the order of 8 hours, and increasing the lattice height would scale the write time linearly.

In Figure 25(c) we look at the FWHM versus bandwidth for tetrakaidecahedron lattices of 6.75μm periodicity. We only fabricated samples 14 unit cells in height, but observe that this is not enough to begin approaching the theoretical bandgap width in the H-N direction. For all lattice architectures and periodicities, additional PhCs of varying thickness must be fabricated and measured to get a more accurate representation of the number of layers necessary to reach the theoretical bandgap width.

3.6. Future Directions for Exploring the Photonic Properties of Polymer 3D Architected PhCs

In this chapter we performed a study on the optical properties of polymer 3D nanolattices with varied underlying cubic symmetries by means of reflectivity measurements and band structure calculations. By comparing experimental reflectivities to numerically derived bandgap positions for simple cubic octahedron, face centered cubic octet, and base centered cubic tetrakaidecahedron PhC, we were able to characterize the finite size effects present in the optical properties of our samples, and show how the periodicity uniquely effects the degree to which bandgap position changes depending on lattice architecture.

However, in future studies, FTIR measurements should be supplemented with angle resolved spectroscopy, such that reflectivity can be determined over precise increments in momentum space, allowing us to determine the exact stopband position versus wave-vector. Additionally, to understand the effect of periodicity on stopband position without interference from factors like fill fraction, lattices should be fabricated with specific beam dimensions that will keep volume fraction constant for varying unit cell size. And finally, a more rigorous study must be made of the relationship between layer number and bandgap width, which will require the fabrication and measurement of new octahedron, octet, and tetrakaidecahedron nanolattices.

Chapter 4: Exploring the Band Structure and Band Dispersion Phenomena of 3D Periodic Architectures – Demonstrating Negative Refraction in 3D Photonic Crystal Lattices

4.1. Introduction and Motivation

So far, studies of PhC's have been focused on the photonic band gap in which the photon density of states is zero. In this region the propagation of the radiation field is forbidden and thus a variety of novel phenomena, e.g., inhibition of spontaneous emission,[1] are possible. A PhC with a full photonic band gap is analogous to an insulator in which the Fermi energy lies in the energy gap. However, PhCs can display other properties based on their allowed bands, by which they can behave as novel "photonic conductors".

By exploiting various dispersion properties of PhCs, one may precisely control the wave propagation direction in the PhC for a given incident wave. Specifically designed 3D PhCs can act as alternatives to conventional defect PhC waveguides, since these structures do not require line defects for confinement, and yet can arbitrarily route light by exploiting engineered dispersion.

4.1.1. Photonic Crystal Bands and Equi-frequency contours (EFCs)

To understand the operation of dispersion-based PhCs, we first consider the band structure or dispersion diagrams for PhCs, which can be obtained numerically using various computational electromagnetic techniques like the plane wave expansion (PWE) method. The dispersion diagram gives the frequencies of propagating modes, or bands, versus the components of the corresponding wave vector, $\vec{k}$. The eigen-frequencies of the discretized bands are functions of wave vector components k_x, k_y, and k_z, allowing us to obtain equi-frequency surfaces (EFSs) of the dispersion diagram at a particular constant frequency. Taking a cross-section of the EFS by setting one of the wave vector components to zero gives us equi-frequency contours (EFCs).

The dispersion surface provides useful information for applications where unique refractive properties are necessary. Specifically, waves excited by a given k-vector will propagate with a group velocity, v_g, along the direction of the gradient of the dispersion surface or contour, $v_g = \nabla k(\omega)$, which is perpendicular to the EFC. By carefully choosing PhCs parameters and frequencies one can obtain square-shaped, star-

shaped, and circular EFCs. Square-shaped EFCs can lead to the phenomenon of self-collimation. Star-shaped EFCs allow for super-prism behavior. And circular EFCs can lead to negative refraction. The ability to shape the EFCs, and thereby engineer the dispersion properties of the PhC, opens a new paradigm for the design and function of PhC devices.

4.2. Negative Refraction and its Implications

Negative refraction is the property of light bending backwards at an interface. And while it is not observed in nature, this phenomenon is physically allowable. Negative refraction was first proposed by Veselago in 1968.[46] He theorized that if a material were to have simultaneously negative effective permittivity and permeability (a so called "left-handed" material), the energy flow in the material, as dictated by the Poynting vector, would be anti-parallel to the wave vector.[46] The implication of this property is that group velocity, $v_g = d\omega/dk$, would be negative, and a refracted wave propagating away from the interface of this material would travel on the negative side of the surface normal. Per Snell's law, a negative angle of refraction gives rise to a negative index of refraction[47]. In recent years it has been shown that artificially prepared metamaterials and photonic crystals can exhibit negative refraction. Such negative index materials (NIMs) can act as superlenses, focusing diverging light rays emanating from an object into two images, one inside the NIM slab, and one on the other side of the slab.

4.2.1. Negative Refraction in metamaterials

One means of achieving a negative index requires a material to simultaneously possess a negative dielectric permittivity ε, and a negative magnetic permeability μ, making it a left-handed material. In the late 1990s, Pendry proposed that electromagnetic resonances in artificially engineered materials made of periodic metal loops and wires could be tuned to values not accessible in natural materials.[48,49] By regulating these artificial metamaterials with unit cells much smaller than the working wavelength, the electric and magnetic resonances could be tailored individually and made to overlap at a desired frequency[50,51].

4.2.2. Negative Refraction in Photonic Crystals

The second type of negative index material is the dielectric photonic crystal (PhC) composed of purely right-handed materials[52]. Both metamaterials and PhCs are artificial periodic structures which can control photons, however, PhCs operate at a wavelength comparable to their lattice constant. While NR in metamaterials is governed by effective medium theory, which treats left-handed materials as uniform media to determine their properties[53], the underlying physical principles that allow NR in PhCs arise from the dispersion characteristics of wave propagation in the periodic medium.

In the case of photonic crystals, theory and experiments have largely focused on achieving negative refraction in two-dimensional periodic structures, which is necessary for the fabrication of superlenses, which are capable of subwavelength imaging[54,55]. True subwavelength imaging of three-dimensional (3D) objects however, requires a 3D PhC capable of negatively refracting light traveling in all three spatial planes, and it was not until 2002 that Luo, Johnson, and Joannopoulos (ref. [56]) proposed a lattice capable of negative refraction for all incident angles from air, now known as all-angle negative refraction (AANR)[56].

The structure proposed by Luo *et al*. consists of a body-centered cubic (BCC) lattice of air cubes embedded in a dielectric with $\varepsilon = 18$ (e.g. germanium in the near-infrared region)[56]. It is specified that for a conventional bcc unit cell with periodicity a, the sides of the air cube are parallel to the unit cell, and have an edge length of $0.75a$.[56] This PhC lattice yields a band structure that possesses a negative photonic-mass region (mathematically, a concave-downward shape) in the third band between the ΓH and ΓN directions, where AANR is observed and the effective refractive index of the PhC is $n_{eff} \approx -1$ (refer to Figure 1 in reference 56). The frequency range for AANR in this lattice spans from $0.375(2\pi c/a)$ to $0.407(2\pi c/a)$, where the equi-frequency contours of the third band are all-convex (circular) and larger than that of air (Figure 2 in reference 56). The lower boundary of this AANR region falls at the frequency where the band has an inflection point, and the upper boundary is at the frequency where the band intersects the light line (dispersion curve for air) along the ΓH direction.

Luo *et al*. proposed and theoretically investigated this 3D PhC capable of AANR, yet the only experimental demonstration of AANR in 3D has been shown by Lu *et al*., at microwave frequencies[57,58].

The lack of experiments demonstrating 3D negative refraction in the optical and infrared range is due, in large part, to the difficulties inherent in fabricating fully 3D lattices with features on the nano- and micrometer length scale. With the advent and refinement of two-photon lithography (TPL) direct laser writing (DLW), it is now possible to fabricate arbitrarily complex 3D structures with sub-micron features. TPL DLW allows for the printing of low index polymeric scaffolds, and this process, coupled with chemical vapor deposition (CVD) or sputtering, for the deposition of high index dielectric materials like germanium (Ge), provides a prospective route for the fabrication of 3D core-shell lattices capable of negative refraction. This process has not yet been explored for the creation of AANR lattices; in this chapter we present numerical calculations to identify the effect of parameters like beam diameter, which directly translates into volume fraction *f*, and the ratio of low index core (polymer or amorphous carbon) to high index (Ge) shell material, have on the resulting frequency range available for negative refraction.

4.3. Photonic Band Structure and Equi-frequency Contour Calculations

We use a plane wave expansion method (PWEM), as described previously, to calculate photonic band-structure and equi-frequency contours (EFCs) of 3D PhCs capable of AANR in the mid-infrared (7.7 μm – 8.62 μm) wavelength range using a bcc lattice analogous to the one proposed by Luo *et al*[56]. These simulations were performed using the commercial software package RSOFT BandSOLVE. Figure 26(a-c) shows such a representative lattice with cylindrical, rather than rectangular beams as used in Luo *et al.*[56], to better reflect the topology of structures fabricated using TPL DLW.

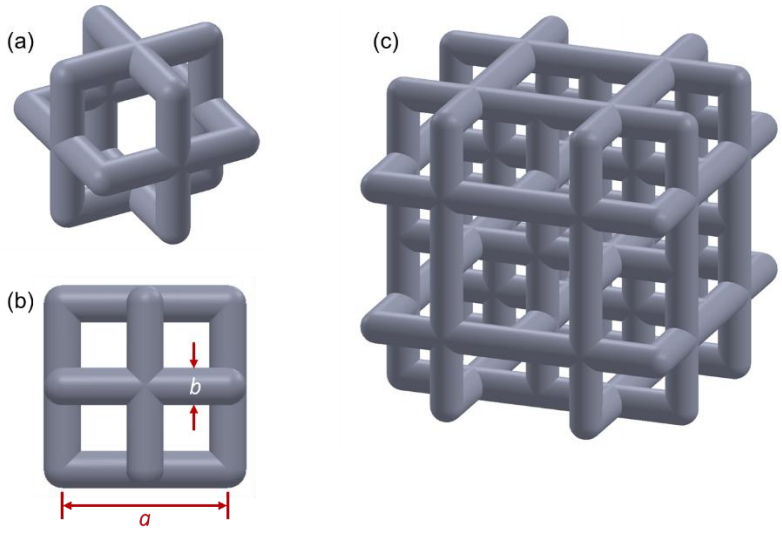

Figure 26. CAD schematic of the 3D bcc PhC lattice. (a) A view the PhC unit cell with cylindrical beams. (b) A single unit cell with representative dimensions for period, *a*, and beam diameter, *b*. (c) Schematic of the full, 3D lattice PhC.

BandSOLVE contains a "simulation parameters dialog" which controls the input and values of parameters required for a numerical simulation. Specifically, lattice vectors, supercell dimensions, number of steps per lattice dimension, and eigenvalue tolerance must be defined. Lattice vectors were expressed as,

$$\overrightarrow{\boldsymbol{a_1}} = \frac{\boldsymbol{a}}{\boldsymbol{2}}(\hat{\boldsymbol{x}} + \hat{\boldsymbol{y}} - \hat{\boldsymbol{z}}),\ \overrightarrow{\boldsymbol{a_2}} = \frac{\boldsymbol{a}}{\boldsymbol{2}}(-\hat{\boldsymbol{x}} + \hat{\boldsymbol{y}} + \hat{\boldsymbol{z}}),\ \overrightarrow{\boldsymbol{a_3}} = \frac{\boldsymbol{a}}{\boldsymbol{2}}(\hat{\boldsymbol{x}} - \hat{\boldsymbol{y}} + \hat{\boldsymbol{z}}) \tag{7}$$

and these are the typical real space vectors for a bcc lattice type. Supercell dimensions, in the context of BandSolve, are equal to a multiplication factor for the chosen lattice vectors. Since BandSolve assumes periodic boundary conditions in all three directions, we needed only to define a single unit cell, and set supercell dimensions to 1 in each direction. Finally, the number of steps in the domain refers to the numerical resolution of the lattice in each direction, which is directly related to the number of plane waves used in the expansion. For 3D or "hybrid" calculations of the type we perform, the number of plane waves used is twice the number of steps stated in the parameters section, as the simulation must account for two polarization states for each plane wave. A finer grid resolution increases the accuracy of the calculation at the expense of the convergence time. Through optimization studies, it was found that setting the number of steps to 64 in each direction was sufficient for both accuracy and simulation time. Finally, eigenvalue

tolerance, the parameter which controls the convergence tolerance for the PWE minimization algorithm, was set to 10^{-12}. Each of these parameters remained consistent over all simulations performed.

4.3.1. Exploring Varied Simulation Parameters: Fill Fraction

In the first case study we investigate the effect of beam diameter, or volume fraction *f*, on the average frequency and frequency range for observing AANR. In this analysis, lattice beams are comprised of a single uniform material with a dielectric constant $\varepsilon = 16.038$ (e.g., Ge in the mid-infrared around $\lambda = 8.0$ μm)[59]. The period of the bcc lattice is set to $a = 4$ μm, an easily fabricated unit cell size using TPL, and the beam diameter is varied between $b = 0.125a = 500$ nm, and $b = 0.5a = 2$μm. This is equivalent to varying the volume fraction of the lattice between $f = 0.07$ and 0.68.

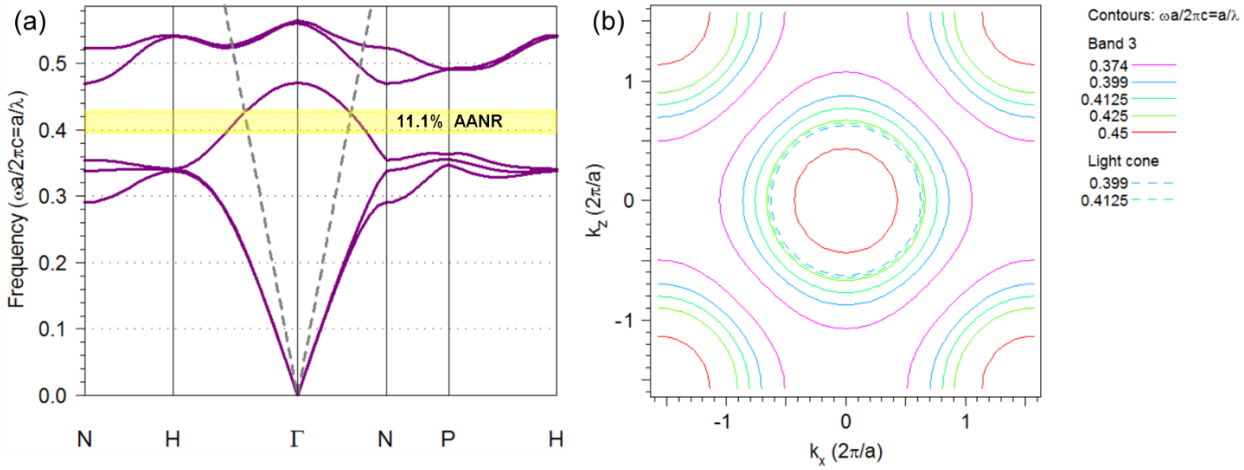

Figure 27. Representative band structure and equifrequency contours. (a) Representative band structure of the 3D PhC ($f = 0.23$). The yellow shaded area represents the frequency range where the PhC exhibits negative refraction for incoming radiation of all angles. The dashed grey lines are the light lines along Γ*H* and Γ*N*. (b) Slice of the equi-frequency surfaces on the $k_y = 0$ plane for band 3 shown in part *(a)*. The highest frequency circle is colored red and lies at the center. Subsequently lower frequencies have larger diameter contours. The dashed circles are equi-frequency contours for air, and are lower than their PhC contour counterparts at the same frequency.

By applying the plane wave expansion method to Maxwell's equations, we solved for eigenfrequencies at a given wave vector and obtained results qualitatively similar to those of Luo *et al* [56]. Figure 27(a) shows a representative band structure of a PhC with a beam diameter $b = 0.25a$ ($f = 0.23$). The dashed straight grey lines in Figure 2(a) are the light lines, or dispersion curves for air, along directions of high symmetry in the first Brillouin zone of a bcc crystal. Within the PhC, light propagates normal to its dispersion surface, which is the 3D k-space representation of the supported eigenmodes (bands). Taking a cross-section of a

dispersion surface yields an equi-frequency contour (EFC) that can be used to predict the direction of light propagation in the PhC. Figure 27(b) shows such a cross-section of the dispersion surface for band 3 along the $k_y = 0$ plane, generating EFCs. We observe that in the frequency range between $\omega = 0.380(2\pi c/a)$ to $0.425(2\pi c/a)$ EFCs are circular and larger than the corresponding EFCs of air. As the frequency increases, EFC radii shrink, indicating negative group velocity, and consequently negative effective refractive index in this range.

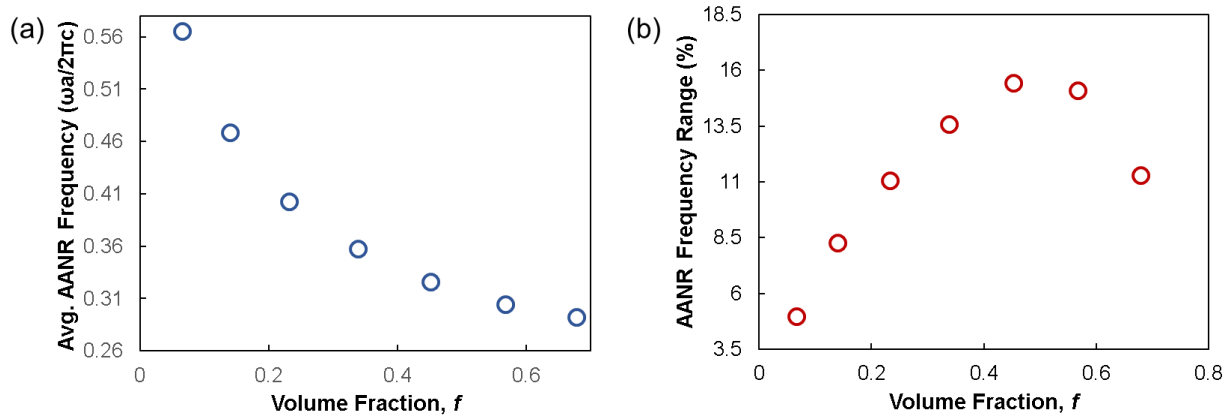

Figure 28. Average AANR Frequency and AANR Frequency range versus volume fraction. (a) Average frequency at which AANR is observed as a function of the volume fraction (beam diameter). (b) AANR frequency range, represented as a percentage difference, as a function of volume fraction.

Varying the volume fraction (f) by changing the beam diameter for a lattice with a set periodicity, we observe that the average frequency for AANR decreases with increasing volume fraction (Figure 28(a)). This is the result of bands compressing and shifting to lower frequencies when the volume fraction of high index material in a PhC increases[3]. Figure 28(b) shows the relative AANR frequency range as a function of volume fraction. Unlike the average AANR frequency, which decreases monotonically with increasing f, (Figure 24(a)), the AANR frequency range has a more complex dependence on the volume fraction, reaching a maximum of 15.4% for a beam diameter b =1.5 μm (f = 0.45). These calculations reveal that there exists an optimal volume fraction for maximizing the AANR frequency range. The aim of this study is to identify physically realizable lattice parameters for the fabrication of PhCs with appreciable AANR in the wavelength range between 7.7 μm – 8.62 μm; we choose to focus on lattices with b = 1.0 μm, or f = 0.23. For this volume fraction, the AANR frequency range is substantial, at 11.1%, and for a lattice period

of 4.0 μm, the average wavelength for observing AANR is centered around 9.9 μm (Table 1). Though this wavelength lies outside the measurement capabilities of our mid-IR spectroscopic setup (which utilizes a quantum cascade laser operating between 7.7 μm – 8.62 μm and will be discussed in greater detail subsequently), actual PhC fabrication efforts will involve using TPL DLW and sputter deposition to create polymer core, germanium shell lattices. The combined refractive index of the core-shell structure will be lower than that of pure Ge, and will push the AANR region to shorter wavelengths.

Table 1. Figures of merit derived from band structure and EFC calculations on PhC lattices of varied beam diameters with n_{beam} = 4.0047.

Beam Diameter (μm)	Volume Fraction, *f*	Absolute Frequency Range, Δω (2πc/a)	Average AANR Frequency (2πc/a)	AANR Frequency Range (%)	Average AANR Wavelength (μm)
0.5	0.0658	0.0283	0.5659	4.9934	7.0685
0.75	0.1394	0.0388	0.4689	8.2831	8.5303
1.0	0.2320	0.0445	0.4026	11.0587	9.9343
1.25	0.3381	0.0485	0.3573	13.5682	11.1937
1.5	0.4517	0.0503	0.3258	15.4339	12.2765
1.75	0.5670	0.0459	0.3044	15.0843	13.1414
2.0	0.6781	0.0330	0.2923	11.2908	13.6854

4.3.2. The Effect of Relative Index of Refraction

4.3.2.1. Polymer Core, Ge Shell PhCs

We also used PWEM to calculate band structure and EFCs to quantify the effect of modified dielectric constant on AANR frequency when core-shell structures are explored. For this analysis, lattice periodicity remains at a = 4 μm, the total beam diameter is set to $b = 0.25a$ = 1 μm (f = 0.23), and the relative ratio of low-index (n = 1.49) acrylate polymer core material[60], and high-index (n = 4.0047) Ge shell material[59] is varied by progressively increasing the core diameter and simultaneously shrinking the thickness of the shell to maintain the same total beam diameter. We varied the core diameter from $b_{core} = 0.1b$ = 100 nm, where shell thickness $t_{shell} = (b - b_{core})/2$ = 450 nm, to $b_{core} = 0.9b$ = 900 nm, with $t_{shell} = (b - b_{core})/2$ = 50 nm, and in so doing decreased the compound index of the lattice (see Table 2). For reference, compound refractive index (n_{beam}) is determined by calculating the ratio of polymer core material to germanium shell material

present in the cross-sectional area of a lattice beam. We observed a monotonic increase in the average frequency for AANR and a monotonic decrease in AANR frequency range with decreasing compound refractive index of lattice beams (Figure 29(a-b)). As this ratio increases, the combined index of the whole PhC decreases down to a threshold index below which AANR is no longer possible. Specifically, by simulating EFCs, we observe that below an index of n ~ 3.1, equivalent to a polymer core of b_{core} = 600 nm and germanium shell of t_{shell} = 200 nm in lattices of volume fraction f = 0.23, an AANR region does not exist. It appears that below this index the periodic modulation effect is weak, and the EFC changes its shape from circular to square-like. Figure 29(c) shows the band 3 EFCs for a lattice with b_{core} = 700 nm and t_{shell} = 150 nm, where n_{beam} = 2.77, and reveals that in the frequency region below the light line (which falls at $\omega = 0.528(2\pi c/a)$ for this lattice) the contours have a square-like shape. A circular EFC means that light can travel isotropically, and a square-like EFC, with its broad, flat regions, indicates that light can propagate without spreading or diffracting significantly, known as self-collimation. We found that lattices with a compound index < 3.1 do not display AANR, but their EFCs indicate that such lattices possess the unique property of self-collimation.

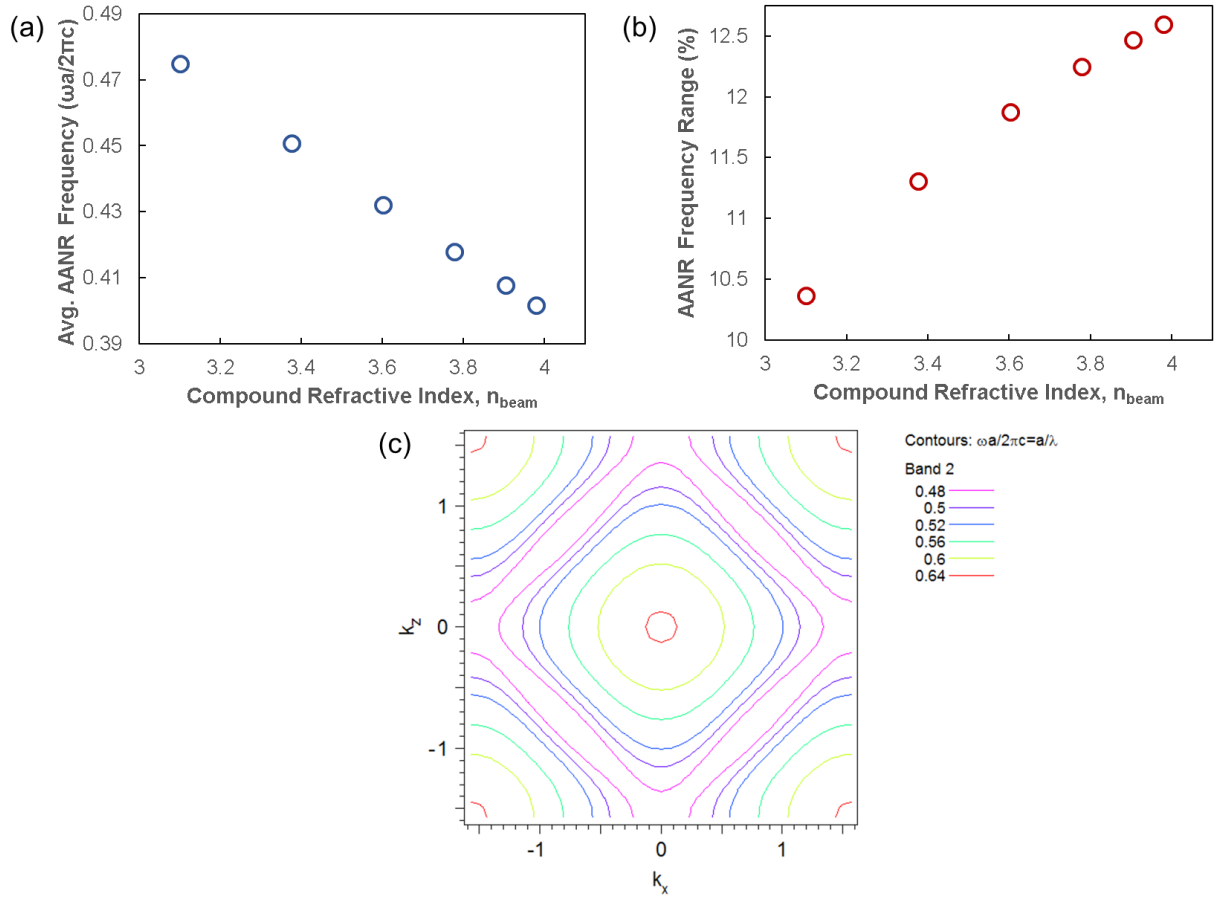

Figure 29. Average AANR Frequency, AANR Frequency range, and equi-frequency contours for polymer-germanium core-shell PhCs. (a) Average frequency at which AANR is observed in the PhC when the compound refractive index of the lattice is varied (polymer core to Ge shell ratio changes). (b) AANR frequency range, represented as a percentage difference, for PhCs with varying compound refractive index (polymer core to Ge shell ratio changes). (c) Slice of the equi-frequency surfaces on the $k_y = 0$ plane for a PhC lattice with b_{core} = 700 nm and t_{shell} = 150 nm (n_{beam} = 2.77).

Table 2. Figures of merit derived from band structure and EFC calculations on core-shell PhC lattices of varied polymer core diameter and Ge shell thickness.

Core beam diameter, b_{core} (μm)	Shell thickness, t_{shell} (μm)	Refractive Index, n_{beam}	Absolute Frequency Range, Δω (2πc/a)	Average AANR Frequency (2πc/a)	AANR Frequency Range (%)	Average AANR Wavelength (μm)
0.1	0.45	3.9796	0.0506	0.4017	12.5933	9.9574
0.2	0.40	3.9041	0.0508	0.4078	12.4654	9.8077
0.3	0.35	3.7784	0.0512	0.4179	12.2456	9.5715
0.4	0.30	3.6023	0.0513	0.4320	11.8763	9.2596
0.5	0.25	3.3760	0.0509	0.4507	11.3045	8.8752
0.6	0.20	3.0994	0.0492	0.4748	10.3671	8.4240

This series of simulations revealed that to preserve the circular shape of EFCs and to observe AANR between 7.7 μm – 8.62 μm using polymer-Ge core-shell lattices, the core diameter should be no greater than ~600 nm. This beam diameter is at a size scale below the resolution limit of TPL DLW capability (cylindrical beams are limited to a diameter of ~900 nm).

4.3.2.2. Carbon Core, Ge Shell PhCs

As an alternative to writing lattices with a polymeric core, recent literature suggests that if a polymer lattice is pyrolyzed under specific temperature and atmospheric conditions, amorphous carbon (a-C) lattices with significantly smaller dimensions will be formed[61]. Amorphous carbon is lossy in the mid-infrared (the extinction coefficient $\kappa = 1.8818$ at $\lambda = 8.0$ μm) but has a higher refractive index of $n = 2.9622$ at $\lambda = 8.0$ μm compared to the $n = 1.49$ of the acrylate polymer[60,62]. To quantify the effect on average AANR frequency and frequency range when core-shell lattices are composed of a-C cores and Ge shells, we repeated the previous series of band structure and EFC simulations, replacing only the core polymer material parameters with those of a-C (Table 3). We find that as is the case in the polymer core-shell lattices, increasing the ratio of a-C to Ge material in the lattice decreases the overall combined index of the structure. We observe a monotonic increase in the average frequency for AANR and a monotonic decrease in AANR frequency range with decreasing compound refractive index of lattice beams (Figure 30(a-b)). Even at the extreme of b_{core} = 900 nm and t_{shell} = 50 nm, an apparent AANR frequency range exists since this lattice configuration has $n_{beam} > 3.1$. This suggests that fabricating a-C core, Ge shell lattices with core diameters around 900 nm would enable AANR observation in the ideal 7.7-8.62 μm range.

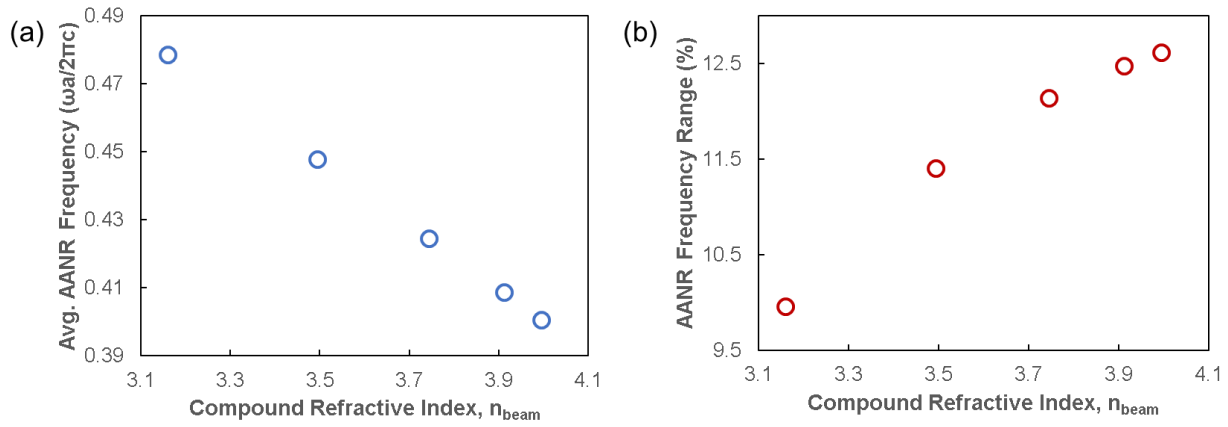

Figure 30. Average AANR Frequency and AANR Frequency range for amorphous carbon-germanium core-shell PhCs. (a) Average frequency at which AANR is observed in the PhC when the compound refractive index of the lattice is varied (amorphous carbon core to Ge shell ratio changes). (b) AANR frequency range, represented as a percentage difference, for PhCs with varying compound refractive index (amorphous carbon core to Ge shell ratio changes).

Table 3. Figures of merit derived from band structure and EFC calculations on core-shell PhC lattices of varied amorphous carbon core diameter and Ge shell thickness.

Core beam diameter, b_{core} (μm)	Shell thickness, t_{shell} (μm)	Refractive Index, n_{beam}	Absolute Frequency Range, Δω (2πc/a)	Average AANR Frequency (2πc/a)	AANR Frequency Range (%)	Average AANR Wavelength (μm)
0.1	0.45	3.9943	0.0506	0.4007	12.6164	9.9826
0.3	0.35	3.9109	0.0510	0.4088	12.4802	9.7839
0.5	0.25	3.7441	0.0515	0.4246	12.1408	9.4216
0.7	0.15	3.4939	0.0511	0.4479	11.4088	8.9307
0.9	0.05	3.1603	0.0477	0.4787	9.9560	8.3557

4.3.2.3. Polymer Core, Si Shell PhCs

Another relatively high index dielectric material commonly utilized in PhC fabrication is silicon (n = 3.4189 at λ = 8.0 μm)[63]. Silicon deposition methods are more ubiquitous and better optimized compared to Ge deposition, so we also chose to study the effect on average AANR frequency and frequency range when core-shell lattices are composed of polymer cores and Si shells. To do this, we repeated the previous series of band structure and EFC simulations, replacing only the germanium shell parameters with those of silicon (Table 4). Similar to our previous parameter sweeps, we observed a monotonic increase in the average frequency for AANR and a monotonic decrease in AANR frequency range with decreasing compound

refractive index of lattice beams (Figure 31(a-b)). As the diameter size of the polymer core increases and Si shell thickness decreases, the combined index of the whole PhC lowers and reaches a threshold index below which AANR is no longer possible. Specifically, by simulating EFCs, we again observe that below an index of n ~ 3.1, approximately equal to a polymer core of b_{core} = 400 nm and germanium shell of t_{shell} = 300 nm in lattices of volume fraction f = 0.23, an AANR region does not exist. As was the case with polymer-Ge core-shell lattices, below an index of 3.1, the periodic modulation effect is too weak, and EFCs change shape from circular to square-like. Figure 31(c) shows the band 3 EFCs for a lattice with b_{core} = 500 nm and t_{shell} = 250 nm, where n_{beam} = 2.94, showing that in the frequency region below the light line (which falls at $\omega = 0.520(2\pi c/a)$ for this lattice) the contours have a square-like shape. Square-like EFCs imply that these lattices are capable of self-collimation but not do not display AANR, when the compound index of the PhC beams are below 3.1, irrespective of the materials comprising the structure (Si versus Ge).

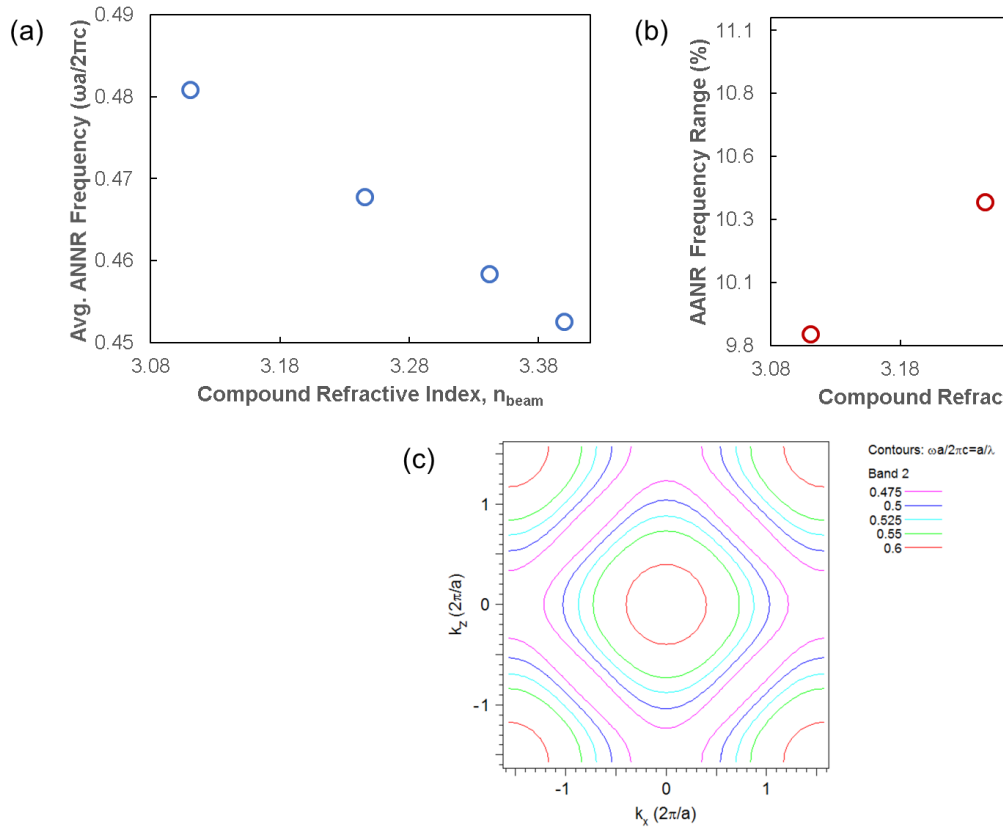

Figure 31. Average AANR Frequency, AANR Frequency range, and equi-frequency contours for polymer-silicon core-shell PhCs. (a) Average frequency at which AANR is observed in the PhC when the compound refractive index of the lattice is varied (polymer core to Si shell ratio changes). (b) AANR frequency range, represented as a

percentage difference, for PhCs with varying compound refractive index (polymer core to Si shell ratio changes). (c) Slice of the equi-frequency surfaces on the $k_y = 0$ plane for a PhC lattice with b_{core} = 500 nm and t_{shell} = 250 nm (n_{beam} = 2.94).

Table 4. Figures of merit derived from band structure and EFC calculations on core-shell PhC lattices of varied polymer core diameter and Si shell thickness.

Core beam diameter, b_{core} (μm)	Shell thickness, t_{shell} (μm)	Refractive Index, n_{beam}	Absolute Frequency Range, Δω (2πc/a)	Average AANR Frequency (2πc/a)	AANR Frequency Range (%)	Average AANR Wavelength (μm)
0.1	0.45	3.3996	0.0494	0.4526	10.9036	8.8376
0.2	0.40	3.3417	0.0491	0.4584	10.7066	8.7258
0.3	0.35	3.2453	0.0485	0.4678	10.3692	8.5498
0.4	0.30	3.1103	0.0474	0.4809	9.8474	8.3182

Because AANR with polymer-Si core-shell structures necessitates a circular core diameter on the order of 400nm, which is too small to achieve reliably with TPL DLW, we instead decided to pursue polymer-Ge core-shell designs.

4.3.3. The Effect of Beam Ellipticity

By performing the series of parameter sweeps listed above, we identified that a volume fraction of f = 0.23, which translates to a circular beam diameter of 1.0 μm for a lattice with 4.0 μm periodicity, is appropriate for the fabrication of low index core, high index shell lattice structures with AANR in the mid-infrared (7.7-8.62 μm range). Specifically, we can aim to fabricate lattices with a 500 nm diameter polymer core, and 250nm germanium shell, which should display AANR between 8.4 μm - 9.41 μm. While these parameters provide useful guidelines for fabricating the desired core-shell nanolattice PhCs, it is not realistically possible to fabricate beams with perfectly circular cross-sections, as the volumetric pixel, or voxel, that is the building block of the TPL DLW process is inherently elliptically shaped. While specialized writing schemes can be employed to generate beams that are largely circular in cross-section (see ref. [39] for more details), fabricated beams will almost certainly possess some degree of elliptical shape. To quantify the effect on average AANR frequency and frequency range when the cross-section of core-shell beams becomes increasingly elliptical, we again calculated band structure and EFCs, this time varying the

parameter of ellipticity, ξ, while keeping cross-sectional area of beams constant (both full beam cross-sectional area and respective core and shell cross-sectional areas are kept constant) for a lattice with a polymer core of b_{core} = 500 nm and germanium shell of t_{shell} = 250 nm.

Ellipticity is a measure of the compression of a circle along a diameter to form an ellipse, and can be defined as $\xi = \frac{a-b}{a}$, where a is the dimension of the semi-major axis of the total beam, and b is the dimension of the semi-minor axis of the beam. We varied the semi-major axis from a = 0.5 μm to $a = 0.83\overline{3}$ μm, and the semi-minor axis, which was treated as a function of a, varied from $b = 0.5^2/a$ = 0.5 μm to 0.3 μm. In this manner, beam cross-sectional area was kept constant at 0.785 μm^2, while ellipticity varied from ξ = 0, for a circular cross-section, to a maximum of ξ = 0.64 (Table 5).

Table 5. Figures of merit derived from band structure and EFC calculations on core-shell PhC lattices with beams of varying ellipticity and constant cross-sectional area.

Semi-major beam axis, a (μm)	Semi-minor beam axis, b (μm)	Ellipticity, $\xi\left(\frac{a-b}{a}\right)$	Absolute Frequency Range, Δω (2πc/a)	Average AANR Frequency (2πc/a)	AANR Frequency Range (%)	Average AANR Wavelength (μm)
0.5	0.5	0	0.0509	0.4507	11.3048	8.8753
0.5556	0.45	0.19	0.0494	0.4531	10.9054	8.8286
0.625	0.4	0.36	0.0479	0.4567	10.4933	8.7586
0.7143	0.35	0.51	0.0461	0.4629	9.9654	8.6415
0.8333	0.3	0.64	0.0446	0.4712	9.4696	8.4893

As the beam ellipticity increases, we observe a monotonic increase in the average frequency for AANR, and a monotonic decrease in AANR frequency range (Figure 32(a-b)). This is the result of bands compressing, and band 3 specifically shifting to higher frequencies as beams become more elliptical in shape. Figure 32(c-d) shows the actual band structure in the Γ-N direction for varying ξ. While the relative shape or concavity of band 3 does not change with ξ, we witness a decrease in band separation between bands 3 and 4, as well as a migration of band 3 to higher frequencies with increasing ellipticity.

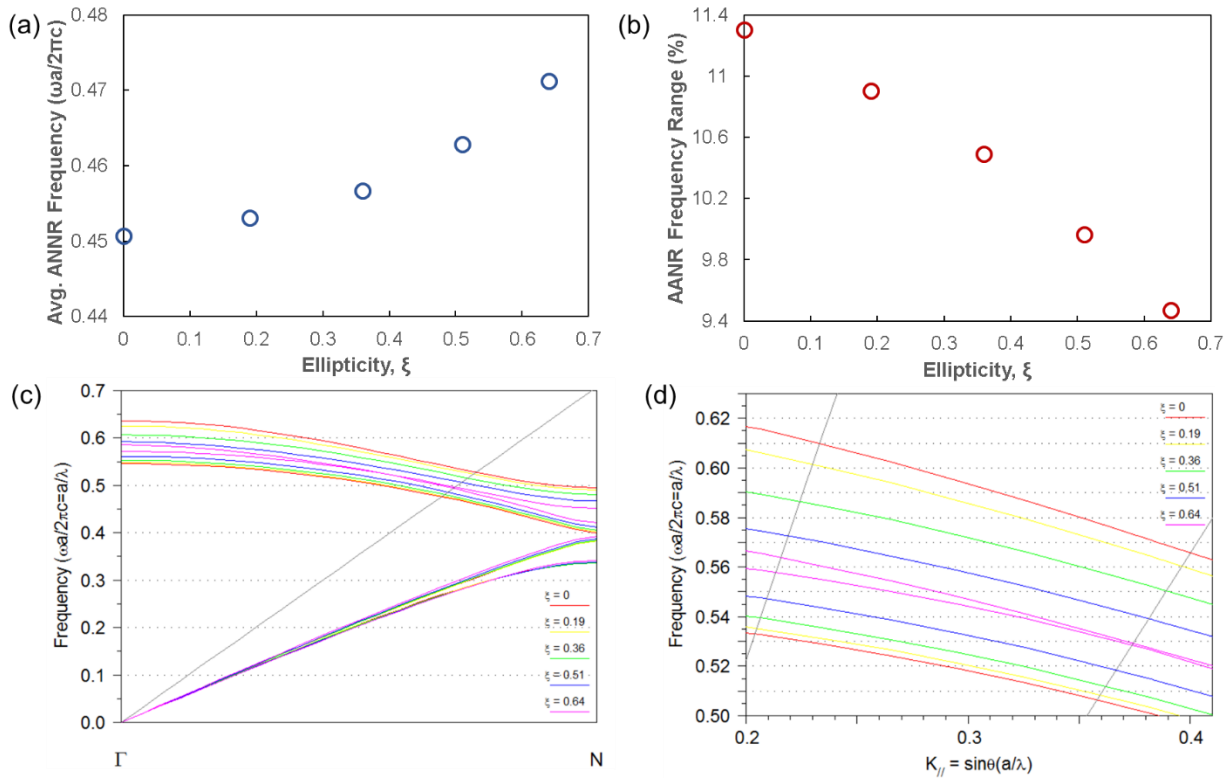

Figure 32. Average AANR Frequency, AANR Frequency range, and evolution of band structure for polymer-germanium core-shell PhCs with beams of varying ellipticity. (a) Average frequency at which AANR is observed in the PhC when beam ellipticity is varied (ratio of lattice beam semi-major and semi-minor axes changes). (b) AANR frequency range, represented as a percentage difference, for PhCs with varying beam ellipticity. (c) Band structure along the Γ*N* direction for the 3D core-shell PhC with varying beam ellipticity. The grey diagonal line is the light line (90° relative to the surface normal). (d) An enlarged subset of the band structure presented in *(c)*. The grey diagonal lines denote the angular span between 22.5° and 45°.

4.3.4. The Effect of Shell Offset Relative to Core Position

The process of creating core-shell lattice structures will involve deposition of high-index germanium onto low index polymer scaffolds. Between sputtering and chemical vapor deposition methods, neither process will likely yield an even, isotropic Ge coating. If Ge deposition is conformal but anisotropic, we can approximate beam cross-sections as "egg-yolks," where the Ge shell position is offset from the center position of the polymer core, as depicted in Figure 33(a). We study the effect of Ge shell offset on average AANR frequency and frequency range by simulating 500nm polymer core, 250nm Ge shell lattices and displacing the center position of the Ge shell relative to the polymer core center from 0 to 250nm in one dimension, the X-direction, two dimensions, the X and Z-directions (Ge shell is offset from the polymer core center by 0 to 250nm in both the X and Z directions), and in all three dimensions, the X-Y-Z-directions

(Figure 33(a)). We perform band structure and EFC simulations for all three offset varieties, and report the figures of merit in Table 6.

Table 6. Figures of merit derived from band structure and EFC calculations on polymer-Ge core-shell PhC lattices with Ge shell offset from the center core position in the X-direction, XZ-directions, and XYZ-directions.

Offset Type	Offset Value (μm)	Absolute Frequency Range, Δω (2πc/a)	Average AANR Frequency (2πc/a)	AANR Frequency Range (%)	Average AANR Wavelength (μm)
X-offset	0	0.0509	0.4507	11.3045	8.8752
	0.05	0.0515	0.4493	11.4605	8.9037
	0.1	0.0521	0.4471	11.6452	8.9471
	0.15	0.0526	0.4445	11.8365	8.9995
	0.2	0.0531	0.4417	12.0104	9.0556
	0.25	0.0533	0.4392	12.1378	9.1075
XZ-offset	0	0.0509	0.4507	11.3045	8.8752
	0.05	0.0510	0.4495	11.3466	8.8990
	0.1	0.0507	0.4475	11.3212	8.9388
	0.15	0.0500	0.4451	11.2231	8.9865
	0.2	0.0490	0.4425	11.0718	9.0392
	0.25	0.0479	0.4394	10.8989	9.1030
XYZ-offset	0	0.0509	0.4507	11.3045	8.8752
	0.05	0.0503	0.4492	11.2058	8.9042
	0.1	0.0486	0.4473	10.8718	8.9433
	0.15	0.0461	0.4451	10.3610	8.9864
	0.2	0.0435	0.4422	9.8432	9.0454
	0.25	0.0425	0.4359	9.7517	9.1769

We observe that, as the degree of offset increases in all three tests, average AANR frequency monotonically decreases, and the value of average AANR frequency does not vary significantly between samples offset in X, XZ, and XYZ (Figure 33(b)). This is because in general, offsetting the Ge shell from the center of the polymer core shifts the position of AANR relevant band 3 to smaller frequencies. In comparison, the degree of offset has a more complex effect on AANR frequency range (Figure 33(c)). Increasing the degree of X-offset appears to increase AANR frequency range, while increasing XZ and

XYZ-offset lowers the AANR frequency range. These trends are the result of the offset parameter subtly changing the shape or curvature of band 3 depending on the type of offset. While an offset of the Ge shell in X will maximally change the average AANR wavelength by 2.6%, and an offset in XYZ will maximally alter average AANR wavelength by 3.4%, these percentages translate to a change in AANR position of hundreds of nanometers, which can be significant when dealing with a narrow characterization region.

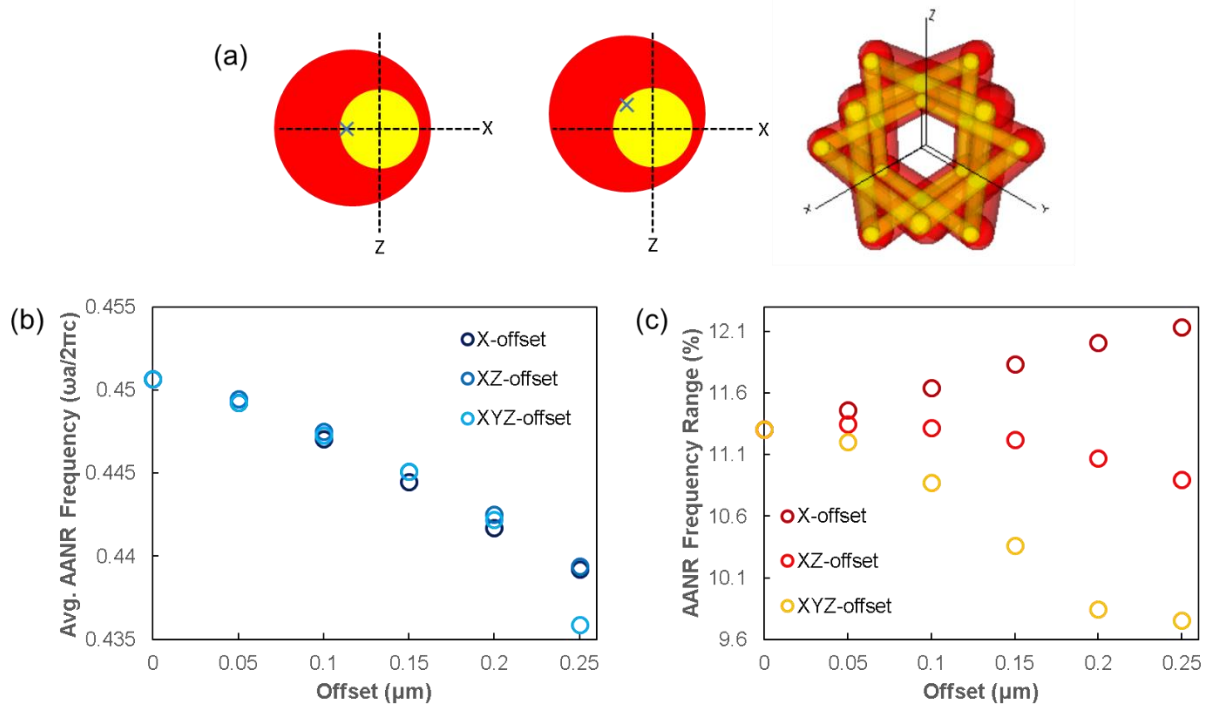

Figure 33. Examples of Ge-shell offset from the polymer-core center position in the X, XZ, and XYZ dimensions, and the effects of shell offset on average AANR Frequency and AANR Frequency range. (a) Schematics depicting the cross-section of a core-shell beam when the Ge-shell of offset from the center position of the polymer in the X-direction, XZ-directions, and XYZ-directions. Note that the blue cross represents the new center position of the full beam following shell offset. (b) Average frequency at which AANR is observed in the PhC when shell-offset position is varied in 1, 2, and 3 dimensions. (c) AANR frequency range, represented as a percentage difference, for PhCs with varying shell-offset in X, XZ, and XYZ.

4.3.5. The AANR Region Versus Frequency Regions Accessible for Experimental Observation of Negative Refraction

In all of the previous discussed simulations, we present figures and data relevant to the frequency region for observing all-angle negative refraction (AANR). The data presented was derived by looking at the properties band 3, which possesses a concave-down shape indicative of a negative "photonic-mass"[54,56], along the ΓN (101) direction. The AANR region is found between the point where the band intersects the

light line, and the point where band curvature changes. In this frequency region, EFCs will be all-convex and larger than that of air, and the effective refractive index may be regarded as $n_{eff} \approx -1$.[54] In the frequency region above the light line, where band shape is still concave-down, group velocity continues to be negative, but EFCs will no longer be larger than air. A consequence of this is that effective refractive index will still be negative, but will be between $-1 < n_{eff} < 0$, and negative refraction will now be angle dependent. The optical experimental characterization tools we have access to like FTIR and angle resolved spectroscopy both rely on the coupling of external radiation to PhC leaky modes, which are modes or bands, above the light line. Consequently, we will not be able to access or observe the PhC AANR region experimentally, but can instead couple into band 3 above the light line, where effective index should still be negative, but angle-dependent.

4.4. Core-Shell Photonic Crystal Fabrication

4.4.1. TPL DLW process

As described in detail in prior sections, nanolattices were first fabricated out of the acrylate-based "IP-Dip" photosensitive monomer, using a direct laser writing two-photon lithography (DLW TPL) system developed by Nanoscribe GmbH. For this DLW TPL process, the 3D periodic cube-like bcc architecture is created using MATLAB and the computer aided design (CAD) program SolidWorks, and lattice beams are defined in slices, for writing in a layer-by-layer fashion.[39] The layer-by-layer write necessitates that the full architecture be described as a series of x-y planes, defined at evenly spaced intervals along the z-axis (see ref. [39] for additional detail), and allows for the generation of beams possessing nearly circular cross-sections (as compared to the octahedron lattices described in Chapter 2 which had elliptical beams).

The design is then imported as a set of points describing the full 3D architecture to NanoWrite, proprietary software which interfaces with the Nanoscribe TPL DLW instrument to write the structure. To allow for subsequent optical characterization with an infrared laser of ~75-100μm spot size, lattices were designed to be 33 x 23 x 18 unit cells in x-y-z extent, resulting in structures with dimensions of approximately 130μm x 130μm x 100μm.

Nanolattice PhC samples were prepared by drop-casting the negative-tone photoresist “IP-Dip” (Nanoscribe GmbH) on a 500μm thick double sided polished silicon chip, to allow for transmission measurements through the sample and substrate.

After exposing the photoresist and generating the 3D polymer scaffold, structures were developed for 30 minutes in propylene glycol mono-methyl ether acetate (PGMEA) followed by a 5-minute rinse in isopropyl alcohol. To prevent lattice collapse or excessive shrinkage due to capillary forces during the drying stage, lattices were dried via a critical point drying method using a TousimisAutosamdri-815B, Series B critical point dryer.

4.4.2. Discussion of Surface Symmetry Effects and Lattice Orientation

It should be noted that fabricated lattices are constructed such that the original unit cell design, presented in Figure 26 and Figure 34(a), is rotated by 45° around the y-axis, so that the crystal surface is along the (101) direction.

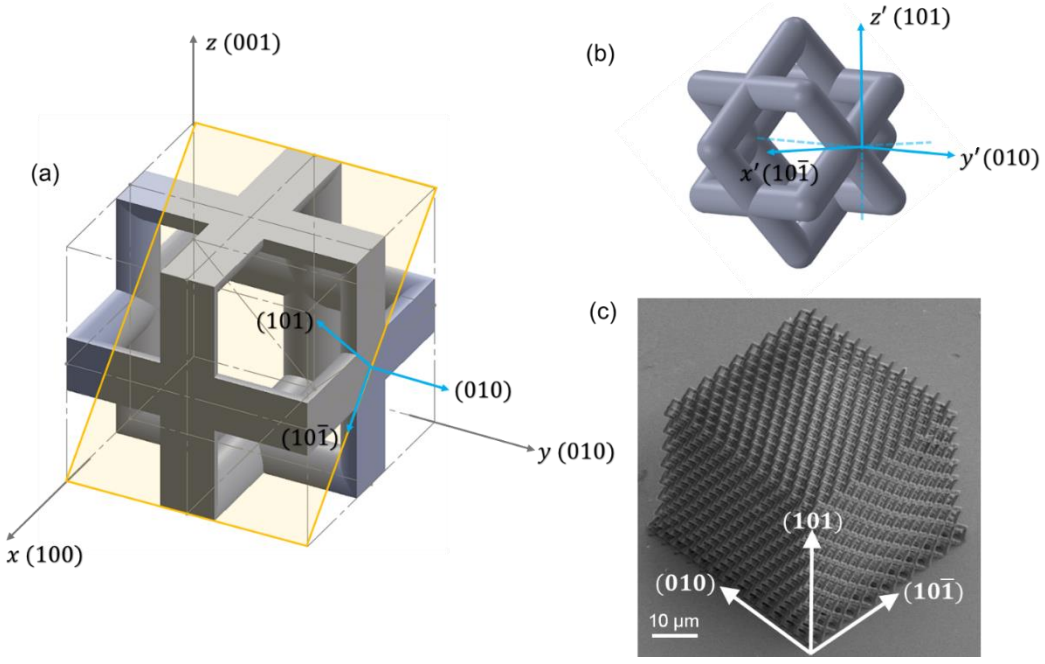

Figure 34. Surface symmetry and orientation of the bcc PhC lattice. (a) The original bcc cube-like PhC unit cell with (001) surface orientation and relevant coordinates and symmetry directions. (b) The proposed rotated bcc cube-like PhC unit cell with (101) surface orientation. (c) A TPL DLW fabricated polymer PhC lattice with (101) surface orientation.

To justify this design, we are reminded that the phenomenon of effective negative index in the bcc PhC lattice is present in a frequency range where only a single band, band 3 specifically, resides. In the context of group theory, this band, or mode, is singly degenerate, and the degeneracy is equivalent to the dimension of its irreducible representation, in this case, 1.[64] In order to observe negative refraction, it is necessary for incident light to couple into the mode, and this will only occur if the photonic crystal mode and incident light wave vector belong to the same irreducible representations of their defining symmetry group. In particular, if the bcc PhC is oriented such that the surface is along the (001) direction, this translates to moving along the Γ-H high symmetry direction which belongs to the C_{4v} symmetry group.[65] Along the (001) direction normal incidence radiation will have two degenerate polarizations, and they are partners of the basis function for the irreducible representation E.[56,64] Only photonic bands that are themselves doubly degenerate can interact with this incident light, and consequently for this direction, no coupling, and hence no negative refraction, will be observed.

If we instead consider the (101) direction (which corresponds to the PhC orientation and surface symmetry depicted in Figure 34(b-c)), this refers to moving along the Γ-N high symmetry direction and belongs to the C_{2v} symmetry group.[65] For this high symmetry direction the two polarizations are no longer degenerate, and the $(10\bar{1})$ polarization specifically can couple strongly to the photonic crystal mode.[56] Conversely, for the other polarization along (010), coupling will be nonexistent at normal incidence, and extremely low at nonzero incident angles.[56]

Through group symmetry arguments, it is clear that the negative refraction phenomena will be strongly dependent on PhC orientation and incident light polarization. Negative index behavior in our bcc PhC will be most obvious for a lattice with (101) surface termination and incident light of $(10\bar{1})$ polarization. We therefore chose to fabricate our bcc PhC with the (101) orientation (Figure 16(c)) and keep in mind these restrictions on coupling in our experimental designs.

4.4.3. O_2 plasma Etching

Following fabrication with TPL DLW, lattices possess circular beams with dimensions on the order of ~850-900nm. Using the previously ascertained simulation results as a guide, we know it is necessary to isotropically reduce the beam diameter to <600nm, and more ideally to ~500nm. Lattices were dry etched with O_2 plasma using a Pie Scientific Tergeo Plus Plasma Cleaner in remote plasma cleaning mode. Typical etching conditions included an oxygen flow rate of 15 sccm and 50 W power. In downstream or remote plasma cleaning mode, oxygen plasma is generated outside sample chamber, which limits sample immersion in energetic plasma and reduces the extent to which lattices are sputtered by energetic ions. Through this process, only gentle, isotropic chemical etching should take place on the lattice beam surface by neutral radicals.

Using the above parameters, we observed an average beam etch rate of 10 nm/min. However, even using these mild etch conditions at high pressure, etching was anisotropic, resulting in the formation of elliptical beams as well as regions of over-etching which could be approximated as beam tapering. Figure 35 is a representative SEM image of the $(10\bar{1})$ lattice face at a 45° tilt after 45 min of etching. It is evident that etch rate is anisotropic with the transverse beam dimension etching faster and producing smaller features relative to the axial beam dimension. On average, O_2 plasma etching using the parameters listed above yields elliptical beams with a short axis of 454 ± 27 nm, and long axis of 647 ± 49 nm. We also observe regions of over-etching or pitting in the axial dimension. The over-etched beam region is measured to be 247 ± 40 nm.

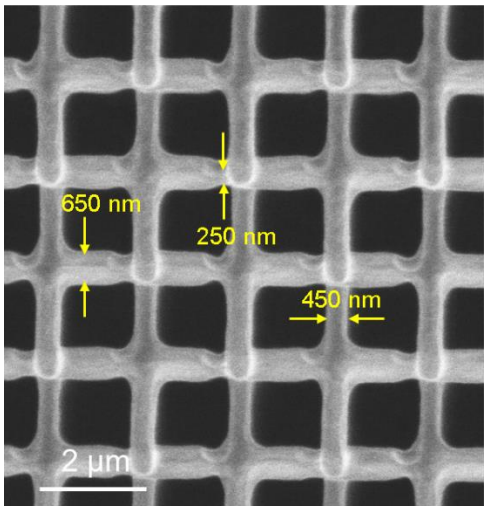

Figure 35. Representative scanning electron microscopy (SEM) image of the (10$\bar{1}$) lattice face of a bcc PhC lattice after 45 min of oxygen-plasma etching. The image was taken at a 45° tilt and approximate beam dimensions are labeled.

4.4.4. Germanium Deposition via Sputtering

The next step in the fabrication process for low-index core, high-index shell bcc PhC lattices is the deposition of germanium onto the etched polymer scaffold. Of the deposition tools available to us, sputtering was the only option which could yield a nominally conformal, isotropic deposition of Ge on our 3D architected structures.

We deposit germanium on to etched polymer lattices by sputtering with a germanium target (Kurt Lesker, Inc.) using a RF power supply at 100 W, under 5 mTorr and 20 sccm argon in a magnetron sputter deposition system (ATC Orion sputtering system, AJA International, Inc.). Base pressure is set to $>4\times10^{-6}$ Torr, and target ramp up and ramp down times are precisely controlled at 10 W/min to prevent the target cracking. Prior to deposition on the sample, the target undergoes a 2-minute burn-in process to remove contaminates and surface oxide.

To improve the conformality of Ge deposition and ensure material penetration through the lattice, sputtering was performed on samples mounted at 90° on an SEM stub on the rotating chuck. With this configuration, the side faces of the lattice, namely the (010) and (10$\bar{1}$) surfaces, were directed towards the target, rather than the lattice top. With the above sputtering parameters, we observed a deposition rate of 0.375nm/min on the 3D lattice structure. Each of the four sample side faces were directed towards the target

and sputtered in increments of 2hrs and 46min, resulting in the deposition of approximately 250nm thick Ge shells on the polymer lattice beams.

4.4.5. FIB cross-section characterization of Ge deposition on 3D structures

Focused ion beam (FIB) milling was used to access the conformality and thickness of germanium deposited onto polymer lattices. To be as minimally destructive towards the sample, only the edges of the core-shell PhC were FIB milled, revealing beam cross-sections for imaging and measurement with scanning electron microscopy (Figure 36).

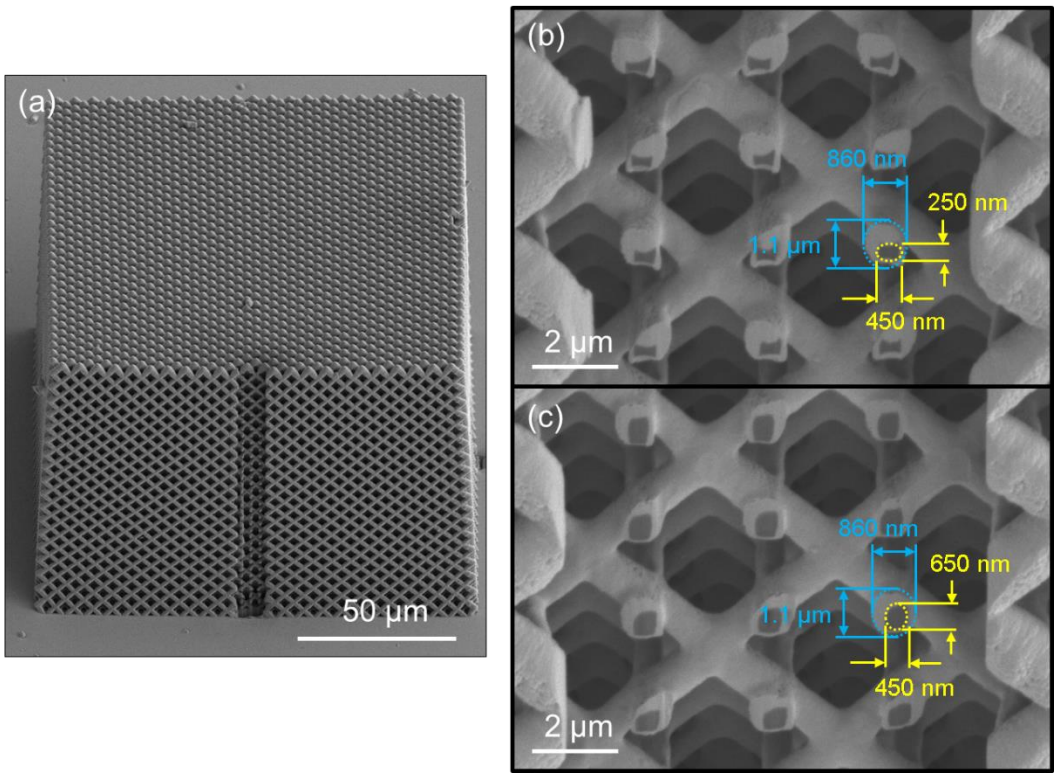

Figure 36. Scanning electron microscope images of a polymer-germanium core-shell PhC. (a) SEM image of the full core-shell lattice at 52° tilt with FIBed cross-section. (b) Enlarged section of the PhC (010) face following a FIB cut of approximately 1µm depth. (c) Same enlarged section shown in part (b), FIB cut 500nm further into the PhC lattice.

Figure 36(a) shows how we create a cleaning cross-section FIB cut into the center of the (010) face of our core-shell PhC. Such cuts are approximately 10 µm wide and span the height of the lattice, so that deposition can be assessed through all z-layers. We also examine Ge deposition and beam dimensions as a function of depth, doing so by FIB milling through the lattice iteratively. Through cross-sectioning and imaging, we measure an average lattice period of 3.8 µm, likely due to structure shrinkage in the TPL DLW

process. In Figure 18(b) we cut approximately 1 μm into the PhC edge and observe that (1) while Ge fully coats the polymer beams, it does not deposit in an isotropic manner, and a ~200nm offset in Ge shell position relative to polymer core position is evident, (2) beam cross-sections are approximately elliptical with the long axis of the full beam measuring 1061±55 nm and the short axis measuring 857±62 nm, and (3) over-etching of the polymer core is apparent at this cleaning cross-section depth, and can also be approximated as elliptical with a short axis of 247±40 nm and long axis of 447±31 nm. In Figure 36(c) we cut approximately 500 nm further into the PhC edge and observe that (1) the offset in Ge shell position relative to polymer core position persists through the length of the beam, (2) the dimensions of the full beam do not vary significantly, remaining elliptical with approximate dimensions of 1.1μm and 880nm, and (3) the polymer core is also elliptical with measured dimensions of approximately 650nm and 450nm.

FIB cross-sectioning reveals that the Ge shell on our lattices is conformal but not uniform, and if we take an average of the polymer core dimensions in both the over-etched and regularly etched regions and compare them to the full core-shell beam dimensions, then we have an average Ge shell thickness of 255 nm, which should be sufficient for the observation of negative refractive behavior.

4.5. Optical Characterization of Core-Shell Photonic Crystal Lattices

In order to observe the unique dispersion phenomena of our bcc core-shell PhCs, we must probe these structures with mid-IR light. One method for establishing whether our fabricated periodic structures possess a negative effective index of refraction is by experimentally mapping the photonic band structure. As discussed previously, band shape will determine the shape of our equi-frequency contours and direction of the group velocity vector inside the PhC, which will give us the propagation direction of a refracted beam. We can then apply Snell's law and calculate an effective index of refraction for this 3D periodic architecture at a given frequency.

4.5.1. Fourier Transform Infrared Spectroscopy

We first characterize our core-shell PhC sample using Fourier Transform Infrared (FTIR) microspectroscopy in reflectance mode. We employ a Nicolet iS50 FT-IR spectrometer equipped with a

Nicolet Continuum Infrared Microscope and a liquid-nitrogen cooled mercury cadmium-telluride (MCT) detector. The Cassegrain objectives used in this spectrometer have an opening angle between 16° and 35.5° relative to the normal.

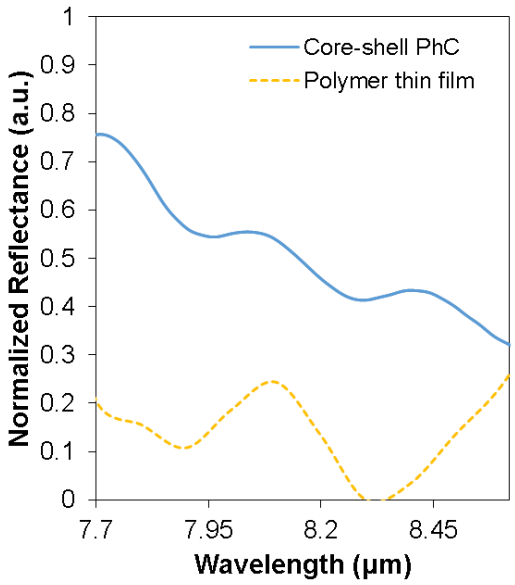

Figure 37. Normalized FTIR reflectance spectra for the polymer-Ge core-shell bcc PhC lattice compared to reflectance from an IP-Dip polymer thin film.

We look at the reflectance of the core-shell structure in the region of interest between 7.7μm to 8.62μm. As shown in Figure 37, we observe two dips in reflectance in this wavelength span at 7.96μm and 8.30μm. Reflectance intensity can be modified when incident light either couples into a photonic band or mode, or undergoes material absorption. We compare the position of these PhC dips in reflectance to the optical response of a 1.9μm thick IP-Dip polymer film and determine that the dip at 8.30μm is due to strong absorption from the polymer core material, while the dip at 7.96μm can be attributed to incident light coupling into a photonic band.

4.5.2. Angle resolved Infrared Spectroscopy for Band Mapping

FTIR reflectance measurements are taken over range of angles, meaning that such spectra give us convoluted momentum space information. In order to truly observe and distinguish photonic states, i.e. photonic bands of our 3D core-shell PhCs, a setup is required that can perform angle resolved spectroscopic measurements. One such system was designed and built by Dr. Siying Peng during her graduate research

in the Atwater group at Caltech. The setup consists of a quantum cascade laser (QCL) with an operating mode between 7.7-8.62 μm as the source, a series of ZnSe lenses to focus the laser beam down to spot size approximately 100μm in diameter, and a germanium beam splitter to direct half of the laser beam to a reference detector, and half to the sample. Pyroelectric sample and reference detectors are mounted on concentric rotation stages allowing for the collect of transmission and reflection spectra at distinct angles of incidence. Alignment of the laser beam and the photonic crystal sample is accomplished using a visible CCD camera and alignment markers. More precise micron scale alignment is performed by transmitting QCL light through the sample, and projecting the magnified image onto a mid-IR camera with MCT detector to determine sample edges versus the sample center. A more in-depth description of the setup may be found in reference 66.

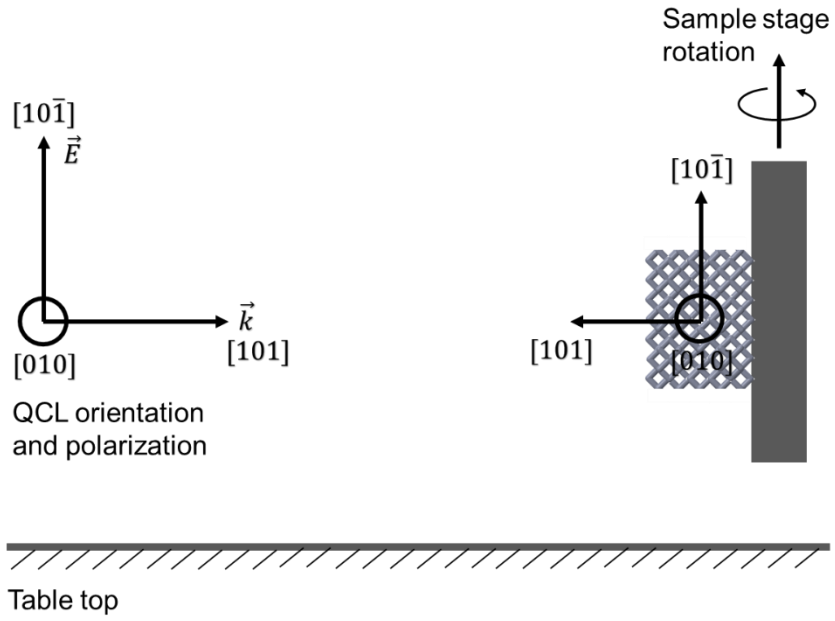

Figure 38. Schematic of the orientation of incident QCL laser light relative to the PhC sample orientation. This is a side view of the experimental setup. It should be noted that incident light is polarized along the [10$\bar{1}$] direction.

For the angle resolved reflectance measurements the incident laser light is polarized in the [10$\bar{1}$] direction relative to the lattice, and interacts with the (101) PhC surface, as can be seen from the schematic in Figure 38. The wavelength range for these measurements is between 7.7 and 8.62μm. The angular range covered in the experiments was limited from θ = 22.5° to 45° (where θ is the angle between the incident

beam and the normal to the crystal surface) due to limitations imposed by the experimental setup. Namely, the size of the detector prevents access to angles below 22.5°, and beyond 45° the reflectance signal is too low due to the smaller effective cross section of the samples at large angles.

4.5.3. Experimental Observation of a Photonic Band Relevant for Negative Refraction

The band structure of our bcc core-shell PhC is constructed from angle resolved reflectance spectra captured between 22.5° to 45°. The setup does not allow for characterization at normal incidence or near the light line, and because we cannot probe at or below the light line, we cannot access the AANR region of the PhC. However, if the curvature of the observable band is concave down, we should still have a frequency region with a negative effective index between $-1 < n_{eff} < 0$.[56] The experimentally measured band structure for our core-shell PhC lattice is shown in Figure 39(a). We observe the emergence of a photonic mode in this angle and wavelength region which has concave down character, and seems to replicate the appearance of the third band. Analogous to what we observed in the FTIR reflectance spectra, coupling into the band is marked by a decrease in reflection intensity in the region between 7.7 and 8.1μm. Reflectance is also relatively low between 8.3 and 8.62μm but this is due to absorption by the PhC's polymer core. Compared to FTIR, angle resolved spectroscopy has the ability to selectively excite photonic states at precise momentum and wavelength, providing a clear picture of photonic band structure.

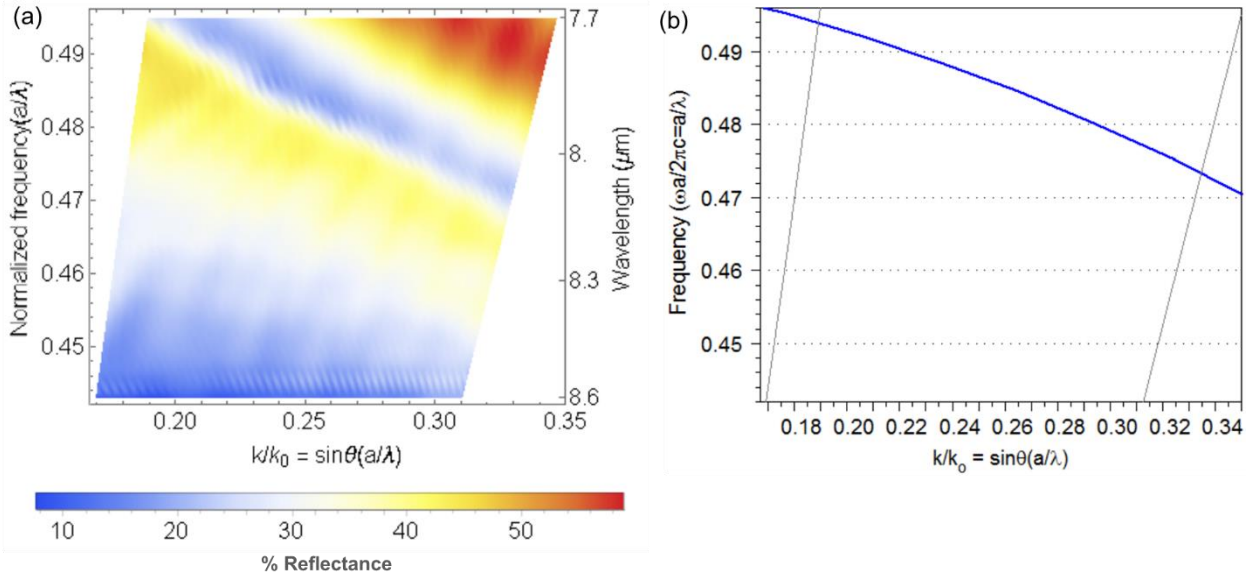

Figure 39. Experimentally measured and calculated band structure for the core-shell PhC lattice. (a) Angle resolved reflectance measurement showing band 3. (b) Simulated band structure for the same frequency and angle range in part (a).

4.5.4. Comparison of Experimental Band Structure and PWE Simulation Results

We compare the experimentally derived angle resolved band map in Figure 39(a) to a band structure calculated using PWE in Figure 39(b). The simulated PhC took into account the structural features and lattice dimensions determined through FIB and SEM measurements. The unit cell size was set to 3.8μm, and beam ellipticity, taper, and Ge shell offset were accounted for. Namely the polymer core was approximated as an elliptical beam with long axis and short axis dimensions of 650nm and 450nm respectively. Taper was introduced to polymer beams pointing in the [010] direction by changing the long axis dimension of their starting vertex to 250nm and while keeping it at 650nm at the ending vertex, creating a core resembling an elliptical conical frustrum. The germanium shell was described by embedding the polymer core in an elliptical beam of Ge with long axis and short axis dimensions of 1.1μm and 860nm respectively. The Ge shell beams were also offset from the polymer core beams by 200nm in x, y, and z, yielding a representative core-shell PhC for simulation. We calculate the band structure for this PhC approximation in the frequency range between $\omega = 0.441(2\pi c/a)$ and $\omega = 0.494(2\pi c/a)$ and angular span between 22.5° to 45° along the ΓN direction, and the experimentally measured and simulated band structures show great agreement (Figure 39).

In Figure 40(a) we plot an EFC for the band shown in Figure 22 at ω = 0.474(2π*c*/*a*) and look specifically at how an incident wave is refracted within the PhC. Note that the PhC contour is nearly circular so negative refraction should be expected. The incident wave can be thought of as coming from free space or air, at an angle of 25° to the surface normal, and interacts with the PhC surface orientated in the ΓN direction. Under conservation of energy and parallel momentum, the incident wave excites a Bloch wave inside the PhC whose solutions, characterized by $\vec{k}_{PhC}$ and $\vec{v}_g^{PhC}$, must lie along the dashed line (running perpendicular to the interface). The refracted beam has the direction of $\vec{v}_g^{PhC}$, which for this particular frequency and angle is -39°. We can now use Snell's law to calculate the corresponding index for this refraction angle, which we find to be n_{eff} = -0.673.

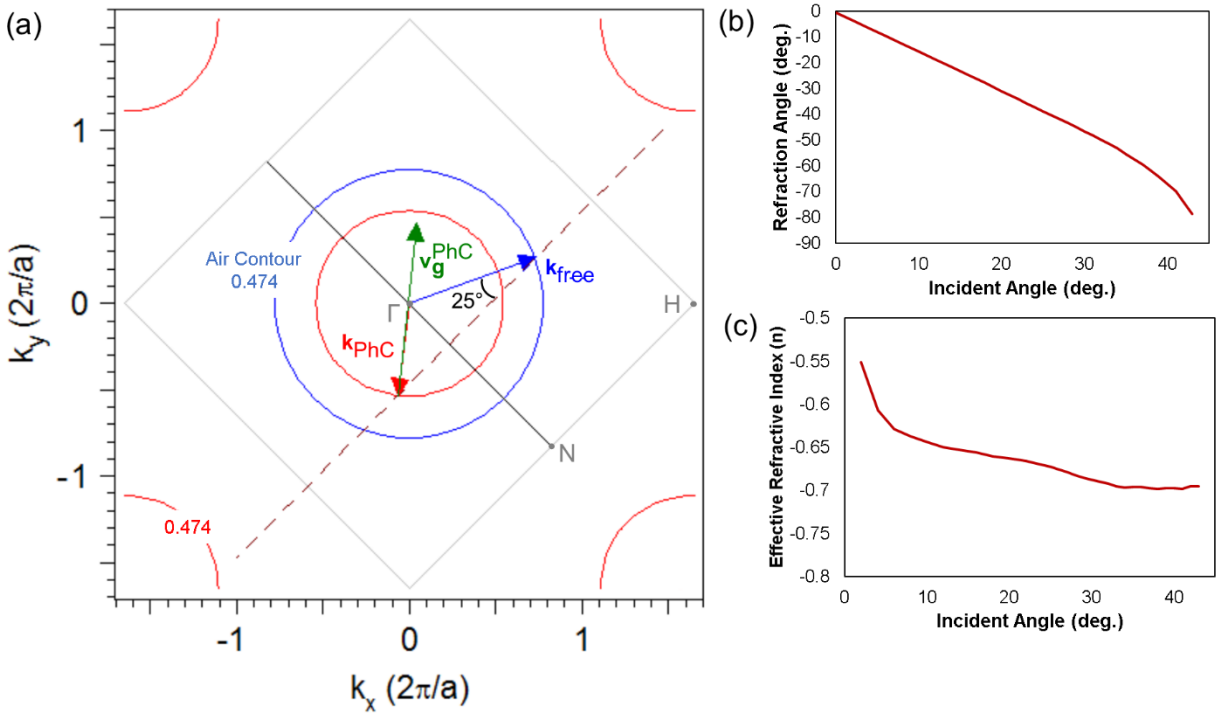

Figure 40. EFC plot and beam propagation construction inside the core-shell bcc PhC and resulting plots of negative refraction and negative effective index. (a) EFC plot and beam propagation construction inside the core-shell bcc PhC for a selected wave vector $\vec{k}_{free}$ (blue arrow), incident at 25° to the interface normal (dotted line). The PhC wave vector is marked by a red arrow, and the group velocity/beam propagation direction is given by the green arrow. The beam is refracted negatively by -39°. (b) Refraction angle versus incident angle for ω = 0.474(2π*c*/*a*). (c) Effective refractive index as a function of incident angle for ω = 0.474(2π*c*/*a*).

Figure 40(b) shows the refraction angle versus incident angle for the EFC at ω = 0.474(2π*c*/*a*). For incident angles larger than 43°, the beam propagation construction, as described in Figure 23(a), does not

give an intersection point of the EFC with the dotted line denoting the normal line to the PhC-air interface. This occurs because conservation of the parallel wave vector component is no longer fulfilled. At ω = 0.474($2\pi c/a$) specifically, incident waves at angles larger than 43° cannot couple to the PhC, and will instead be totally reflected.

Figure 40(c) plots the effective refractive index as a function of incident angle for ω = 0.474($2\pi c/a$). Because the EFC at this frequency is not perfectly circular, effective refractive index varies depending on incident angle. However, the calculated effective index for our core-shell bcc PhC is negative, with an average value of $n_{eff} = -0.67$.

It should be noted that in the case of PhCs, group and phase refractive index are unique and separate, and the values calculated above for effective refractive index represent the effective index of the PhC as an incident beam would experience in accordance with Snell's law of refraction.[67] However, these effective indices determine only the direction of the group velocity vector $\vec{v}_g^{PhC}$, as the magnitude calculated for these effective indices would yield velocities larger than the speed of light, which would be unphysical.[68]

4.6. Conclusions and Outlook on the Experimental Observation of Negative Refraction with 3D PhCs

We have systematically analyzed the dispersion phenomena and negative refraction properties of polymer-germanium core-shell PhCs in the mid-infrared using band theory and angle resolved spectroscopy. Band structure and equifrequency contour calculations were performed to inform the design of the 3D photonic crystal, which was subsequently fabricated using TPL DLW and sputtering. We were able to successfully characterize a polymer-Ge core-shell lattice and map its band structure, which we then used to calculate PhC refraction behavior. Analysis of wave-propagation revealed that this 3D core-shell PhC will refract light negatively, and possesses an effective negative index of refraction in the region we experimentally mapped.

4.6.1. Creation of a 3D Core-Shell PhC Superlens

However, negative refraction can also be demonstrated by utilizing the PhC as a superlens. As briefly mentioned previously, a superlens composed of negative index material is capable of capturing both the

propagating and evanescent waves emitted by a point source placed in front of the lens and refocusing them into a perfect point image behind the lens, even for a slab design with parallel sides or flat edges. While the focusing effect of propagating waves can be described using conventional geometric optics, the perfect recovery of evanescent waves may also be achieved via amplified transmission through the negative-index slab.[69] Such a superlens possesses several key advantages over conventional, convex lenses; a flat superlens lacks an optical axis, implying that strict alignment of an object with the focal axis is not necessary. A superlens also operates over distances on the order of wavelengths, meaning such lenses are ideal candidates for small-scale integration. AANR for a superlens also means that there is essentially no physical limit on the aperture of this imaging system. Finally, for superlensing at a given configuration and wavelength, the resolution of a superlens is expected to be limited by the surface period, the characteristic length of a photonic crystal.[69]

In 2003 Luo et. al. described the principles of the amplified transmission of evanescent waves and superlensing in general photonic crystals, and presented specific designs of superlenses based on AANR in PhCs, along with a numerical study of their subwavelength imaging properties.[69] In 2005 Lu et. al. fabricated a 3D BCC lattice PhC flat lens which demonstrated superlensing, or sub-wavelength imaging, via AANR and the amplification of evanescent microwaves.[57,58] In the vein of these projects, another logical method for demonstrating negative refraction through our 3D core-shell PhCs is to utilize them as superlenses operating in the mid-IR wavelength range.

Studying the superlensing capabilities of our 3D core-shell PhCs operating in the mid-IR will require the use of scanning near-field optical microscopy (SNOM). In SNOM, excitation laser light is focused through an aperture of a metallic probe tip with a diameter smaller than the excitation wavelength, resulting in an evanescent field on the far side of the aperture. When the sample is scanned at a small distance below the aperture, the optical resolution of transmitted or reflected light is limited only by the diameter of the aperture. While this process allows for optical resolution as small as $\lambda/60$,[70] a deficit of SNOM is that the scanning probe must be very close to the investigated object, limiting SNOM applications to surface studies. Combining near-field microcopy with a superlens, however, can enable subwavelength-scale resolved

imaging of buried objects, even beneath opaque substrates. Namely, a superlens like our 3D core-shell PhC can be placed between the scanning probe tip of an infrared SNOM operating in reflection mode, and an object to be imaged, like gold film patterned with holes of different diameters and separations. In contrast to the first proposed demonstration of negative refraction by our 3D core-shell PhC using transmission experiments, this setup allows for direct mapping of an image plane with SNOM, recording both the amplitude and the phase of the optical field distribution. In fact, this process was recently used to demonstrate the superlensing capabilities of a silicon carbide (SiC) thin film,[71] but could easily be applied to the characterization of metamaterial and PhC superlenses from the visible to terahertz frequencies.

Chapter 5. Perspectives on Future Research Directions for 3D Photonics

5.1. Opportunities in PhC Architecture and Topology

In this thesis we have utilized experiments and simulations to understand the effects of particular lattice geometries and material properties on 3D PhC bandgap position and dispersion phenomena like negative refraction. This work contributes to the greater field of 3D photonics, and with that we posit the question, what are some imperative research directions for subsequent work on 3D PhCs? To this end, we believe that areas of critical exploration will revolve around (1) the creation of new architectures, possibly even non-periodic geometries, (2) the study of topology and photonics, and (3) the exploration of novel chemistries and material synthesis routes for the fabrication of high index 3D PhCs.

New methodologies for engineering the band gap and dispersion characteristics of PhCs will enable the creation of functional integrated photonic circuits. With regards to new mechanisms for tuning band gap properties, we envision applying concepts from cellular solid mechanics in designing auxetic lattices possessing a negative Poisson's ratio.[72,73] This property would allow the PhC lattice period to be modulated isotropically, enabling a more complex band structure manipulation through the application of mechanical strain. By exploiting various dispersion properties of PhCs, one may precisely control the wave propagation direction in a PhC for a given incident wave. With dispersion engineering, an alternative exists to generating conventional PhC waveguides where line defects are built into the structure. Instead, by designing an architecture which can exhibit a specific band structure, and by extension uniquely shaped equi-frequency surfaces, it will be possible to arbitrarily route light by exploiting engineered dispersion. This new class of devices, namely dispersion-based PhC devices, can in principle achieve extremely low propagation losses while splitting incident light by the superprism effect, or bending incident light via self-collimation. Understanding and fabricating 3D PhC architectures capable of the superprism effect and self-collimation, and integrating these structures on a single chip to operate in tandem, will be hugely impactful for the field of photonics.

5.1.1. Topological Photonics

Topological photonics is another research area that has lately captured a great deal of scientific attention.[74–77] Very basically, topology is the branch of mathematics which deals with quantities that do not change when an object is continuously deformed, no matter the extent of deformation. One classic example of a topological property, or topological invariant, is the number of holes within a closed surface. Objects with the same topological invariant are topologically equivalent, and only when a hole is created or removed in the object, by the introduction of a cut, will the topological invariant change, the process being a topological phase transition. In solid state systems, the Brillouin zone is analogous to a surface, and the geometric phase, or Berry phase, looks at changes in crystal momentum, analogous to surface curvature.

In the same way the study of photonic crystals benefited from an understanding of electronic crystals, topological photonics was prompted by the discovery of electronic topological insulators.[78,79] Topological insulators are unique due to the existence of protected states occurring at crystal boundaries. Protected states support unidirectional propagation and are immune to a wide class of crystal impurities and defects. Given all the analogs between solid state systems and photonic systems, many quantum topological effects are being translated to the field of photonics. Indeed, quantum topological effects are a consequence of the wave nature of electrons, and light can be characterized as a wave as well. While photons do not experience electric potential as they have no electric charge, their motion is governed by the periodic change in dielectric contrast, which is analogous to electronic potential. For 3D PhC systems, one particular area of study has been the observation of Weyl points in a photonic band structure.[80,81] Theoretical and experimental observation of Weyl points is currently being pursued, given the numerous phenomena which can result from this topological feature.[82]

From a practical standpoint, topological effects will allow for substantially more robust photonic devices. Current PhC fabrication processes are not immune to defects, and topologically insulating structures would relax certain device fabrication constraints. In particular, topological insulators could resolve issues like insertion losses, Fabry–Pérot oscillations, lattice disorder, and unwanted localization.[74]

The fabrication of optically active, topological photonic structures is currently the main challenge of this growing field, and consequently an area for future research.

5.1.2. Photonic Quasicrystals

In this thesis we have discussed at length the properties of 3D periodic structures. Interestingly though, recent research has revealed that quasi-periodic structures, or quasicrystals, also possess unique photonic properties that require further exploration.[83–87] Quasicrystals are a class of structures that do not have translational symmetry, but possess local rotational symmetry. Because the structures of photonic quasicrystals have no periodicity, the Bloch wave vector $\vec{k}$ cannot be defined exactly, and it is not possible to draw a conventional photonic band structure such as that for a typical PhC. However, photonic quasicrystals exhibit Bragg scattering of light, and a quasi-Brillouin zone can be defined on the basis of a quasicrystal's long range order.[87] This fact suggests that a pseudo-photonic band structure can be created for photonic quasicrystals, and that some of the band gap and dispersion properties evident in periodic photonic crystals may also be realizable in photonic quasicrystals.

The photonic dispersion relations in a band structure govern the basic properties of light propagation, and in periodic PhCs, a complete photonic bandgap arises when frequency gaps at the Brillouin zone boundaries overlap in all directions. The appearance of pseudo-bandgaps, or directional stop bands, depend on the symmetry of the underlying photonic crystal lattice. In photonic quasicrystals, as the rotational symmetry of the quasicrystal increases, the pseudo-Brillouin zone will become more spherical in 3D, which can result in the formation of a complete bandgap.[83,88] A study by Man et. al. discussed how, even for low dielectric contrast structures, the increased isotropy of quasicrystals gives these structures an increased likelihood of possessing a complete bandgap.[83] In contrast, for high dielectric contrast, light scattering in an architecture gets stronger, overwhelming the advantage of isotropy and allowing periodic photonic crystals to perform better.[83] Nonetheless, these findings imply that photonic quasicrystals can be more advantageous in various photonic bandgap applications relative to periodic PhCs, at threshold material index values.

With regards to dispersion properties of quasicrystals, work done by Feng et. al. reported that a 2D photonic quasicrystal with dodecagonal symmetry exhibits negative refraction.[86] The photonic quasicrystal under study consisted of a quasiperiodic arrangement of dielectric columns with ε = 8.6, embedded in a styrofoam background and was active in the microwave frequency regime. Refractive properties were investigated by creating wedge samples with different wedge angles, θ_0, and measuring the refracted wave intensity versus the angle of refraction of an incident k-vector through the quasicrystal wedge. For $\theta_0 = 30°$, a peak in intensity was observed at the refraction angle $\theta = -32°$, corresponding to a negative refractive index of n = -1.06. This result was verified by a numerical simulation based on multiple-scattering theory, and further measurements indicated a refractive index of $n \approx -1$ over a substantial range of incident angles. However, opportunities still exist in fabricating 3D photonic quasicrystals capable of AANR, and demonstrating negative refraction in quasicrystal structures at infrared and optical frequencies. Additionally, a recent report from Kraus et. al. demonstrated that quasicrystals can exhibit topological phases that were previously thought to exist only for systems of higher dimensionality.[89] This work posits that the study of topological phases in 3D photonic quasicrystals may lead to the discovery of topological properties that would only have appeared in 6D periodic systems.[89] It is therefore clear that the intersection of topological photonics and quasicrystals is a minimally explored frontier that can yield unprecedented insights into higher dimensional photonic properties.

5.2. Future Directions for Index of Refraction Engineering and 3D Photonic Crystal Fabrication

Other areas of research that must be explored in order to fully unlock the technological potential of 3D PhCs include routes for tailoring PhC material properties, and methods for fabricating high resolution PhCs capable of operating in the optical regime.

Though 3D PhC properties have been explored via theory and computational means, fabrication and experimental observation of 3D PhC behavior in the optical and infrared regime has only become possible in the last twenty years. Initially, simple layered photonic lattices were created using top-down semiconductor fabrication techniques,[90] but, more complex 3D lattice architectures were enabled through

the advent and refinement of two photon lithography (TPL) direct laser writing (DLW) technology.[91] As described previously, in TPL DLW, an infrared laser is used to crosslink and write a preprogrammed 3D lattice pattern into a photopolymer via two-photon absorption.[60] The exposed sample is developed using standard lithographic solvents, resulting in freestanding 3D architectures with micro- to nanoscale features. The TPL DLW process allows for maximum control over nanolattice architecture and enables the fabrication of arbitrarily complex nano- and micro-structures.[60] One drawback of this technology however, is the reliance on photopolymerizable materials for the fabrication of nanolattice PhCs. Photopolymers are largely acrylate or epoxy based, and have a relatively low refractive index of >1.7, which can limit the photonic band gap properties of polymer-based PhCs.[92] In an effort to overcome some of the practical shortcomings of polymer PhCs, we can look towards designing and fabricating core-shell 3D PhCs, as described in Chapter 4 of this thesis, or, we could pursue alternative methods for the direct fabrication of high index 3D PhCs.

Several methods exist for direct fabrication of high index 3D PhCs. The double inversion method is one possibility which has been explored mostly in the context of generating of 3D silicon structures,[93–95] with only one example existing for the fabrication of a solid germanium inverse woodpile structures.[96] In the double inversion method, a polymer template is first fabricated using TPL DLW. The template is then infiltrated with an oxide (SiO_2 in the case of silicon double inversion) using a chemical vapor deposition process (CVD). The polymer is then exposed and etched away either with O_2 plasma etching or calcination, followed by CVD infiltration of the template with the desired high index material (Si or Ge). The remaining oxide material is finally chemically etched away, revealing the high-index 3D replica. Optimizing the double inversion process for Ge and applying it to non-conventional geometries (outside of woodpiles, inverse woodpiles, and inverse opals) would be a meaningful step towards the fabrication of novel high index PhC architectures.

Another intriguing method is generating high-index polymer 3D PhCs using a high index photoresin with a refractive index comparable to that of the AANR capable core-shell lattices ($n_{eff} \geq 2.5$). Conventional polymers typically possess a refractive index, *n*, in the range of 1.30–1.70.[97] However, in recent years,

hybrid chemistry techniques have been adopted to develop high index refractive polymers which combine an organic polymer matrix with highly refractive inorganic nanoparticles.[97] The factors affecting the refractive index of a high-*n* nanocomposite include the properties of the individual polymer matrix and nanoparticles, and the chemistry linking inorganic and organic components.[97] In particular one can look at the synthesis of nanocomposite materials based on hybrid networks of organically modified, inorganic oxide clusters dispersed in a polymer host matrix.[98] Organically modified inorganic oxide clusters can be obtained by a reaction of inorganic-based alkoxides with carboxylic acids.[98] Exposing the organic-inorganic hybrid system to UV light results in homogeneous photopatterning and modification of polymer host refractive index properties.[98] Developing hybrid organic-inorganic chemistry amenable for use with TPL DLW would allow for this fabrication methodology to be used in the fabrication of 3D PhC architectures of the sort described in this thesis. Recently, Vyatskikh et. al. described a similar process for fabricating nickel nanolattices via TPL DLW.[99] A ligand exchange reaction was used to synthesize a metal precursor with polymerizable functionalities by reacting nickel alkoxide with a carboxylic acid. Nickel oxide clusters were then mixed with pentaerythritol triacrylate, a common acrylate based monomer, and a small amount of 7-diethylamino-3-thenoylcoumarin photoinitiator. Using this new hybrid photoresin, metallo-organic 3D structures were directly fabricated via TPL DLW. Once these structures were pyrolysed, the result was fully metallic 3D structures with sub-micron features. Based on the synthesis of a nickel oxide cluster-acrylate hybrid resin, one natural extension of hybrid organic-inorganic chemistry techniques would be the development of high index germanium and/or zirconium alkoxide clusters bonded to pentaerythritol tetraacrylate monomers, which will polymerize by two-photon absorption of UV light. The development of such a novel high index Ge-nanocluster resin will allow for the one-step fabrication of high index 3D nanoarchitected structures, more easily enabling the experimental observation of phenomena like negative refraction and full photonic band gaps in complex 3D PhCs.

Also critical to fabricating 3D PhCs active in the optical regime is increasing the resolution of printed 3D PhCs. The spatial resolution of direct laser writing as used in this work can be much smaller than the free-space wavelength of the writing laser used. Nevertheless, the minimum feature size is fundamentally

limited by the wavelength of light. One method for overcoming this limitation is the application of stimulated emission depletion (STED) to direct laser writing. In this process, the photo-polymerization of PETA can be effectively inhibited by exposing the monomer voxel to laser light of a second, different wavelength, resulting in a size-reduction of written features.[100] Such an exposure enables the breaking of the diffraction limit in lithography, and should STED become adopted in commercial DLW systems, it is not unrealistic to posit that 3D PhCs can be fabricated with minimum feature sizes of tens of nanometers within the foreseeable fututre.

Appendicies

Appendix A.

Absorption Features in FTIR Spectra

The main chemical component in the IP-Dip photoresist is the monomer pentaerythritol triacrylate. Several of the sharp, intense dips we observe in our nanolattice spectra are due to absorptions from the polymer material, and are not optical features due to the nanolattice architecture. A few of these material absorptions cut right through the relevant stopband features of the lattice—namely the dips at 5.78μm and 7.1μm—making it seem as though the stopbands are split for nanolattices under particular strain. The mid-IR region is ideal for observing various fundamental vibrations and associated rotational-vibrational modes of organic functional groups, which is why the aforementioned absorption features in our FTIR spectra are inevitable. In Figure 41 we have overlaid spectra collected from both an unstrained nanolattice and a 1.9μm thin film made from TPL cured IP-Dip photoresist, and observe that prominent absorption features exist in both spectra. This implies that the dips are in fact due to the excitation of vibrational modes of the polymer material, rather than the photonic structure of the lattice.

We can even characterize some of the absorption dips as follows: the intense absorption band, highlighted in light blue, observed at 5.78μm (1730 cm^{-1}) is due to the antisymmetric stretching vibration of C=O group[40]. The double peaked absorption dip, highlighted in light green, at 6.11μm and 6.18μm (1636 and 1618 cm^{-1}) is designated to the antisymmetric stretching of the polymer's C=C groups[40]. The regions at 6.80μm and 10.16μm (1470 and 984 cm^{-1}), highlighted in light yellow, are due to (CH) in-plane deformation[40]. The various absorptions highlighted in the broad light orange band spanning between 7.87μm and 9.43μm (1270 and 1060 cm^{-1}) are ascribed to CO stretching modes[40].

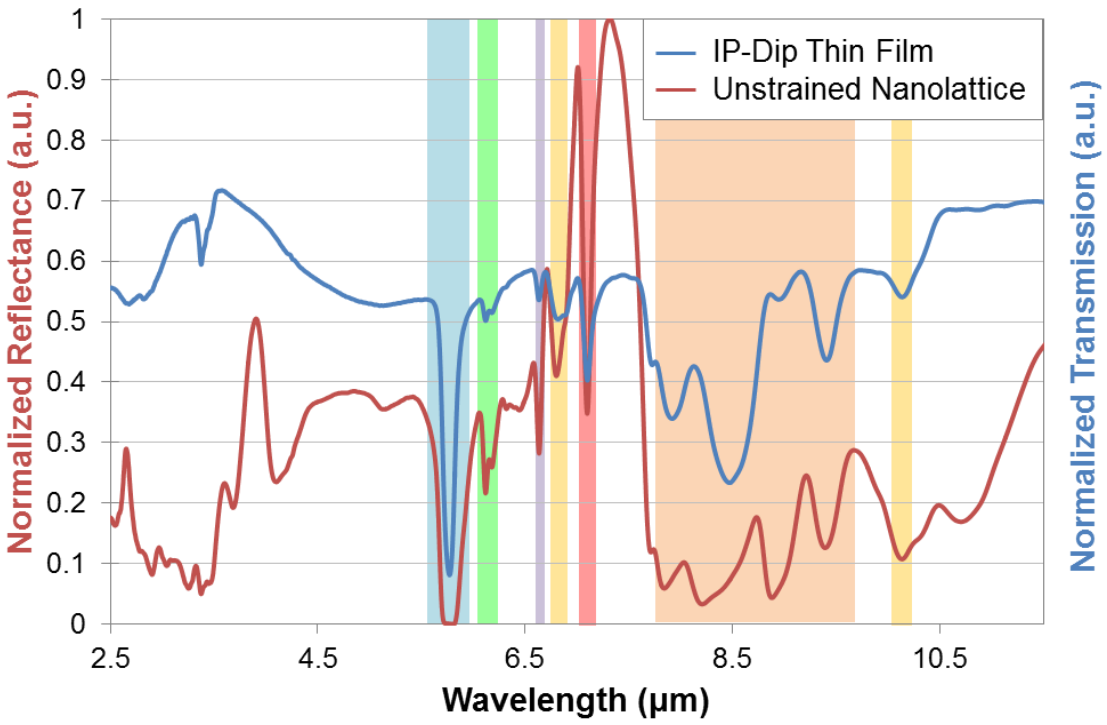

Figure 41. FTIR spectra of an unstrained 45° octahedron nanolattice, and a 1.9μm cured thin film of IP-Dip photoresist (the same polymer as in the nanolattices). Colored areas highlight regions in both spectra where absorption features exist, showing that these dips are due to excited vibrational modes of the polymer material, and not to the photonic structure of the lattice.

Appendix B.

Refractive Index Calculation for IP-Dip Polymer

To optically characterize IP-Dip polymer we took several FTIR reflectance measurements on IP-Dip thin films with thicknesses ranging from 2.7, 7.4, and 11.8 μm. These films were fabricated on polished silicon using the same TPL DLW parameters as were used to make the nanolattices. This fabrication methodology was used in order to assure that the polymer films had the same cross-linking density as the nanolattice structures, for accurate characterization. Reflection from each sample was measured using the same FTIR microspectroscopy setup as for the nanolattices. Figure 42 shows the reflectance spectra collected for the 7.4μm IP-Dip film. As can be seen in the low energy (long wavelength) parts of the spectrum, the reflected data is convoluted with many vibrational and resonant modes of the polymer, as could also be seen in the spectra displayed in Figures 8 and 17. For shorter wavelengths, a scattering matrix approach combined with a minimization technique was employed to fit the measured data to the reflected spectrum of a polymer-on-Si system. This led to a calculated effective refractive index of n~1.49 for the polymer over the entire spectral range of interest, which we used in subsequent numerical calculations.

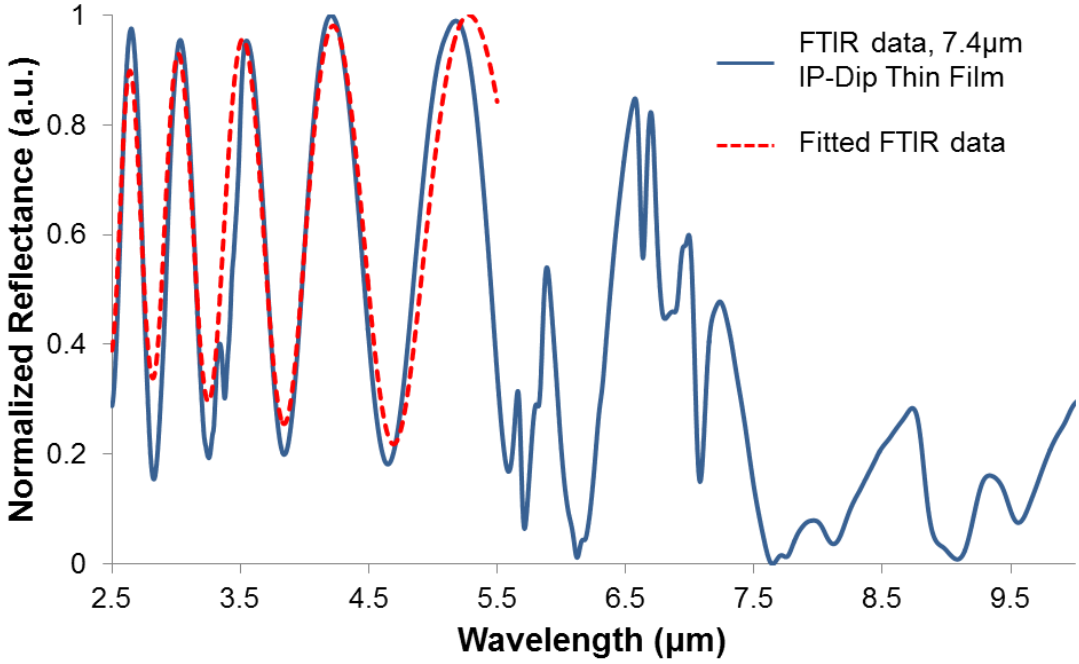

Figure 42. FTIR reflectance spectra for a 7.4μm TPL cured IP-Dip thin film, and a fitting curve for the reflectance data extending from 2.5-5.5μm (beyond 5.5μm, the data is too heavily convoluted by absorption dips).

This fit was determined using a scattering matrix approach combined with a minimization technique, and led us to calculate an effective refractive index of n~1.49 for the cured IP-Dip polymer.

IR-VASE ellipsometry would have been the preferred method for determining the refractive index of IP-Dip, but, since this resist is designed to be drop cast and polymerized using two-photon absorption, spin coated and UV-flood exposed samples did not possess the film uniformity or crosslinking density necessary to obtain accurate index measurements with this technique.

Appendix C.

Band Diagrams for Octahedron Nanolattices in Chapter 2

To fully characterize the properties of a photonic crystal structure, calculating band diagrams can be a proper starting point. Band diagrams show the dispersion of the lattice when the momentum of the modes varies in the 1st Brillouin zone in the reciprocal lattice as a function of energy. The reciprocal lattice for a cubic crystal like our octahedron nanolattice is also cubic. Figure 28 shows the band diagrams for the 45° (unstrained) and 30° (~40% strained) nanolattice in the 1st Brillouin zone. The inset of panel (a) in Figure 28 shows the momentum directions and the common symbols in a cubic lattice.

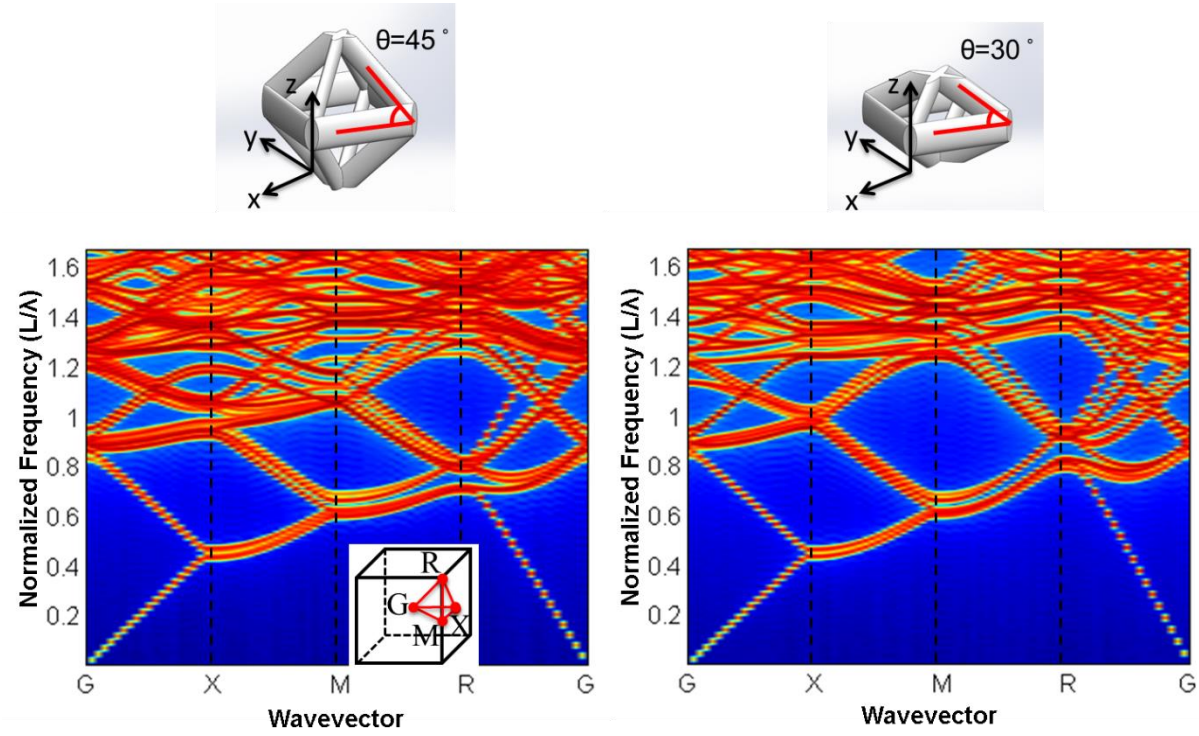

Figure 43. FDTD simulations of octahedron nanolattices. (a) Calculated band diagrams of the modes for an unstrained 45° lattice, and (b) an effectively strained 30° lattice. In each case the horizontal axis shows the momentum along the edges of the Brillouin zone, and the vertical axis shows the normalized frequency defined as $\boldsymbol{L_{x,y}/\lambda}$.

To calculate the bands, an octahedron unit cell with experimentally relevant feature sizes and dimensions was modeled using the software package Lumerical. The model unit cell was surrounded by Bloch boundary conditions along all three x, y, and z directions. An array of randomly oriented dipoles was placed in the simulation region, located far from any lattice symmetry points. Simulations were allowed to

run until they converged with an accuracy of 10^{-6}. Scattering data was collected using point monitors located at random locations in the simulation region, also far from any symmetry points of the lattice. The collected data was then Fourier transformed to locate the peaks in the spectral domain corresponding to the oscillating modes in both the unstrained, 45° octahedron unit cell, and the effectively strained 30° octahedron unit cell. Plotting these peaks at each Bloch momentum along the edges of the Brillouin zone produced the full band diagram for the two most extreme lattice types studied in this manuscript, as shown in Figure S6.

Although this band diagram is for a fully periodic lattice in 3D, some general features can still be inferred from it. Our wavelength range of interest (4μm-10μm), corresponding to the range of FTIR measurement, can be related to the part of the band diagram with the normalized frequency between 0.4-1. As can be seen in Figure S6, none of the lattices support a complete band gap within this range, but, in both lattice cases, partial band gaps can be observed at the edges of the high symmetry points, namely G, X, M and R. The presence of these partial band gaps leads to a minimum in the transmission and a peak in the reflection spectrum. Also note that decreasing the layer spacing along the z-direction, which can be represented in going from the 45° lattice to the 30° lattice (and which physically corresponds to uniaxial lattice compression), all the energy gaps in the band structure shift to larger normalized frequencies. This is consistent with the general blue shift observed in the reflection spectra from stacked photonic crystals.

References

1. Yablonovitch, E. Inhibited spontaneous emission in solid-state physics and electronics. *Phys. Rev. Lett.* **58,** 2059–2062 (1987).
2. John, S. Strong localization of photons in certain disordered dielectric superlattices. *Phys. Rev. Lett.* **58,** 2486–2489 (1987).
3. Joannopoulos, J. D., Johnson, S. G., Winn, J. N. & Meade, R. D. *Photonic crystals: molding the flow of light*. (Princeton University Press, 2008). doi:10.1063/1.1586781
4. Chan, E. P., Walish, J. J., Urbas, A. M. & Thomas, E. L. Mechanochromic photonic gels. *Adv. Mater.* **25,** 3934–47 (2013).
5. Blanco, A. *et al.* Large-scale synthesis of a silicon photonic crystal with a complete three-dimensional bandgap near 1.5 micrometres. *Nature* **405,** 437–40 (2000).
6. Noda, S., Tomoda, K., Yamamoto, N. & Chutinan, A. Full Three-Dimensional Photonic Bandgap Crystals at Near-Infrared Wavelengths. *Science* **289,** 604–606 (2000).
7. Arsenault, A. C. *et al.* From colour fingerprinting to the control of photoluminescence in elastic photonic crystals. *Nat. Mater.* **5,** 179–184 (2006).
8. Fink, Y. *et al.* A Dielectric Omnidirectional Reflector. *Science* **282,** 1679–1682 (1998).
9. Hart, S. D. *et al.* External reflection from omnidirectional dielectric mirror fibers. *Science* **296,** 510–513 (2002).
10. Yoon, J. *et al.* Defect-mode mirrorless lasing in dye-doped organic/inorganic hybrid one-dimensional photonic crystal. *Appl. Phys. Lett.* **88,** 15–18 (2006).
11. Ben-Moshe, M., Alexeev, V. L. & Asher, S. a. Fast responsive crystalline colloidal array photonic crystal glucose sensors. *Anal. Chem.* **78,** 5149–5157 (2006).
12. Fortes, L. M., Gonçalves, M. C. & Almeida, R. M. Flexible photonic crystals for strain sensing. *Opt. Mater. (Amst).* **33,** 408–412 (2011).
13. Chan, E. P., Walish, J. J., Thomas, E. L. & Stafford, C. M. Block copolymer photonic gel for

mechanochromic sensing. *Adv. Mater.* **23,** 4702–4706 (2011).

14. Arsenault, A. C., Puzzo, D. P., Manners, I. & Ozin, G. a. Photonic-crystal full-colour displays. *Nat. Photonics* **1,** 468–472 (2007).

15. Hwang, K. *et al.* Electrically tunable hysteretic photonic gels for nonvolatile display pixels. *Angew. Chemie - Int. Ed.* **50,** 6311–6314 (2011).

16. Lu, Y., Xia, H., Zhang, G. & Wu, C. Electrically tunable block copolymer photonic crystals with a full color display. *J. Mater. Chem.* **19,** 5952 (2009).

17. Pryce, I. M., Aydin, K., Kelaita, Y. a, Briggs, R. M. & Atwater, H. a. Highly strained compliant optical metamaterials with large frequency tunability. *Nano Lett.* **10,** 4222–7 (2010).

18. Kang, Y., Walish, J. J., Gorishnyy, T. & Thomas, E. L. Broad-wavelength-range chemically tunable block-copolymer photonic gels. *Nat. Mater.* **6,** 957–60 (2007).

19. Han, M. G. *et al.* Full color tunable photonic crystal from crystalline colloidal arrays with an engineered photonic stop-band. *Adv. Mater.* **24,** 6438–44 (2012).

20. Yu, C. L. *et al.* Stretchable photonic crystal cavity with wide frequency tunability. *Nano Lett.* **13,** 248–52 (2013).

21. Yoshino, K., Shimoda, Y., Kawagishi, Y., Nakayama, K. & Ozaki, M. Temperature tuning of the stop band in transmission spectra of liquid-crystal infiltrated synthetic opal as tunable photonic crystal. *Appl. Phys. Lett.* **75,** 932 (1999).

22. Leonard, S. W. *et al.* Tunable two-dimensional photonic crystals using liquid-crystal infiltratio. *Phys. Rev. B* **61,** 2389–2392 (2000).

23. Xia, J., Ying, Y. & Foulger, S. H. Electric-field-induced rejection-wavelength tuning of photonic-bandgap composites. *Adv. Mater.* **17,** 2463–2467 (2005).

24. Busch, K. & John, S. Liquid-Crystal Photonic-Band-Gap Materials: The Tunable Electromagnetic Vacuum. *Phys. Rev. Lett.* **83,** 967–970 (1999).

25. Fudouzi, H. & Xia, Y. Photonic papers and inks: Color writing with colorless materials. *Adv. Mater.* **15,** 892–896 (2003).

26. Viel, B., Ruhl, T. & Hellmann, G. P. Reversible Deformation of Opal Elastomers. *Chem. Mater.* **19,** 5673–5679 (2007).

27. Sumioka, K., Kayashima, H. & Tsutsui, T. Tuning the Optical Properties of Inverse Opal Photonic Crystals by Deformation. *Adv. Mater.* **14,** 1284–1286 (2002).

28. Montemayor, L. C., Meza, L. R. & Greer, J. R. Design and Fabrication of Hollow Rigid Nanolattices via Two-Photon Lithography. *Adv. Eng. Mater.* **16,** 184–189 (2014).

29. Jang, D., Meza, L. R., Greer, F. & Greer, J. R. Fabrication and deformation of three-dimensional hollow ceramic nanostructures. *Nat. Mater.* **12,** 893–8 (2013).

30. Meza, L. R. & Greer, J. R. Mechanical characterization of hollow ceramic nanolattices. *J. Mater. Sci.* **49,** 2496–2508 (2014).

31. Tétreault, N. *et al.* New Route to Three-Dimensional Photonic Bandgap Materials: Silicon Double Inversion of Polymer Templates. *Adv. Mater.* **18,** 457–460 (2006).

32. Kim, J. Y. & Greer, J. R. Tensile and compressive behavior of gold and molybdenum single crystals at the nano-scale. *Acta Mater.* **57,** 5245–5253 (2009).

33. Park, W. & Lee, J.-B. Mechanically tunable photonic crystal structure. *Appl. Phys. Lett.* **85,** 4845 (2004).

34. Fudouzi, H. & Sawada, T. Photonic rubber sheets with tunable color by elastic deformation. *Langmuir* **22,** 1365–8 (2006).

35. Griffiths, P. R. & De Haseth, J. A. *Fourier Transform Infrared Spectroscopy*. (John Wiley & Sons, Inc., 2007).

36. Sözüer, H. S. & Haus, J. W. Photonic bands: simple-cubic lattice. *J. Opt. Soc. Am. B* **10,** 296 (1993).

37. Zhou, G., Ventura, M., Gu, M., Matthews, A. & Kivshar, Y. Photonic bandgap properties of void-based body-centered-cubic photonic crystals in polymer. *Opt. Express* **13,** 4390–5 (2005).

38. Urbas, a. M., Maldovan, M., DeRege, P. & Thomas, E. L. Bicontinuous Cubic Block Copolymer Photonic Crystals. *Adv. Mater.* **14,** 1850–1853 (2002).

39. Meza, L. R. Design, Fabrication, and Mechanical Property Analysis of 3D Nanoarchitected

Materials. (California Institute of Technology, 2016). doi:10.7907/Z9154F1K

40. Oueslati, A., Kamoun, S., Hlel, F., Gargouri, M. & Fort, A. Real-time FTIR and electrical monitoring of the photopolymerization of a pentaerythritol triacrylate-based resin. *Akademeia* **1,** 1–6 (2011).

41. Johnson, S. & Joannopoulos, J. Block-iterative frequency-domain methods for Maxwell's equations in a planewave basis. *Opt. Express* **8,** 173 (2001).

42. Joannopoulos J.D, Pierre R. Villeneuve, S. F. Photonic crystals:putting a new twist on light. *Nature* **386,** 7 (1997).

43. Braginsky, L. & Shklover, V. Light propagation in an imperfect photonic crystal. *Phys. Rev. B - Condens. Matter Mater. Phys.* **73,** 1–11 (2006).

44. Galisteo-López, J. F., Palacios-Lidón, E., Castillo-Martínez, E. & López, C. Optical study of the pseudogap in thickness and orientation controlled artificial opals. *Phys. Rev. B* **68,** 115109 (2003).

45. Vlasov, Y. A., Kaliteevski, M. A. & Nikolaev, V. V. Different regimes of light localization in a disordered photonic crystal. *Phys. Rev. B* **60,** 1555–1562 (1999).

46. Veselago, V. G. The electrodynamics of substances with simultaneously negative values of ε and μ. *Sov. Phys. Uspekhi* **10,** 509–514 (1968).

47. Luo, C., Johnson, S. G., Soljačić, M., Joannopouls, J. D. & Pendry, J. B. Novel optical phenomena with photonic crystals. *Proc. SPIE - Int. Soc. Opt. Eng.* **5166,** 207–219 (2004).

48. Pendry, J. B., Holden, A. J., Stewart, W. J. & Youngs, I. Extremely Low Frequency Plasmons in Metallic Mesostructures. *Phys. Rev. Lett.* **76,** 4773–4776 (1996).

49. Pendry, J. B., Holden, A. J., Robbins, D. J. & Stewart, W. J. Magnetism from conductors and enhanced nonlinear phenomena. *IEEE Trans. Microw. Theory Tech.* **47,** 2075–2084 (1999).

50. Soukoulis, C. M., Linden, S. & Wegener, M. Negative Refractive Index at Optical Wavelengths. *Science* **315,** 47–49 (2007).

51. Shalaev, V. M. Optical negative-index metamaterials. *Nat. Photonics* **1,** 41–48 (2007).

52. Notomi, M. Theory of light propagation in strongly modulated photonic crystals: Reflectionlike

behavior in the vicinity of the photonic band gap. *Phys. Rev. B* **62,** 10696 (2000).

53. Baba, T., Matsumoto, T. & Asatsuma, T. Negative Refraction in Photonic Crystals. *Adv. Sci. Technol.* **55,** 91–100 (2008).

54. Luo, C., Johnson, S., Joannopoulos, J. & Pendry, J. All-angle negative refraction without negative effective index. *Phys. Rev. B* **65,** 2–5 (2002).

55. Cubukcu, E., Aydin, K., Ozbay, E., Foteinopoulou, S. & Soukoulis, C. M. Subwavelength resolution in a two-dimensional photonic-crystal-based superlens. *Phys. Rev. Lett.* **91,** 207401 (2003).

56. Luo, C., Johnson, S. G. & Joannopoulos, J. D. All-angle negative refraction in a three-dimensionally periodic photonic crystal. *Appl. Phys. Lett.* **81,** 2352–2354 (2002).

57. Lu, Z., Shi, S., Schuetz, C., Murakowski, J. & Prather, D. Three-dimensional photonic crystal flat lens by full 3D negative refraction. *Opt. Express* **13,** 5592–9 (2005).

58. Lu, Z. *et al.* Three-dimensional subwavelength imaging by a photonic-crystal flat lens using negative refraction at microwave frequencies. *Phys. Rev. Lett.* **95,** 2–5 (2005).

59. Icenogle, H. W., Platt, B. C. & Wolfe, W. L. Refractive indexes and temperature coefficients of germanium and silicon. *Appl. Opt.* **15,** 2348–2351 (1976).

60. Chernow, V. F., Alaeian, H., Dionne, J. A. & Greer, J. R. Polymer lattices as mechanically tunable 3-dimensional photonic crystals operating in the infrared. *Appl. Phys. Lett.* **107,** (2015).

61. Bauer, J., Schroer, A., Schwaiger, R. & Kraft, O. Approaching theoretical strength in glassy carbon nanolattices. *Nat. Mater.* **15,** 438–443 (2016).

62. Hagemann, H.-J., Gudat, W. & Kunz, C. Optical constants from the far infrared to the x-ray region: Mg, Al, Cu, Ag, Au, Bi, C, and Al2O3. *J. Opt. Soc. Am.* **65,** 742 (1975).

63. Chandler-Horowitz, D. & Amirtharaj, P. M. High-accuracy, midinfrared (450cm−1⩽ω⩽4000cm−1) refractive index values of silicon. *J. Appl. Phys.* **97,** 123526 (2005).

64. Inoue, K. & Ohtaka, K. *Photonic Crystals: Physics, Fabrication and Applications*. (Springer Berlin Heidelberg, 2004).

65. Dresselhaus, M. S., Dresselhaus, G. & Jorio, A. *Group Theory - Application to the Physics of*

Condensed Matter. (Springer Berlin Heidelberg, 2008). doi:10.1007/978-3-540-32899-8

66. Peng, S. 2D and 3D photonic crystals : synthesis , characterization and topological phenomenon. (California Institute of Technology, 2018).

67. Foteinopoulou, S. & Soukoulis, C. M. Negative refraction and left-handed behavior in two-dimensional photonic crystals. *Phys. Rev. B* **67,** 235107 (2003).

68. Foteinopoulou, S. & Soukoulis, C. M. Electromagnetic wave propagation in two-dimensional photonic crystals: A study of anomalous refractive effects. *Phys. Rev. B - Condens. Matter Mater. Phys.* **72,** 1–20 (2005).

69. Luo, C., Johnson, S. G., Joannopoulos, J. D. & Pendry, J. B. Subwavelength imaging in photonic crystals. *Phys. Rev. B* **68,** 45115 (2003).

70. Ash, E. A. & Nicholls, G. Super-resolution aperture scanning microscope. *Nature* **237,** 510–512 (1972).

71. Taubner, T., Korobkin, D., Urzhumov, Y., Shvets, G. & Hillenbrand, R. Near-Field Microscopy Through a SiC Superlens. *Science* **313,** 1595–1595 (2006).

72. Carneiro, V. H., Meireles, J. & Puga, H. Auxetic materials — A review. *Mater. Sci.* **31,** 561–571 (2013).

73. Yang, W., Li, Z. M., Shi, W., Xie, B. H. & Yang, M. B. On auxetic materials. *J. Mater. Sci.* **39,** 3269–3279 (2004).

74. Lu, L., Joannopoulos, J. D. & Soljačić, M. Topological photonics. *Nat. Photonics* **8,** 821–829 (2014).

75. Siroki, G., Huidobro, P. A. & Giannini, V. Topological photonics: From crystals to particles. *Physical Review B* **96,** (2017).

76. Khanikaev, A. B. & Shvets, G. Two-dimensional topological photonics. *Nat. Photonics* **11,** 763–773 (2017).

77. Slobozhanyuk, A. *et al.* Three-dimensional all-dielectric photonic topological insulator. *Nat. Photonics* **11,** 130–136 (2017).

78. König, M. *et al.* Quantum spin hall insulator state in HgTe quantum wells. *Science* **318,** 766–770 (2007).

79. Hsieh, D. *et al.* A topological Dirac insulator in a quantum spin Hall phase. *Nature* **452,** 970–974 (2008).

80. Lu, L., Fu, L., Joannopoulos, J. D. & Soljačić, M. Weyl points and line nodes in gyroid photonic crystals. *Nat. Photonics* **7,** 294–299 (2013).

81. Noh, J. *et al.* Experimental observation of optical Weyl points and Fermi arc-like surface states. *Nat. Phys.* **13,** 611–617 (2017).

82. Potter, A. C., Kimchi, I. & Vishwanath, A. Quantum oscillations from surface Fermi arcs in Weyl and Dirac semimetals. *Nat. Commun.* **5,** 1–6 (2014).

83. Man, W., Megens, M., Steinhardt, P. J. & Chaikin, P. M. Experimental measurement of the photonic properties of icosahedral quasicrystals. *Nature* **436,** 993–996 (2005).

84. Jeon, S., Kwon, H. & Hur, K. Intrinsic photonic wave localization in a three-dimensional icosahedral quasicrystal. *Nat. Phys.* **13,** 363–368 (2017).

85. Ledermann, A. *et al.* Three-dimensional silicon inverse photonic quasicrystals for infrared wavelengths. *Nat. Mater.* **5,** 942–5 (2006).

86. Feng, Z. *et al.* Negative Refraction and Imaging Using 12-fold-Symmetry Quasicrystals. *Phys. Rev. Lett.* **94,** 247402 (2005).

87. Vardeny, Z. V., Nahata, A. & Agrawal, A. Optics of photonic quasicrystals. *Nat. Photonics* **7,** 177–184 (2013).

88. Zoorob, M. E., Charlton, M. D. B., Parker, G. J., Baumberg, J. J. & Netti, M. C. Complete photonic bandgaps in 12-fold symmetric quasicrystals. *Nature* **404,** 740–743 (2000).

89. Kraus, Y. E., Lahini, Y., Ringel, Z., Verbin, M. & Zilberberg, O. Topological states and adiabatic pumping in quasicrystals. *Phys. Rev. Lett.* **109,** 1–5 (2012).

90. Lin, S. Y. *et al.* A three-dimensional photonic crystal operating at infrared wavelengths. *Nature* **394,** 251–253 (1998).

91. Erskine, L. L. *et al.* Two-photon polymerization initiators for three- dimensional optical data storage and microfabrication. *Nature* **398,** 51–54 (1999).

92. Sun, H.-B., Matsuo, S. & Misawa, H. Three-dimensional photonic crystal structures achieved with two-photon-absorption photopolymerization of resin. *Appl. Phys. Lett.* **74,** 786–788 (1999).

93. Tétreault, N. *et al.* New route to three-dimensional photonic bandgap materials: Silicon double inversion of polymer templates. *Adv. Mater.* **18,** 457–460 (2006).

94. Hermatschweiler, M., Ledermann, a., Ozin, G. a., Wegener, M. & von Freymann, G. Fabrication of Silicon Inverse Woodpile Photonic Crystals. *Adv. Funct. Mater.* **17,** 2273–2277 (2007).

95. Rinne, S. a., García-Santamaría, F. & Braun, P. V. Embedded cavities and waveguides in three-dimensional silicon photonic crystals. *Nat. Photonics* **2,** 52–56 (2007).

96. García-Santamaría, F. *et al.* A Germanium inverse woodpile structure with a large photonic band gap. *Adv. Mater.* **19,** 1567–1570 (2007).

97. Liu, J. & Ueda, M. High refractive index polymers: fundamental research and practical applications. *J. Mater. Chem.* **19,** 8907 (2009).

98. Nicole, L., Laberty-Robert, C., Rozes, L. & Sanchez, C. Hybrid materials science: a promised land for the integrative design of multifunctional materials. *Nanoscale* **6,** 6267–92 (2014).

99. Vyatskikh, A. *et al.* Additive manufacturing of 3D nano-architected metals. *Nat. Commun.* **9,** 593 (2018).

100. Fischer, J. *et al.* Exploring the mechanisms in sted-enhanced direct laser writing. *Adv. Opt. Mater.* **3,** 221–232 (2015).